IONIC AND ELECTRONIC TRANSPORT IN CONDUCTING POLYMER SYSTEMS

by

YONGJUN WANG

A DISSERTATION

Presented to the Department of Physics
and the Graduate School of the University of Oregon
in partial fulfillment of the requirements
for the degree of
Doctor of Philosophy

December 2008

University of Oregon Graduate School

Confirmation of Approval and Acceptance of Dissertation prepared by:

Yongjun Wang

Title:

"Ionic and Electronic Transport in Conducting Polymer Systems"

This dissertation has been accepted and approved in partial fulfillment of the requirements for the Doctor of Philosophy degree in the Department of Physics by:

Heiner Linke, Chairperson, Physics
Mark Lonergan, Advisor, Chemistry
Roger Haydock, Member, Physics
Stephen Kevan, Member, Physics
James Hutchison, Outside Member, Chemistry

and Richard Linton, Vice President for Research and Graduate Studies/Dean of the Graduate School for the University of Oregon.

December 13, 2008

Original approval signatures are on file with the Graduate School and the University of Oregon Libraries.

An Abstract of the Dissertation of

Yongjun Wang for the degree of Doctor of Philosophy

in the Department of Physics to be taken December 2008

Title: IONIC AND ELECTRONIC TRANSPORT IN CONDUCTING POLYMER SYSTEMS

Approved: _____
Dr. Mark Lonergan

The electrical properties of conducting polymer-based devices are investigated in order to better understand charge transport through conducting polymers and charge transfer at conducting polymer interfaces with metals and inorganic semiconductors. Experiments on two specific systems are reported: (1) an anionically functionalized conducting polymer between metal electrodes and (2) nanostructured doped conducting polymer-semiconductor interfaces.

Temperature dependent impedance measurements are reported on an anionically functionalized polyacetylene sandwiched between two gold electrodes ($Au|P_A|Au$). These measurements provide key quantities regarding the ionic carriers in this system, such as the characteristic frequency for electrode polarization, ionic DC conductivity, activation energy, effective ion concentration, and hopping frequency. Impedance measurements are also reported on samples where excess electronic carriers had been introduced with a DC bias and at temperatures sufficiently low so as to freeze out the

ionic carriers. In addition to providing information about the dielectric relaxation of electronic carriers such as the characteristic frequency for electrode polarization and activation energy, these low-temperature impedance measurements also support the ionic dielectric relaxation assignments.

Temperature-dependent potential step experiments, in combination with the dielectric measurements probing ionic carriers, demonstrate the direct connection between the redistribution of ions and an enhancement in carrier injection in the Au|P_A|Au system. Further potential step experiments followed by relaxation through either a short- or open-circuit configuration demonstrate that the electric field distribution is closely related to the amount of injected electronic carriers. The electric field distribution changes from being mostly determined by ionic carriers to being jointly determined by both ionic and injected electronic carriers when the density of injected electronic carriers is higher than that of the effective ionic carriers.

To investigate charge depletion and transport at length scales less than the depletion width of a semiconductor interface, nanoscale metal-InP contacts with low barrier height were embedded within conducting polymer-InP contacts with high barrier height. Electrical measurements on these hybrid interfaces indicate that charge transport across the nanoscale metal contacts is affected by the neighboring high barrier region when the size of the metal contacts is less than the depletion width of the conducting polymer-InP background.

CURRICULUM VITAE

NAME OF AUTHOR: Yongjun Wang

PLACE OF BIRTH: KuiTun, China

DATE OF BIRTH: February 1975

GRADUATE AND UNDERGRADUATE SCHOOLS ATTENDED:

University of Oregon
Shandong University
Xinjiang University

DEGREES AWARDED:

Doctor of Philosophy in Physics, 2008, University of Oregon
Master of Science in Physics, 2002, University of Oregon
Master of Science in Physics, 2000, Shandong University
Bachelor of Science in Physics, Xinjiang University

AREAS OF SPECIAL INTEREST:

Organic semiconductors, solid state electrochemistry, semiconductor device physics, impedance spectroscopy.

PROFESSIONAL EXPERIENCE:

Research Assistant, University of Oregon, 2002-2008
Research Intern, Invitrogen Inc. 06.2008-09.2008
Teaching Assistant, University of Oregon, 2000-2002

PUBLICATIONS:

F. D. Lin, Y. J. Wang, and M. C. Lonergan, J. Appl. Phys. (in press).

J. F. Wang, Y. J. Wang, Mater. Sci. Eng. B **96**, 8 (2002).

Y. J. Wang, J. F. Wang, J. Mater. Sci. Lett. **20**, 19 (2001).

Y. J. Wang, J. F. Wang, J. Phys. D: Appl. Phys. **33**, 96 (2000).

Y. J. Wang, J. F. Wang, Eur. Phys. J. AP. **11**, 155 (2000).

ACKNOWLEDGMENTS

First, I would like to thank Dr. Mark Lonergan for his continuous support and direction during the entire period of this dissertation project. For those years Mark made many efforts to build my critical thinking and problem solving abilities. I also benefited greatly from his advices on effective communication, scientific presentation and writings. His influence on me is not limited to scientific research. He is open-minded in both scientific research and daily life.

Several people in the Lonergan Lab also played important role during my pursuit of scientific development. Dr. Frank E.Jones taught me many skills in semiconductor device fabrication. He also modified the SEM into an Electron beam writing system and developed the procedures to fabricate nano-scale metal patterns on the surface of inorganic semiconductors. Because of these work, I was able to carry out studies on charge transfer across the nano-structured hybrid semiconductor interfaces. I collaborated with Fuding Lin on the impedance measurements. We had many inspirational discussions about wide range of subjects from detailed experimental techniques to data analysis and fundamental physics. I had a great time working with him. Dr. Carrie Daniels-Hafer contributed to various parts of my work. She showed me the techniques needed to make "ideal" Schottky diode with polyrrole and InP during my early time in Lonergan Lab. Also, she shared with me much of her understandings of semiconductor physics while I was struggling with all the jargons and concepts in the literatures. In addition, she investigated great efforts in carefully reading the drafts of my dissertation, and she

offered many helpful suggestions and feedbacks. Particular thanks must be given to T.J.Mills, who collaborated with me in interpreting electrical measurements presented in chapter VI. I am always amazed by his ability to reach over physics with chemistry training and obtain insights on both sides. It is convenient that we sat on neighboring desks, which facilitate frequent discussion. Even though he mostly focused on simulations and while I on experiments, we managed to find some common ground that brought senses to both the computational and experimental results. I had many scientific interactions with Dr. Calvin H.W. Chang. Beyond that, our joyful activities included weight training three days a week for a few months and 9-hole golf game. Ian Moody has always been nice to me even though I spell his name as "Ion" in an email to our group. He also listened to me during my hard times. I appreciate him very much for listening. Ian also spent much time explaining the fundamental properties of nanocrystals, as well as reading some drafts of my dissertation. David Stay is an excellent chemist and public educator. He can always find a way to explain chemistry in a clear and enjoyable way. His explanations are interesting enough to make me feel that I missed a lot of fun because I didn't get trained in chemistry. David (together with his wife Marcelle) also helped me in developing writing skills and introduced to me many useful resources such as the Thesaurus. I would also like to thank Ethan Walker, Stephen Robinson and Dean Johnston for many discussions and help in proofreading my dissertation.

I would also like to thank Chris, David and John in the student shop. I admire the machinist perspective they demonstrated while helping me, but I don't think I would ever be able to adapt it.

Dedicated to my wife Jingyun, our parents, and our daughters Mica and Maya.

TABLE OF CONTENTS

Chapter Page

I. INTRODUCTION 1
1.1 Overview 1
1.2 Historical Background 2
1.3 Charge Conduction Semiconductor Devices 4
1.4 Charge Injection at Metal-semiconductor Interfaces (M-SC) 5
1.5 Charge Transport in Inorganic MIEC 8
1.6 Conducting Polymers 10
1.7 Polymer Light-emitting diode 14
1.8 Polymeric MIEC 16
1.9 Strategy of Dissertation 20

II. PRINCIPLES AND INSTRUMENTATION OF IMPEDANCE SPECTROSCOPY 23
2.1 Overview 23
2.2 Dielectric Relaxation and Polarization 24
2.2.1 Mechanism of Polarization 28
2.2.2 Impedance-related Functions 29
2.3 Impedance Spectroscopy 31
2.3.1 Data Presentation 33
2.3.2 Measurement Techniques 34
2.4 Application of Impedance Spectroscopy 35
2.4.1 Impedance Spectroscopy of Ionic Conductors 35
2.4.2 Space Charge Polarization and Diffusion Capacitance 38
2.4.3 Semiconductor Interfaces 40

III. IMPEDANCE ANALYSIS OF AN ANIONICALLY FUNCTIONALIZED POLYACETYLENE BETWEEN METAL ELECTRODES 42
3.1 Overview 42
3.2 Sample Preparation and Measuring Techniques 43
3.2.1 Sample Preparation 43

Chapter Page

3.2.2 Measurement Techniques 44
3.3 Experimental Results 45
3.3.1 Impedance-related Functions and Dielectric Relaxation Processes 45
3.3.2 Characteristic Frequencies 48
3.4 Discussion 53
3.4.1 Assignment of Dielectric Relaxation Processes 53
3.4.2 Scaling Properties 58
3.4.3.Electrode Polarization Model 59
3.4.4 Jump Relaxation Model 61
3.5 Conclusions 66

IV. IMPEDANCE ANALYSIS OF ELECTRONIC CARRIERS IN AN ANIONICALLY FUNCTIONALIZED POLYACETYLENE BETWEEN METAL ELECTRODES 67
4.1 Overview 67
4.2 Experimental Procedures 68
4.3 Experimental Results 69
4.3.1 Small Amplitude AC Impedance 69
4.3.2 Influence of V_{DC} 77
4.4 Discussion 81
4.4.1. Impedance-related Functions 81
4.4.2 Characteristic Frequency of the Electrode Polarization 82
4.4.3 Effects of V_{DC} 83
4.5 Conclusion 86

V. IMPEDANCE ANALYSIS OF AN ANIONICALLY FUNCTIONALIZED POLYACETYLENE UNDER DC VOLTAGE BETWEEN METAL ELECTRODES 88
5.1 Overview 88
5.2 Experimental Procedures 89
5.3 Experimental Results 90

Chapter Page

5.4 Discussion 98
5.4.1 Influence of Ion Motion on Impedance Measurement 98
5.4.2 High DC Voltage 101
5.4.3 Normalization at Various Temperatures 101
5.4.4 Capacitance Calculations[13] 105
5.5 Conclusions 109

VI. ELECTRICAL CHARACTERIZATION OF AN ANIONICALLY FUNCTIONALIZED POLYACETYLENE BETWEEN METAL ELECTRODES 111
6.1 Overview 111
6.2 Experimental Procedures 111
6.3 Experimental Results 115
6.4 Discussion 130
6.4.1 Low Voltage Regime (Vapp up to 0.7V) 135
6.4.2 High Voltage Regime (Vapp>0.7V) 136
6.4.3 Discharging Behavior in the Short-Circuit Configuration 138
6.5 Conclusion 143

VII. LATERAL BARRIER HEIGHT INHOMOGENEITIES AT INP-POLY(PYRROLE) INTERFACES 145
7.1 Overview 145
7.2 Theoretical Treatment of Barrier Formation and Charge Transport at M - SC Contacts 147
7.3 Previous Work on n-InP - PMH Interfaces 152
7.4 Parallel conduction vs. "Pinched Off" Barrier Inhomogeneities 154
7.5 Experimental Procedures 157
7.6 Experimental Results & Discussion 160
7.7 Conclusions 174
7.8 Future work 175

Chapter Page

VIII. CONCLUSIONS AND FUTURE DIRECTIONS 176

BIBLIOGRAPHY 181

LIST OF FIGURES

Figure		Page
1.1	Device architecture of anionically functionalized polyacetylene sandwiched between two Au electrodes	4
1.2	Common conducting polymers	11
1.3	Doping of polyacetylene	12
1.4	Two examples of internally compensated conducting polymers and the self-doping	14
1.5	Illustrations of major difference between the electrochemical model and the electrodynamic model	18
2.1	Relaxation of a dielectric material	25
2.2	Plots of both the real and imaginary portions of the frequency dependent complex permittivity as function of the characteristic frequency	27
2.3	Typical polarization mechanisms as a function of time in seconds	30
2.4	The schematic of transfer function analyzer	35
3.1	Sample structure diagram	44
3.2	Frequency dependent ε' at temperatures from 308K to 398K	46
3.3	Thickness dependence of capacitance spectra	47
3.4	Frequency dependent σ from T=308K to 398K	48
3.5	Frequency dependent ε'' at temperatures from 308K to 398K	49
3.6	Loss tangent spectra at temperatures from 308K to 398K	50
3.7	Temperature dependence of ω_{EL} and ω_{LT}	51
3.8	The temperature dependence of ω_{LT} for 5 samples	52
3.9	The thickness dependence of ω_{LT}	53
3.10	The equivalent circuit of the system	55
3.11	Frequency dependent σ at 398K for samples with various thicknesses	56
3.12	Thickness dependence of the ω_{LT}	57
3.13	Frequency dependent σ at temperatures from 308K to 398K normalized by the ionic DC conductivity	59
3.14	The schematic representation of single particle sitting in a potential well	62
3.15	The schematic representation of the jump-relaxation process	63
3.16	Frequency dependent ε' of a 1600nm thick sample at temperatures from 308K to 398 K	64
3.17	The temperature dependence of the hopping frequencies	65
4.1	Frequency dependent ε' in the temperature range from 173K to 233K	70

Figure		Page
4.2	Frequency dependent ε'' in the temperature range from 173K to 233K	71
4.3	Frequency dependent σ in the temperature range from 153K to 233K	72
4.4.	The frequency dependence of the loss tangent in the temperature range from 173K to 233K	73
4.5	Frequencies related to the electrode polarization ω_{EL} and ω_{LT}	74
4.6	The DC voltage (V_{app}) dependence of the loss tangent at 173K as a function of frequency	75
4.7	Frequency dependent capacitance as a function of DC voltage (V_{app}) at 173K	76
4.8	Frequency dependent σ at 173K	76
4.9	Frequency dependent σ under V_{DC} from 0V to 1.4V at 203K	77
4.10	Derivatives of ε' spectra at 203K	78
4.11	The frequency dependence of the capacitance under V_{DC} from 0V to 1.4V at 203K	79
4.12	Frequency dependent capacitance as a function of the reverse DC voltage (V_{DC}) at 203K	80
4.13	Capacitance as a function of V_{DC}	80
4.14	Frequency as a function of V_{DC}	85
5.1	Frequency dependent capacitance under various V_{DC}	91
5.2	Frequency dependent ε' at T = 308K, 328K, and 348K	92
5.3	Frequency dependent ε' at T = 308K, 328K, 348K	93
5.4	Frequency dependent ε' at T = 308K with applied V_{DC} from 0V to 0.9V	94
5.5	Frequency dependent σ at T = 308K with V_{DC} from 0V to 1.1V	95
5.6	Frequency and V_{DC} dependence of the capacitance in the low frequency region at T = 308K	96
5.7	Applied voltage dependence of the capacitance	97
5.8	Frequency dependent σ for T = 308K under the V_{DC} range from 0V to 0.5V	97
5.9	Frequency dependent σ at T =308K	98
5.10	Transient current measurements at T = 308K and T = 328K	104
5.11	Current and Cosine function with a period of 1second as a function of time	107
5.12	Capacitance measured with impedance spectroscopy and that calculated from the Fourier transform of transient current as a function of frequency	108

Figure Page

5.13 Frequency dependence of the capacitance with V_{DC}=0.5V and that from the Fourier transform of the transient current at V_{DC}=0.5V 108
6.1 Transient curr ent in response to potential steps V_{app} = 0.1V, 0.5V, 0.8V and 1.2V (as labeled) at 328K 113
6.2 Steady-state current from potential step measurements plotted as a function of V_{app} 114
6.3 Transient cu rrent in response to potential steps in the range V_{app} = 0.1V to 0.7V 116
6.4 Transient cur rent in response to potential steps in the range V_{app} = 0.8V to 1.5V (as labeled) and plotted on a log-log scale 116
6.5 Stead y-state current versus V_{app} 117
6.6 Transient current in response to a potential step with V_{app}=0.6V at T = 298K, 315K, and 328K (as labeled) for sample yjw8080A 118
6.7 Arrhenius plot of t_{onset} 119
6.8 S hort-circuit relaxation current after V_{app} from 0.1V to 1.5V has been applied for 4 hours 120
6.9 Relationship of the total charge extracted from integration of the short-circuit relaxations as a function of V_{app} 121
6.10 Open-circuit voltage (Y axis) after the sample has been prepared to steady state 122
6.11 Initial open-circuit voltage V_{OC} vs V_{app} 123
6.12 Linear current-voltage sweep measurements and open-circuit voltage 124
6.13 Short -circuit relaxation current following a potential step of V_{app} =1.5V as a function of the duration of the potential step (as labeled) 126
6.14 Current on the left axis and initial short circuit current on the right axis as a function of time 126
6.15 Current on the left axis and charge on the right axis as a function of time .. 127
6.16 Thickness dependence of the steady-state current with samples of thickness 200nm, 220nm, 667nm and 1800nm 128
6.17 C omparisons of transient short-circuit current at 1.5V with thicknesses ranging from 200nm to 1800nm 125
6.18 Charg e versus V_{app} with samples of various thicknesses 129
6.19 Ener gy level diagram of the Au|Polymer|Au device 130
6.20 Ener gy level diagram of the Au|Polymer|Au device with V_{app} 131
6.21 P lot of the transient current separated into four regions to indicate the evolvement of both the electric field and transport properties 132

Figure		Page
6.22	The charge (top), field distribution (middle), and short-circuit current with (a) low V_{app} 0<V<0.7V, (b) intermediate V_{app} between 0.7V to 1V, and (c) high V_{app} between 1V to 1.5V	136
7.1	Characteristic dependence of current (J) on applied bias (V_{app})	147
7.2	Formation of a barrier between an n-type inorganic semiconductor and a conductor	148
7.3	Variation of charge density, electric field and barrier height with distance x into an n-type semiconductor from the interface	149
7.4	Competing charge transport mechanisms at an inorganic semiconductor | conductor interface	150
7.5	Current density – applied voltage (J-V_{app}) curves for an n-InP | PMH interface	153
7.6	Temperature dependence of the current density (J) for an n-InP|PMH interface	154
7.7	Diagrams for parallel conduction and Pinch-off	155
7.8	The schematic of the modified SEM system	158
7.9	The schematic of the parallel n-InP --PMH|metal device architecture	159
7.10	Comparison of the barrier height of n-InP|PMH and n-InP | Cr interfaces	161
7.11	The effect of plasma cleaning on the barrier height of PMH-InP interfaces	162
7.12	Patterns of various shapes and sizes fabricated onto n-InP substrates,	163
7.13	Size effects of patterned samples of various line width	164
7.14	Interfaces exhibiting "pinch-off" effects at room temperature	165
7.15	Current density-applied voltage characteristics of a representative hybrid InP-Cr|PMH interface	167
7.16	Quality factors extracted from both (a) low bias and (b) high bias regions of the J-V_{app} data	168
7.17	Barrier height as a function of pattern size as a function of distance into the inorganic semiconductor	170
7.18	The effect of applied voltage on the barrier height of the interface, for V_{app} at -0.5, 0, and +0.5 V	171
7.19	Comparisons of current-voltage relationship in hybrid interfaces with that of simulated results	173

LIST OF TABLES

Table Page

3.1 Results from modeling with the electrode polarization 60

CHAPTER I

INTRODUCTION

1.1 Overview

Mixed ionic-electronic conductors (MIECs) are fundamentally intriguing because the interactions between ionic and electronic charge carriers offer both rich physics and often unique device potential. The many charged species participating in conduction gives rise to complexity on the one hand, and the potential for better manipulation of the electrical properties and broader applications than traditional single-carrier-type devices on the other. For example, electronic charge transport in MIECs can in principle be tuned by manipulating ionic charges, as long as the influence of the ionic carriers on electronic carrier injection can be fully understood. Considering that MIECs are very complex and that so far most of the work on MIECs has focused only on either electronic or ionic transport, it is not surprising that the operational mechanism of electronic devices containing MIECs is still largely controversial. The goals for this work are to investigate systemically ionic and electronic transport and their influence on one and other in a model MIEC. Through investigating the fundamental properties of MIECs, a foundation can be laid for understanding the interactions of ionic and electronic carriers, which in turn offers the promise of controlling charge injection by ionic functionality.

The remainder of this chapter begins with a walkthrough of the studies that have been done on MIECs. An overview of physics of charge transport in semiconductor devices follows in order to build a theoretical framework. Finally, the strategy employed to achieve the goals outlined above is presented.

1.2 Historical background

Studies on MIECs initially focused on inorganic materials such as ionic crystals[1,2,3,4], ceramics[5,6,7,8] and glasses[9,10]. Such studies were driven by applications for catalytic electrodes in solid-state ionic devices[11], solid oxide fuel cells[12,13], batteries[14,15], and chemical sensors[16], to name a few. Although the broad range of materials studied to date differ greatly in terms of physical structure, they share in common the ability to transport both electronic and ionic carriers in the solid state. The device applications of MIECs often utilize the migration (as in solid electrolyte in batteries) or redistribution (as in polymer light-emitting electrochemical cells) of these ionic carriers. Pioneering work concerning the fundamental relationship between the current and the voltage was derived by Wanger[17,18] as early as 1933. In the early 1970s, Choudhury and Patterson[19,20,21] extended Wanger's theory to include both the charge and the field distribution in the materials. In these inorganic materials, it is generally believed that it is the defects in the material that play a central role in ionic conduction[22]. Ions move from one site to another in the form of diffusion (under no electrical field) or drift (under the influence of an electrical field) and contribute to the current. Even though these works offered some insight into the interplay of electronic and ionic carriers, their main focus was ionic conductivity.

In the last 10 years, polymeric MIECs[23,24,25] have received much attention due to promising applications in various semiconductor devices. Among them, a new type of organic light emitting device, namely the polymer light-emitting electrochemical cell (PLEC). The PLEC provides attractive properties such as high efficiency, low threshold

voltage and insensitivity to contact electrodes when compared with the polymer lighting emitting diode (PLED).[26,27,28].

While previous work has provided important insight into the understanding of some MIECs,(reference?) basic questions, such as the role of ionic carriers in electronic carrier transport, remain unanswered. This lack of understanding stems from the complexity of MIECs on one hand, and the shortage of systematic electrical characterization on the other. The goal for this dissertation is to systematically investigate the electrical properties of a polacetylene-based MIEC using various techniques such as impedance spectroscopy, potential step experiments, electrical relaxation in short- or open-circuit configuration, and fast current-voltage scans. The platform selected for these studies is a polymer electrochemical system consisting of an ionically functionalized conducting polymer sandwiched between two gold electrodes (see Figure ??). The reasons behind this selection are manifold. First, conducting polymers uniquely combine chemical, electrical and mechanical properties. This offers convenience in manipulating electrical properties by chemical doping. Second, the availability of conducting polymers predicts widespread application in various electronic devices, as was mentioned earlier. The specific polymer to be studied is a polyacetylene with ionic functionality. In addition to being an ideal platform to investigate the operational mechanism of MIECs, ionically functionalized polyacetylenes have been used to develop an approach to stable interfaces between dissimilarly doped regions. Such interfaces provide a means of realizing regions of charge depletion analogous to that at traditional inorganic semiconductor interfaces [29,30,31]. Another favorable property of ionically functionalized

polyacetylenes is that they are a single component system, in contrast to the polymer blends often used in studies of MIECs and where phase separation is a potential problem.

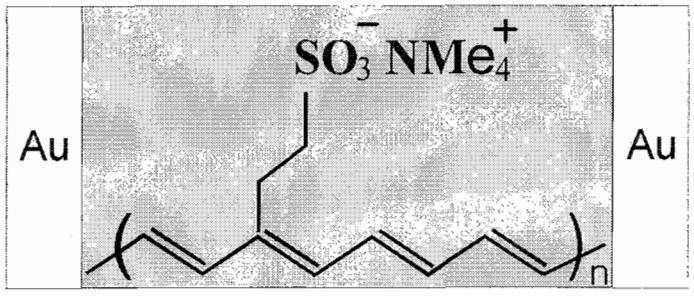

Figure 1.1 Device architecture of anionically functionalized polyacetylene sandwiched between two Au electrodes

To understand the electrical characteristics of MIECs consisting of an ionically functionalized polyacetylene sandwiched between two metal electrodes, it is necessary to introduce charge transport processes in semiconductors. For the thin-film semiconductor device to be studied herein (see Figure 1.1) , charge transport can be roughly divided into two processes in series: charge transport across the metal-semiconductor interfaces (injection) and charge transport within the semiconductor. Both of these processes are discussed in detail below.

1.3 Charge conduction in semiconductor devices

The motion of charge carriers in semiconductors is driven either by electric field (drift) or a carrier concentration gradient (diffusion).

Under the influence of an electric field, the current density at a steady state is:

$$J = qn\mu E \qquad \text{(eq. 1.1)}$$

where J_n is the current density, q is the unit of charge, n is the carrier concentration, μ is the mobility of carriers, and E is the electric field.

The diffusion of charge carriers due to spatial variation of the carrier concentration can be described as follows:

$$J = qD \frac{dn}{dx} \qquad \text{(eq. 1.2)}$$

where J is the diffusion current density, q is the elemental charge, D is the diffusion constant, and n is the carrier concentration.

It is worthwhile to point out that even though governed by the same rules as shown in eq. 1.1 and eq. 1.2, the nature of charge motion in crystalline and disordered semiconductors is very different. In disordered semiconductors, charge carriers are mostly localized and move from one site to another by hopping.

1.4 Charge injection at metal-semiconductor interfaces (M-SC)

When describing charge injection at M-SC interfaces, the normal starting point is to define the energy difference between the respective Fermi energies of the isolated materials. The Schottky barrier height (ϕ_b) is a measure of the mismatch of the energy levels for majority carriers across the M - S interface. The first order theory of a Schottky barrier is the Schottky-Mott theory, which can be described as follows[32,33]:

$$\Phi_b = \Phi_M - \chi_s \qquad \text{(eq. 1.3)}$$

Where Φ_b is the Schottky barrier height, Φ_M is the work function of the metal, and χ_s is the electron affinity of the semiconductor.

Due to the difference in their Fermi levels, charge redistribution occurs when two bulk materials come into contact, bringing them into equilibrium. In the case of an n-type semiconductor coming into contact with a metal surface, electrons move from the semiconductor to the metal until the Fermi levels are equal. The fixed uncompensated ions in the semiconductor then form a space charge region ρ , which leads to both an electric field ε and a built-in potential ψ. A detailed description of barrier formation can be found in Chapter VII section 7.2, where diagrams are provided.

If it is assumed that a Schottky barrier is established in a metal - conducting polymer interface (M - CP) as described above, charge transport across the interface can happen in several ways[34]. The major mechanisms are summarized below:

(1) Thermionic emission of electronic carriers over the top of the potential barrier, ϕ_b

(2) quantum-mechanical tunneling through ϕ_b

(3) recombination in the interfacial region

Only the first two mechanisms will be addressed in detail here because the recombination process is only important in limited cases at low temperature and low forward-bias voltages.

A general way to describe the current density (J)-voltage (V) behavior across an interface is the free-electron model.

$$J = e\int V_x K(p)N(p)f[E(p)]dp \qquad \text{(eq. 1.4)}$$

Where $\kappa(p)$ is the probability that an electron with a particular energy will cross the interface, $N(p)$ is the carrier density at a certain energy, and $f(E(p))$ is the fraction of occupied states described by the Fermi-Dirac distribution.

$$f(E-u) = \frac{1}{Exp(\frac{E-u}{kT})+1} \qquad \text{(eq. 1.5)}$$

where μ is chemical potential.

In Bethe's original thermionic emission mechanism, it is assumed assumes that all of the electrons with sufficient energy to exceed the interfacial potential barrier ϕ_b will contribute to the current. In addition, Bethe assumed that the electrons move ballistically and that the metal acts as almost a perfect sink for charges leaving a semiconductor and entering the metal[34]. The effects of scattering and diffusion were later considered by Schottky and generalized by Crowell and Sze[35,36]. By choosing the integration interval to be from ϕ_b to infinity, the *J-V* relationship based on the thermonic emission theory is:

$$\begin{aligned} J &= J_0 \exp(qVn/kT)\{1-\exp(-qV/KT)\} \\ J_0 &= A^* T^2 \exp[-q\phi_b/kT] \\ A^* &= m^* qk^2/8\pi^2\hbar^3 \\ n &= [1-(\partial\phi_b/\partial V)]^{-1} \end{aligned} \qquad \text{(eq. 1.6)}$$

where J is the current density, J_0 is the exchange current density, q is the elemental charge, V is the applied voltage, n is the empirical quality factor incorporated to accommodate deviations from Thermonic emission in practise , K is the Boltzman

constant, T is the temperature, A^* is the Richardson constant, m^* is the effective mass, m is the mass of electron, $\hbar$ is the Planck constant and ϕ_b is the barrier height.

Under certain circumstances (for example with degenerate semiconductors or in the presence of a high electric field at the interface), it is more likely for electrons with energies below the top of barrier to penetrate the barrier by quantum-mechanical tunneling. The tunneling probability can be estimated with the Wentzel-Kramers-Brillouin (WKB) approximation[34]. Fowler and Nordheim considered the triangular barrier profile, and in this case, the tunneling current is[37] :

$$J = \sigma_0 F^2 \exp[-\frac{4\sqrt{2m^*}(q\phi_b)^{3/2}}{3q\hbar E}] \qquad \text{(eq. 1.7)}$$

$$\sigma_0 = \frac{q^3}{16\pi^2\hbar(q\phi_b)} \qquad \text{(eq. 1.8)}$$

where J is the current density, ϕ_b is the barrier height and depends on applied voltage, q is the unit of charge, h is the Planck constant and E is the electric field.

A basic step from the free electron model to materials with a crystal structure is to replace the mass of the electron with an effective mass, a term that accommodates the overall influence of the crystal structure on the motion of electrons.

1.5 Charge Transport in inorganic MIEC

The discussion above focused on a system with only electronic carriers. Driven by fundamentals and promising applications, attention has also been paid to mixed ionic-electronic conductors (MIECs) in which both ionic and electronic carriers contribute to

electric conduction. Early work on MIECs focused on inorganic materials. Theoretical treatment of charge transport in mixed ionic-electronic systems was reported by Wanger,[17,18], Choudhury and Patterson[19,20,21], Reiss[38,39], and Nafe[40]. Most experimental studies on inorganic mixed conductors focused on ionic conductivity due to the fact that most applications utilize ionic conduction almost exclusively [41,42,43,44]. The applications of specific materials are closely-related to the type of ions they conduct. For example, oxygen ion conductors are primarily used in chemical sensors and solid oxygen fuel cells[45,46]; lithium ion conductors are mostly used in batteries[47,48]; while proton conductors are widely used in fuel cells[49,50].

A primary quantity of interest for mixed conductors is ionic conductivity, due to the fact that it is most-closely related to device applications. It is generally believed that ionic conductivity results from either intrinsic or extrinsic defects formed in various ways. The classic microscopic models were developed by Frenkel and Schottky and described ions moving among vacant or interstitial lattice sites leading to long-range ionic charge conduction in a rigid structure[51,52]. At equilibrium, ions occupy the energy minimum that is defined by the physical properties of the material. Under the influence of thermal energy, there is a certain probability for ions to move from one minimum energy site to another, which is often called hopping. The probability is determined by the energy barrier, the distance between the two sites, and the temperature. In the vacancy mechanism, the vacancy hops from one lattice site to another accompanied by ion hopping in the opposite direction. In the interstitial model, ions move through the interstitial sites. The interstitial model describes the situation when an ion moves from a

lattice site to an interstitial site, with an interstitial ion filling the remaining vacancy. Despite the mechanistic differences in the above models, ion conductivity can generally be described by an Arrhenius-type equation[53]:

$$\sigma = \frac{\sigma_0}{T}\exp(-E_A / kT) \qquad \text{(eq. 1.9)}$$

where σ is the ionic conductivity, T is the temperature, E_A is the activation energy for defect motion and migration, and k is the Boltzmann constant.

Overall, the ionic conductivity of inorganic materials varies from as little as 10^{-11} to 10 Siemens/cm for fast ion conductors.

The materials under investigation herein belong to the class of organic semiconductors. Before we move on to describing polymeric MIECs, some attention needs to be paid first to conducting polymers. Features of conducting polymers, such as their structure, chemical doping and ionic functionality, are important in order to understand the electrical characteristics of polymeric MIECs.

1.6 Conducting polymers

The key component in a polymeric MIEC is the conducting polymer. Figure.1.2 listed some common conducting polymers.

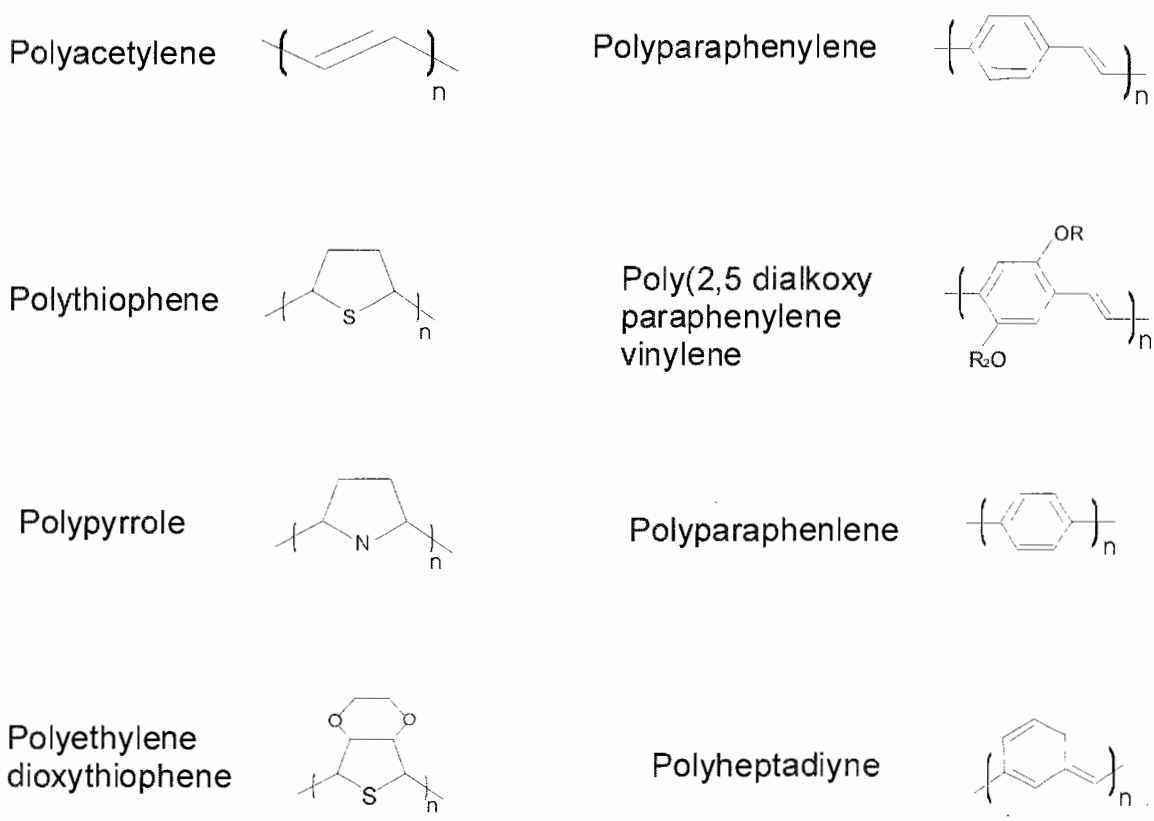

Figure 1.2 Common conducting polymers

The electronic conductivity of a conducting polymer can vary from that of an insulator to a metal through the process of doping, either chemically or electrochemically. In electrochemical doping, electrodes supply the redox charge to the conducting polymer, while ions diffuse in or out of the polymer structure from a nearby electrolyte to compensate the electronic charge. Compared to chemical doping, the electrochemical doping process offers better control because the doping level is precisely defined by the voltage between the conducting polymer and counter electrode.

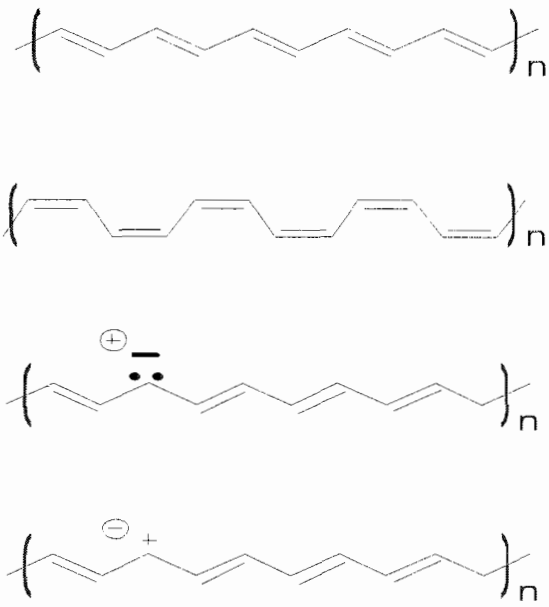

Figure 1.3 Doping of polyacetylene (a) Trans-Polyacetylene (b) Cis-Polyacetylene (c) n-doping (d) p-doping of polyacetylene In (c), the electron (black dot) introduced chemically or electrochemically is compensated by cation , which constitutes n-doping. While in (d), excess hole is compensated by anion for charge neutrality. It is therefore p-doping. In both cases the ions are mobile and can move under the influence of an electric field or an concentration gradient.

Polyacetylene was the first conducting polymer to successfully doped and has been studied extensively ever since. It is used here to show the doping process. Polyacetylene has two isomers: trans form and cis form, as showed in figure 1.3. Also, polyacetylene can be either n-doped or p-doped, as we can see in part (c) and (d) in figure 1.3 respectively.

A major difference between the doping of inorganic semiconductors and conducting polymers is that in the former the dopant atoms are immobilized by the crystal structure. In contrast, the dopant atoms can move throughout the material in an energy-activated processes in conducting polymers. This causes a potential problem in the fabrication of

homojunctions between dissimilarly doped polymeric materials. The mobility of dopant atoms in conducting polymers makes it impossible to form a stable space charge region. One way to solve this problem and to obtain the analogous charge depletion that exists in inorganic semiconductor devices is to have ions covalently bound to the polymer backbone. This way a self–doping process can occur, with ionic functional groups acting as counter ions for electronic carriers, as shown in figure.1.4. Conducting polymers which utilize this self-doping process do not contain any mobile counter-ions. Self-doping is a unique property of ionically functionally polymers and is very critical in achieving stable organic semiconductor homojunctions. Reference?

The doping of ionically functionalized conducting polymers can also happen during electrical characterization. The structure used to measure the ionic and electronic properties of most polymeric devices consists of sandwiching one or more layers of the active polymer material between two electrodes. As was discussed previously, the electronic charge can be injected from the electrode into the conducting polymer. In the case of ionically functionalized polymers in a two electode geometry, this charge injection can result in a self-doping process analogous to that described previously , with the mobile counter ions redistributed within the polymer to compensate the injected electronic carriers. The mobile ions in the polymer make the doping possible without the need for a separate electrolyte. This scenario will be discussed in detail in chapter VI, which focuses on electrical measurements of an ionically functionalized polyacetylene sandwiched between two electrodes.

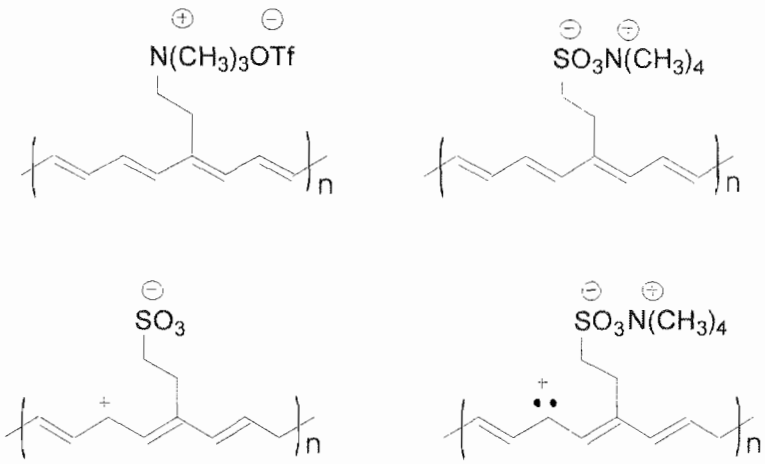

Figure.1.4 Two examples of internally compensated conducting polymers and the self-doping. Top two graphs show the units of anionically functionalized (P_A,left) and cationically functionalized (P_C,right) polyacetylene respectively. The bottom two graphs illustrated the n-doping (left) and p-doping (right) of the cationically functionalized polyacetylene respectively. The n-doping of Pc is self-doping because excess electron(•) is compensated by the cation on the backbone and there is no need to introduce cation externally. The mobile counter ion is not present in the polymer if the doping density matches the ion concentration. In contrast, in the p-doping of the P_C, (bottom right graph), the incorporation of anion from external source is necessary to compensate the hole (+).At the same time, the p-doing in P_A is self-doping.

1.7 Polymer light-emitting diodes

One example of a conducting polymer device that has been studied extensively is the polymer light-emitting diode (PLED). Electrical conduction in PLEDs is mostly electronic. As a result, the PLED is a good reference point to understand the role of ionic carriers by comparing the electrical properties of PLECs with those of PLEDs.

As in inorganic semiconductor devices, electronic carriers transport across the electrode-semiconductor interface in PLEDs through thermionic emission or tunneling. Electronic charge migration or diffusion across the bulk constitutes another process in

series with charge injection. The overall conductivity in a PLED is jointly determined by both processes, with the much slower one dominating the performance [56,57]. In the case of a PLED with high barriers, slow charge injection generates high resistance at the interfaces. Therefore, interfacial processes represent the conductivity of the PLED. However in case of diodes with good operational characteristic, such as a low turn-on threshold and high efficiency, the charge conduction across the bulk is the limiting factor for current flow because of a space charge region built up in the polymer. The charge transport can be described with the space-charge-limited current (SCLC) model.

The SCLC model was developed by A.Rose and Lampert to explain the current in insulating materials[58]. The perfect trap-free insulator and the injection of only one type of electronic carrier is a simplified case, but it still lends a great deal of insight into the underlying physics of charge injection into near intrinsic semiconductors.

The simplified theory starts with a set of equations as follows:

$$J = e\mu n\mathrm{E} \qquad \text{(eq. 1.10)}$$

$$\frac{\varepsilon}{e}\frac{d\mathrm{E}}{dx} = n(x) - n_0 \qquad \text{(eq. 1.11)}$$

$$n(x) = N_C \exp\frac{V(x) - E_c(x)}{kT} \qquad \text{(eq. 1.12)}$$

Where J is the drift current, e is the unit of charge, μ is the mobility, E is the electric field, ε is the dielectric constant, $n(x)$ is the carrier concentration, N_C is the effective density of states in the conduction band, $V(x)$ is the electrostatic potential, E_C is the energy at the edge of conduction band, k is the Boltzman constant, and T is the temperature.

In the above equations, the contribution of diffusion to the steady-state current is ignored. In addition, it is assumed that the electrode kinetics is fast enough so that the electrode is effectively infinite reservoir of carriers. The boundary condition is then: $E(x=0)=0$

An analytical solution with these assumptions and boundary condition is:

$$J = (\frac{9}{8})\varepsilon\mu(\frac{V^2}{L^3}) \qquad \text{(eq. 1.13)}$$

where V is the applied voltage and L is the thickness of the sample.

Therefore, the SCLC predicts square-law current-voltage characteristic.

1.8 Polymeric MIEC

Ionic conductivity in a polymer MIECs is an energy activated process, and so experimental data can be fitted with either the Arrhenius form, or the Vogel-Thanmann-Furcher(VTF) form[59,60]. The mechanism of ion conduction in polymer MIECs in which the conductivity follows the VTF form is related to the polymer chain viscosity which decreases rapidly above the glass transition temperature. The ion is transported by the motion of polymer segments according to the free volume model [61,62]. When temperature increases, the polymer expands and creates a local empty space, or "free volume" into which polymer segments can move. This then increases the mobility of both the polymer segment and the ions. Overall, ion conductivity is nontrivial to measure because it is generally hard to build a low resistance interface for ion flow. One way to

address this problem is using impedance spectroscopy, a topic that will be discussed in more detail in Chapter III.

PLEDs experienced a breakthrough when Pei and coworkers blended a polymer electrolyte consisting of a salt and polyether based polymer with a conducting polymer, essentially constructing an electrochemical cell [23]. In this system, the salt is dissolved in the polyether. This system exhibits mixed conduction mechanisms because there is electronic conduction through the conducting polymer, and ionic conduction through the polymer electrolyte. It was also shown that the turn-on threshold was much less than that in the PLED and did not depend on the thickness of the device. The electroluminescence efficiency was also higher compared with PLEDs. At the same time, low work function cathodes are required for high efficiency PLEDs and highly reactive materials such as calcium are often used. In contrast, PLECs can be fabricated with a wide range of electrode materials.

Studies [23,26] on polymer MIECs have generally agreed that the low threshold for charge injection results from movement of the mobile ions towards the electrodes, but the precise distribution of charges and corresponding electric potential profile across the device is different depending on the model used. So far, there are two major models, namely the electrochemical model [23] and the electrodynamic model[**26].** Each is supported by a number of observations. They are summarized as follows:

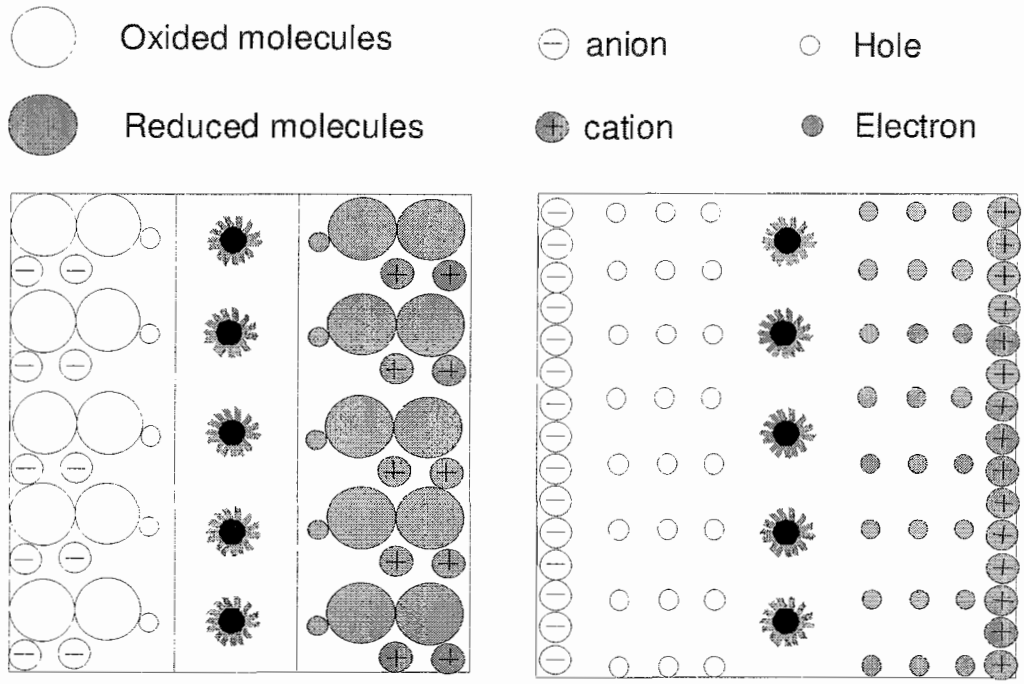

Figure.1.5 Illustrations of major difference between the (a) electrochemical model (b) and the electrodynamic model (adapted from ref.26)

According to the electrodynamic model, ions move towards the electrodes in response to the electrical field and form a region of ionic space charge when a blocking electrode is used. Ionic carrier redistribution occurs throughout the bulk of the polymer film until the local electrical field is cancelled everywhere. The accumulation of uncompensated ions near the electrode-polymer interface screens the bulk polymer from the external electrical field. Thus, the bulk of the device is field free. The strong electrical field in the region close to the interface reduces the width of the interfacial barrier drastically and enhances electronic charge injection.

In the electrochemical model, it is suggested that the ions are separated spatially. When enough voltage is applied, the polymer material close to the electrode region is

either p-doped (oxidation) or n-doped (reduction) depending on its proximity to the anode or cathode. The two doped regions create ohmic contacts at the electrodes and a PN junction forms where the two doped regions meet.

The fundamental difference between the two models is the distribution of the electrical field inside the PLEC. In the electrodynamic model, the potential drops mostly at the interface to maintain the high field that assists electronic carrier injection. While in the electrochemical model, the polymer close to the interface is doped and is therefore ohmic. An electric field builds up where electrons and holes recombine due to high resistance in this intrinsic region. These differences are illustred in figure 1.4.

Many theoretical treatments and experiments have been done to investigate how factors such as ion concentration [24, 26,63], ion species [64,65], polymer morphology [66], device processing procedures [67] and contact metals [68,69,70] affect the current-voltage relationship or emission efficiency. One feature of PLECs that assists in understanding the mechanism of their operation is that doping quenches emission, thereby enabling direct obervation of the intrinsic junction region. In devices with an open surface structure and a thick active polymer layer, the emission can be monitored in real time to study the propagation of the doping front and formation of a PN junction[71,72,73,74]. Recent progress in this direction is the fabrication of polymer LECs with bulk emission. This is realized by combining an open surface structure with either metal electrodes floated under the polymer film or with metal particles [75,76]. Impedance spectroscopy is also employed to confirm junction formation, with the

assumption that the capacitance of the device increases as a junction is formed at high enough applied bias[77,78].

To probe the profile of the electric field in the polymer directly, techniques such as electroabsorption [79,80] and electric force microscopy (EFM) [81] have also been utilized. In contrast to results from experiments showing electrochemical junction formation inside the polymer, which lean towards supporting the electrochemical model, these measurement demonstrate a high electrical field in the region close to the electrode, which is the main assumption of the electrodynamic model. The lack of a consistent description for the mechanism of PLECs limits attempts to improve their operation.

The long-standing controversy in the fundamentals of PLECs despite extensive studies reflects the complexity of the system. At the same time, it urges for systematic investigations involving carrier dynamics and comprehensive electrical characterization, which are the main focus of this work. The following section describes the strategy used herein to examine the role of ionic carriers in electronic carrier transport in MIECs including their interactions and distribution, which in turn determines the electric field distribution.

1.9 Strategy of Dissertation

In MIECs, the ionic and electronic charge carriers respond to external stimuli on different time scales. More specifically, the relaxation of ionic carriers is much slower than that of electronic carriers. However, in the time domain, both charge carrier species will contribute to the response and will hence be convoluted with each other. The first

step of this investigation, therefore, is to use impedance spectroscopy to identify ionic and electronic relaxation processes in order to study them separately. Impedance analyses of ionic carrier relaxations are carried out over frequencies ranging from 0.01 Hz to 1MHz and at temperatures ranging from 308K to 398K. Impedance analyses of electronic carrier relaxations are done at lower temperatures from 173K to 273K in order to slow down the relaxation of electronic carriers as well as to freeze the ions. In the temperature range from 173K to 273K, the ionic mobility is so low that the ionic carriers can be considered to be immobile. The relaxations of both ionic and electronic carriers show Arrhenius-type behavior and are therefore an energy-activated process. Activation energies can be extracted from the temperature dependence of their conductivities and relaxation frequencies.

The second step of the investigation probes the interactions between ionic and electronic carriers using an array of techniques in the time domain, in which the influence between them will be in full play. Each of these techniques involves driving the system away from equilibrium using a DC voltage while simultaneously probing the electronic properties of the non-equilibrium state. In the case of impedance analysis, a DC voltage is applied to the sample until a steady state is reached, and then impedance analysis is performed using a relatively small amplitude AC perturbation. Voltage and temperature dependences of the impedance are systematically investigated in the range of 0V to 0.5V and 308K to 348K, respectively. The current is monitored both during the approach to steady state and during the relaxation back to equilibrium in the time domain. The approach to steady state is monitored by measuring the transient current in response to

the DC bias, while the relaxation is measured through either a short circuit (with current measured), or an open circuit (with the potential across the system measured).

CHAPTER II

PRINCIPLES AND INSTRUMENTATION OF IMPEDANCE SPECTROSCOPY

2.1 Overview

The purpose of this chapter is to introduce dielectric relaxation processes and the instrumental setup for their measurement. A theoretical description of dielectric relaxation processes will be provided. Based on this theory, some response functions will be defined, and the experimental design introduced. A few application examples, which are related to content in Chapter III and Chapter IX, are also included in this chapter.

Relaxation, in general, is a delay in a response to a changing stimulus in a linear system. In the case of dielectric relaxation, the subject under study is often a highly resistive material with small or even negligible electrical conductivity. The stimulus applied to probe the material is frequently an electrical field that perturbs the system. The consequential evolution of the polarization in response to the stimulus is monitored to infer information about dynamics. More often than not, the response lags behind the stimulus. The physical origin of the time lag between the applied electric field and the polarization is the irreversible loss of free energy to heat. Also, a larger lag implies a slower process.

Since polarization is a quantity describing the separation of charge, and an electrical field is usually applied to separate charges, there is often some misunderstanding that the relaxation of the polarization as a function of the electrical field is due to the direct pull of the field. The relaxation of polarization is brought about by thermal motion, and consequently, the rate at which the polarization relaxes is very sensitive to temperature.

2.2 Dielectric relaxation and polarization

Some definitions are necessary before the mathematical description of dielectric relaxation is introduced. Polarization is a measure of the collective dipole moment. The dielectric response is characterized by the permittivity, ε, which is related to the polarization (P) as follows :

$$P = \varepsilon_0(\varepsilon - 1)E \qquad \text{(eq 2.1)}$$

where E is the electric field and ε_0 is the vacuum permittivity.

The polarization can be divided into two parts based on the rate of the response:

$$P(t) = P'(t) + P_\infty \qquad \text{(eq 2.2)}$$

Where $P'(t)$ is the fraction of the time-dependent polarization without contribution from instantaneous polarization , and P_∞ is the high frequency ($t \to 0$) component of the polarization given by:

$$P_\infty = \varepsilon_0(\varepsilon_\infty - 1)E \qquad \text{(eq 2.3)}$$

where ε_∞ is high frequency permittivity.

Later we are going to use the static polarization (P_s) , which satisfies:

$$P_s = P(t \to \infty)$$

$$\text{and} \qquad P_s = \varepsilon_0(\varepsilon_s - 1)E \qquad \text{(eq 2.4)}$$

Figure 2.1 shows an example of relaxation. The time dependence of the polarization can be represented by a differential equation. The polarization at any time, $P(t)$, differs from P_s because the dielectric response lags behind the field. Based on linear response

theory, the change in the rate of polarization towards equilibrium is proportional to how far it is from equilibrium. The following differential equation for a single time constant relaxation is obtained:

$$-\tau\frac{dP}{dt} = P_s - P(t) \qquad \text{or} \qquad -\tau\frac{dP'(t)}{dt} = P_s - (P'(t) + P_\infty) \qquad \text{(eq 2.5)}$$

where τ is the characteristic time describing the approach to equilibrium:

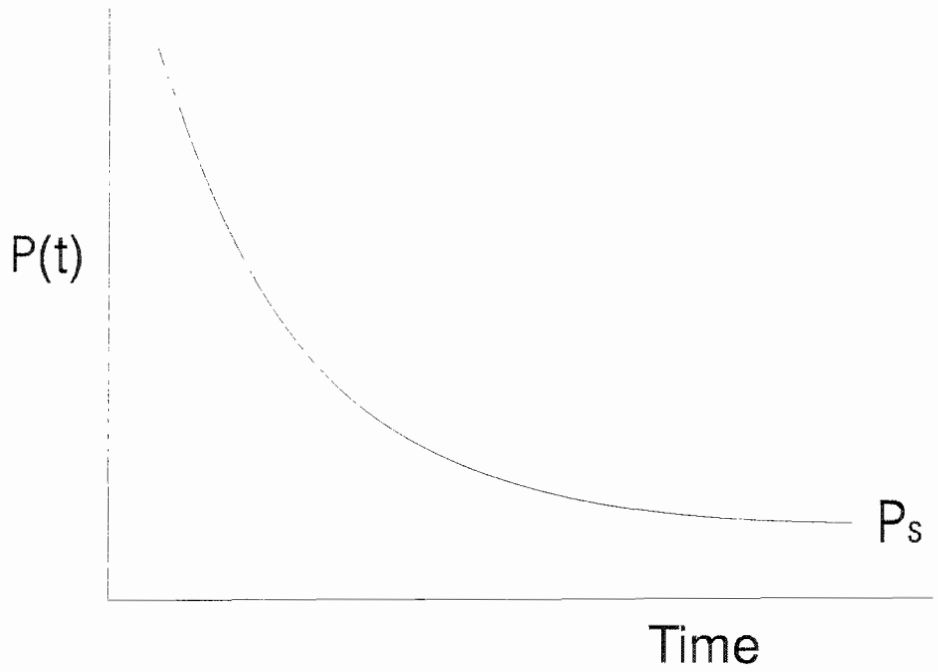

Figure 2.1 The relaxation of a dielectric material, where *P(t)* is the polarization response at some time *t*, and P_s is static polarization.

The solution to the differential equation 2.5 is the frequency dependent complex permittivity $\varepsilon^*(\omega)$, where:

$$\varepsilon^*(\omega) - \varepsilon_\infty = \frac{\varepsilon_s - \varepsilon_\infty}{1 + j\omega\tau} \qquad \text{(eq 2.6)}$$

Here the $\varepsilon^*(\omega)$ is used to emphasis that the solution to eq. 2.5 is complex. The real

part ($\varepsilon'(\omega)$) and the imaginary part ($\varepsilon''(\omega)$) of the complex permittivity in eq 2.6 are given as:

$$\varepsilon'(\omega) = \varepsilon_\infty + \frac{\varepsilon_s - \varepsilon_\infty}{1+\omega^2\tau^2}$$

$$\varepsilon''(\omega) = \frac{\omega\tau(\varepsilon_s - \varepsilon_\infty)}{1+\omega^2\tau^2} \qquad \text{(eq 2.7 a. \& b.)}$$

Eq 2.7 a&b are the Debye equations, which were first derived by Debye for molecular systems. The delay, which is characterized by the phase angle (defined in eq. 2.11), of the dielectric response introduces the loss of free energy to heat. Therefore, the tangent of the phase angle (also referred to as the loss tangent, $tan\,\delta$) is used to quantify the energy loss. It is defined as:

$$tan\,\delta = \frac{\varepsilon''(\omega)}{\varepsilon'(\omega)} \qquad \text{(eq 2.8)}$$

Therefore, using eq 2.8 a & b,

$$tan\,\delta = \frac{(\varepsilon_s - \varepsilon_\infty)\omega\pi}{\varepsilon_s + \varepsilon_\infty\omega^2\pi^2} \qquad \text{(eq 2.9)}$$

The loss tangent is also a function of frequency and usually shows a peak for a single relaxation time process. For a Debye relaxation, the peak frequency in the loss tangent (ω_{LT}) is different from the peak frequency in imaginary part of complex permittivity (ω_{EL}) The ratio between the two is given as:

$$\frac{\omega_{LT}}{\omega_{EL}} = \left(\frac{\varepsilon_s}{\varepsilon_\infty}\right)^{1/2} \qquad \text{(eq 2.10)}$$

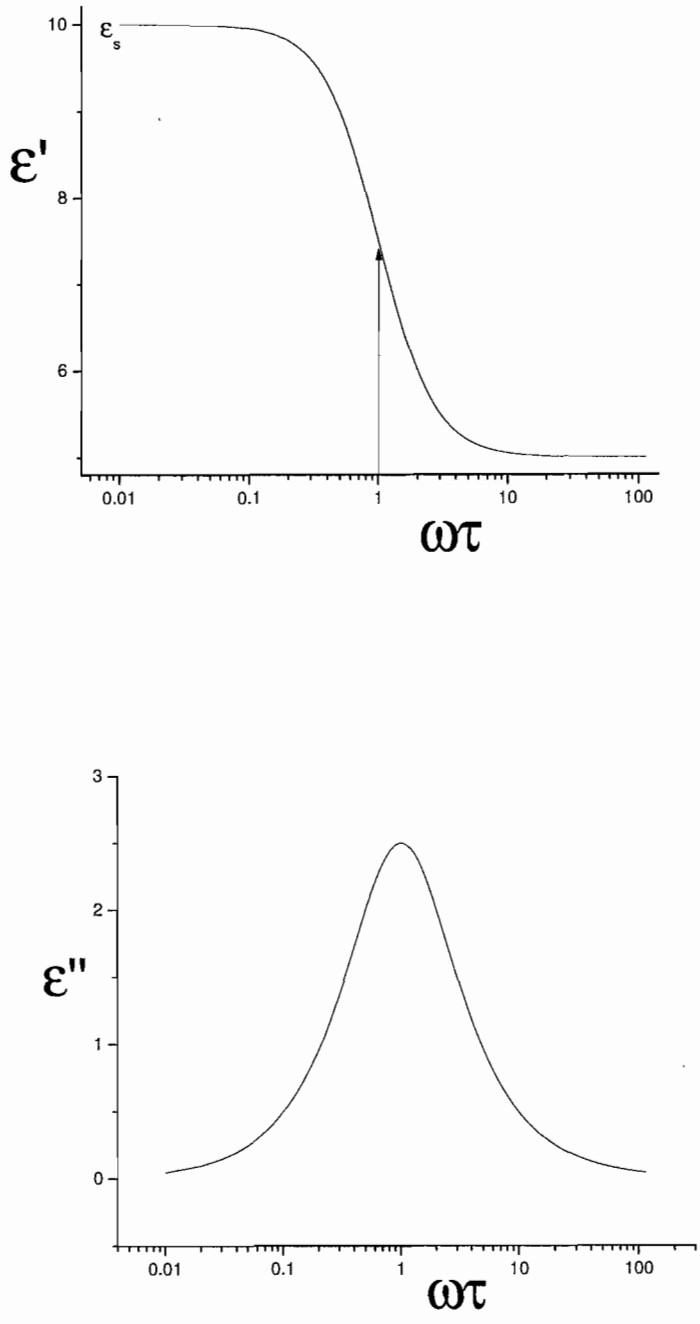

Figure 2.2 Plots of both the real (a) and imaginary (b) portions of the frequency dependent complex permittivity as function of the characteristic frequency

2.2.1 Mechanism of polarization

The introduction so far offers a generic mathematical description of a simple dielectric relaxation process and the dielectric permittivity. There are a number of different mechanisms that can contribute to polarization and hence the dielectric permittivity. This section describes those physical processes. First recall that polarization is essentially the displacement of negative and positive charge under the influence of an electric field. This displacement takes place from the atomic scale up to the molecular and even larger scale. How fast the medium can respond to an electrical field is closely related to the scale on which the dielectric relaxation occurs; generally, the larger the scale, the slower the process. The most common processes contributing to the polarization of materials are shown in figure 2.3. Electronic polarization occurs at the atomic level when the electron cloud around the nucleus of a neutral atom is displaced in shape by the electrical field. Electronic polarization generally persists around 10^{-15} s. Atomic polarization is due to vibration of atoms or ions, and is typically in the timescale of 10^{-12} to 10^{-9} s. Dipole polarization originates from the reorientation of permanent or induced dipoles along the electric field, and the time scale for this process depends strongly on temperature and is in the range of 10^{-9} -10^{-3} s for most materials. The ionic polarization is due to space-charge polarization from ion motion and occurs on a timescale longer than 10^{-3} s.

The characteristic frequencies of the processes in figure 2.3 range from 10^{-6} Hz to 10^{10} Hz. This extended range of interaction between electromagnetic waves and matter is the domain of broadband impedance spectroscopy, which enables us to gain a wealth of

information about molecular and collective dipolar fluctuations, charge transport and polarizations at both interfaces and boundaries.

In conventional dielectrics, only dipolar and electronic polarization processes are typically important. In the highly disordered ionically and electronically conductive materials studied herein, carrier polarization processes are also important. These carrier polarization processes involve a wide range of mechanisms with the common feature being that the charge carriers involved move by discontinuous hopping movement between localized sites. These carriers can be electronic carriers (electrons, holes, polarons etc.) or ionic carriers. For electronic carriers, the DC conductivity is determined by the entire network of percolation paths between the two electrodes, while at sufficiently high frequencies, the conductivity is determined by local hopping between neighboring sites. For ionic carriers, the case is similar, but ion hopping is typically much slower, and one must also take into consideration electrode polarization because most practical contacts are ion blocking.

2.2.2 Impedance-related functions

Impedance ($Z(\omega)$) is by definition a complex variable and is fully described with both magnitude and phase angle.

$$Z(\omega) = Z' + Z'' = |Z|\, e^{j\delta} \qquad \text{(eq 2.11)}$$

where Z' and Z'' are the real and imaginary part of impedance, respectively, $|Z|$ is the magnitude of impedance, and δ is the phase angle.

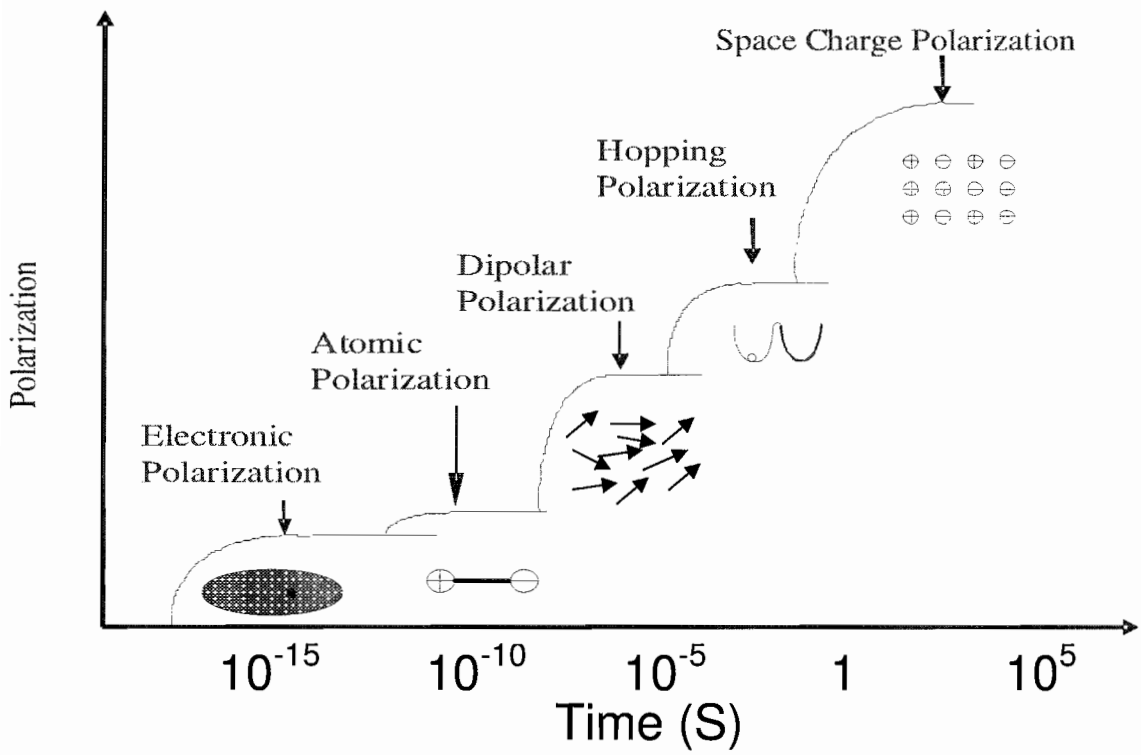

Figure 2.3 Typical polarization mechanisms as a function of time in seconds. The characteristic frequency of each process is inversely proportional to the timescale shown in the graph. The graph indicates that more relaxation processes can contribute to the polarization at longer measurement timescales, therefore the polarization is higher. With the measurement frequency range from 0.01Hz to 1MHz, only the polarization processes with timescale from 10^{-6} to 100 seconds can be detected. Processes with time scale less than 10^{-6} seconds contributes to ε_∞ in equation 2.7. Diagram adapted from reference 1.

For purely resistive behavior, the phase angle is zero, and there is no lag between the signal (voltage) and the observed response (current). In contrast, the phase angle for a capacitor is -90°, as the voltage lags behind the current. In the case of an inductor, the phase angle is +90° degrees because the current lags behind the voltage.

For the sake of convenience, there are other quantities that can be derived from impedance. A useful quantity is the admittance, which is the inverse of impedance:

$$Y(\omega)=Z^{1}=Y'+Y'' \qquad \text{(eq 2.12)}$$

where Y' and Y'' are the real and imaginary part of admittance, respectively.

It is customary to express Y in terms of resistive and capacitance components:

$$Y(\omega)=G(\omega)+jB(\omega). \qquad \text{(eq 2.13)}$$

where $G(\omega)$ is the conductance and $B(\omega)$ is the susceptance.

Susceptance is related to capacitance $C(\omega)$ as

$$B(\omega)=\omega C(\omega). \qquad \text{(eq 2.14)}$$

Complex permittivity is also related to impedance through admittance as follows:

$$\varepsilon^{*}(\omega) = j\,\omega C_0/Y(\omega) \qquad \text{(eq 2.15)}$$

where C_0 is the geometric capacitance.

2.3 Impedance spectroscopy

The mathematical description of dielectric relaxation given in the previous sections lays the foundation for introducing the experimental technique of impedance spectroscopy. In this method, a material is usually integrated into an electronic circuit

so that an external stimulus can be applied, and the corresponding electrical response can be measured. When an electrical stimulus is applied, there are commonly a multitude of fundamental microscopic processes that take place throughout, such as the transport of electrons, the transfer of electrons across an interface, the flow of neutral atoms or molecules, and the motion of ions. All these processes are coupled closely together in the time domain and give rise to an overall electrical response.

The time-dependent electrical response of a material is often transformed into the frequency domain using a Fourier Transform to separate the contributions from the different processes. There are in general three forms of stimuli that are applied: a step function of voltage, a signal composed of random noise, and a single frequency voltage oscillation.

For the step voltage, the measurement is done in the time domain, and the frequency domain response is recovered using a Fourier transform of the time-dependent current i(t) as follows:

$$Y(\omega) = \frac{1}{\Delta V} \int i(t) e^{j\omega t} dt \qquad \text{(eq 2.16)}$$

where ΔV is the amplitude of the voltage stimulus.

For a stimulus comprised of a voltage oscillation, measurements are made directly in the frequency domain. Direct measurement in the frequency domain is the major technique utilized in this work for impedance spectroscopy measurements and will be discussed in more detail in 2.3.4.

2.3.1 Data presentation

Impedance-related functions can be presented both in terms of frequency and in the complex plane. For dielectric measurement data, the choice of how the data is presented can facilitate data analysis and make more or less obvious the key parameters needed to describe the system. In a complex plane presentation, such as the Cole-Cole plot, each relaxation process corresponds to a semicircle. Therefore, it is relatively easy to identify relaxation processes in the complex plane. However, the frequency is not explicit, and it is hard to identify the relationship between the dielectric functions and the frequency. To illustrate the frequency dependence, both the real and imaginary parts of impedance-related functions are displayed in terms of frequency. Dielectric processes and their corresponding characteristic frequencies can be easily identified with this presentation.

Often the physicoelectrical model including all the processes that might be involved in the response of an electrode-material system to the applied electrical field is not available. Dielectric theory is further complicated by the fact that permanent dipoles influence each other. The field that permanent dipoles actually feel is often not just the applied field, but a local field which includes contributions from neighboring permanent dipoles. There are a number of ways to simplify the above complications and to analyze the impedance data without detailed knowledge of all the microscopic processes. One of the most common practices is to approximate the impedance-related functions by an equivalent circuit made up of ideal resistors, capacitors, and perhaps inductors. In this model, resistors are used to account for bulk conductivity, while capacitors and inductors account for processes associated with space charge polarization and interfacial

polarization. Although it is important to keep the actual physical processes in mind, this approximation is helpful in both understanding and interpreting impedance data.

2.3.2 Measurement techniques

Many techniques have been utilized to measure and analyze impedance, both in the time domain and the frequency domain[1,2,3]. In the time domain, any arbitrary time domain excitation can be used to measure the system impedance. The response of the system is recorded in the time domain, and then the time to frequency conversion is performed by either Fourier or Laplace transform. This conversion can be done either by software or by hardware.

In the frequency domain, there are a number of standard ways to measure an impedance spectrum, such as audio frequency bridges, transformer ratio arm bridges, a Berberian-Cole bridge, direct measurements using an oscilloscope, phase-sensitive detection, and automated frequency response analysis. In this work, only frequency response analysis will be introduced. Frequency response analysis is an example of measuring the system response and then performing Fourier transforms using hardware. It is done by correlating the system response with two synchronous reference signals, one of which is in phase with the sine-wave perturbation while the other is shifted 90° in phase. The principles of a frequency response analyzer can be illustrated in the figure 2.4

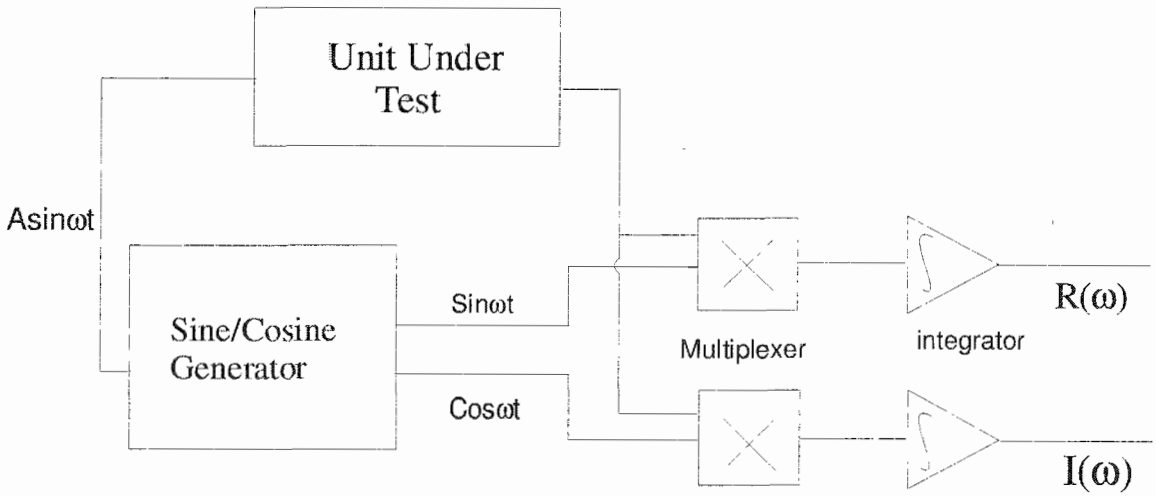

Figure 2.4 The schematic of a transfer function analyzer. Small amplitude signals go to a multiplexer along with the response from the test unit. The products are then integrated to get the real ($R(\omega)$) and imaginary parts($I(\omega)$) of the impedance.

2.4 Applications of impedance spectroscopy

Impedance spectroscopy has been used to probe a broad range of materials, including ionic conductors, disordered materials, polymer electrolytes, electrolytic liquids, conducting polymers, PN junctions and other dielectric materials.[4,5,6,7,8,9]. Several applications of impedance spectroscopy that are relevant to the work herein are introduced below.

2.4.1 Impedance spectroscopy of ionic conductors

The rigorous theoretical treatment of impedance spectroscopy requires the careful study and mathematical solution of transport equations, with knowledge of all quantities

and parameters (i.e. carrier concentration and mobility, recombination rate, electrode transparency, field distribution, etc.). The first attempts of this kind were done by Chang and Jaffe in 1952[10], followed shortly by Friauf [11]. Chang and Jaffe studied the situation where positive and negative carriers (of equal equilibrium bulk concentration) discharged at the electrodes to a degree determined by blocking or discharge parameters. Friauf gave close-form solutions for the over-all current in his analysis, but did not derive and investigate expressions for parallel capacitance and conductance holding for all frequencies. At about the same time, J.R.MacDonald published an exact, closed-form expression for the admittance of a charge-carrying liquid or solid between two plane parallel completely-blocking electrodes[12]. Work focusing on solid dielectrics was also done by assuming that negative charges were mobile and completely disassociated, while positive charges remained fixed[13]. One clear message that could be derived from the studies mentioned above was that the electrode dynamics are very important in understanding polarization in the low frequency region. The electrode polarization in a device where an active layer is sandwiched between two electrodes is essentially the increased concentration of the charge carriers in the region that is close to electrodes due to the slowness of the electrode reactions compared to the rate of migration of the carriers through the bulk of the active layer. The electrode dynamics can be quantified with the transparency variable ρ.

A model that includes every aspect of a dielectric system is in general extremely complex. In practice, certain assumptions based on the system under study are used to simplify modeling. Careful analysis based on an appropriate model can generate a wealth

of information about the system. The model that is presented here was first developed by J.H.Beaumont and P.W.M.Jacobs to investigate the polarization in potassium chloride crystals[14]. It can be generalized to any system with the following properties:

- There is a certain rate of carrier discharge across the electrode
- Only ions of one sign are mobile
- Generation and recombination effects are ignored.

The continuity equation is

$$\frac{\partial n}{\partial t} = D\frac{\partial^2 n}{\partial x^2} + \mu\frac{\partial (nE)}{\partial x} \qquad \text{(eq 2.17)}$$

Where $n(x,t)$ is the concentration of mobile ions, and μ and D are the mobility and diffusion coefficients, respectively. The carrier concentration n and the electrical field E are related by the Poisson equation:

$$\frac{\partial E}{\partial x} = \beta(n_0 - n) \qquad \text{(eq 2.18)}$$

where n_0 is carrier concentration in equilibrium.

The current density J consists of contributions from both the drift of carriers under the electrical field and diffusion due to concentration gradient.

$$J = eD\frac{\partial n}{\partial x} + e\mu nE \qquad \text{(eq 2.19)}$$

The discharge current at the boundaries (from $x=0$ to $x= L$) can be written as:

$$J(0,t) = \rho e\Delta n(0,t)\frac{D}{L}$$
$$J(L,t) = -\rho e\Delta n(L,t)\frac{D}{L} \qquad \text{(eq 2.20)}$$

Eqs 2.20 and 2.19 can be solved with the following boundary conditions:

$$eD\frac{\partial n}{\partial x} + e\mu nE = -\rho e\Delta n\frac{D}{L}$$
$$eD\frac{\partial n}{\partial x} + e\mu nE = \rho e\Delta n\frac{D}{L} \qquad \text{(eq. 2.21)}$$

The differential equations can be linearized if the higher harmonics are neglected.

$$n(x,t) = n_0(x) + n_1(x)e^{i\omega t}$$
$$E(x,t) = E_0(x) + E_1(x)e^{i\omega t} \qquad \text{(eq. 2.22)}$$

The solution for capacitance is then:

$$C_p = (\frac{\pi kT}{\varepsilon n_0})^{1/2}\frac{4\sigma^2}{\omega^2 L^2 e}\{[1+\frac{\pi kT}{\varepsilon n_0}\frac{4\sigma^2}{\omega^2 L^2 e}(2+\rho)^2]\}^{-1} \qquad \text{(eq. 2.23)}$$

where σ is the DC conductivity, ρ is the electrode transparency, with $\rho = 0$ to be completely blocking, and $\rho = \infty$ to be completely non-blocking.

It is worthwhile to point out the role of the electrode transparency in the AC capacitance. Eq.2.23 implies that discharge at the interface (ρ nonzero, Faradic process) reduces the AC capacitance when compared with the completely blocking case.
The characteristic frequency is thus:

$$f = (\frac{\pi kT}{\varepsilon n_0})^{1/2}\frac{2\sigma(2+\rho)}{eL} \qquad \text{(eq. 2.24)}$$

2.4.2 Space charge polarization and diffusion capacitance

Polarization involves the physical separation of charge, and therefore, it creates space charge when the electrodes are not reversible. This scenario can be described with a bi-

stable model. Frohlich [15] first tried to ignore the electrostatic interactions and proposed a scenario in which the potential energy as a function of distance has two minima, therefore forming potential wells. He asserted that a particle of charge may be in one or other of two sites with a physical distance of *d*. Particles and potential wells are treated as a microscopic assembly of N bi-stable dipoles in which particles exchange energy with each other and the directions of the dipoles fluctuate. The jumping rate of the particles is determined by the depth of the potential well, the electrical field, temperature and trial frequency. An electrical field creates a potential difference between the two sites, which generates a further difference in the number of particles sitting in site 1 versus site 2. This gives rise to a non-zero polarization. A relaxation equation can be derived by noticing that the change in the number of dipoles in 1 is equal to the outflow to 2 less the inflow from 2. This model offers the physical meaning for the relaxation time, which is the reciprocal of the frequency of jumps over the potential barrier.

In the situation where charge neutrality holds, transport of charge carriers occurs by a nearly-free diffusive mechanism and gives rise to a diffusion capacitance[16,17]. The charge carrier motion is driven by its concentration gradient. The diffusion current in one dimension, *x*, is given as:

$$J(x,t) = -D\frac{dn}{dt} \qquad \text{(eq 2.25)}$$

The continuity equation without recombination is in the form:

$$\frac{dn}{dt} = -\frac{dJ}{dx} = D\frac{d^2n}{dx^2} \qquad \text{(eq 2.26)}$$

The carrier concentration at the electrode charge is injected is assumed to be constant, while that at other electrode is assumed zero. The solution for the carrier concentration with the above boundary conditions is as follows:

$$n(x) = n(0)(1 - \frac{x}{W}) \qquad \text{(eq 2.27)}$$

where W is the thickness of the device.

With a small amplitude signal, the current can be expressed as:

$$J'(\omega) = \frac{\omega}{2}(1+i)V' \qquad \text{(eq 2.28)}$$

and therefore the complex admittance is:

$$Y(\omega) = \frac{J(\omega)}{V'} = \frac{\omega}{2}(1+i) \qquad \text{(eq 2.29)}$$

The relationship between the complex dielectric permittivity is $\varepsilon(\omega) \propto \omega^{-\frac{1}{2}}$, which is very different from the Debye relaxation. The nearly field-free case can happen in a PN junction in forward bias[18], as well as in a LEC in which the external field is screened by the redistribution of ionic carriers[19,20].

2.4.3 Semiconductor interfaces

The application of impedance spectroscopy to semiconductor devices is described because it is used in studying the conducting polymer-inorganic semiconductor interfaces, as presented in Chapter IX. The following is a brief introduction to the theoretical base for these measurements.

The polymer-inorganic semiconductor interfaces in this work are considered to be Schottky contacts because the polymer does not support charge depletion and acts as a metal when in contact with inorganic semiconductors.

The depletion region of a Schottky contact behaves in some aspects as a parallel-plate capacitor. The Schottky barrier height is one of the determining factors of capacitance. Therefore, the capacitance of a Schottky contact is measured in order to extract information about the Schottky barrier height. In the case of an n-type semiconductor contacted to a metal, the applied bias changes the width of the depletion region, the number of uncompensated donors in the depletion region and consequently the built-in electric field. This gives rise to a displacement current and a differential capacitance:

$$C^{-2} = \frac{2}{q\varepsilon_s N_d A^2}\left(V_{b0} + V_{app} - \frac{k_B T}{q}\right) \qquad \text{(eq 2.30)}$$

where ε_s is the dielectric constant of the n-type semiconductor, N_d is the carrier concentration (also referred to as the dopant density), V_{b0} is the diffusion voltage, A is the area of the contact, T is the absolute temperature in K, and k_B is the Boltzmann constant. Ideally, a plot of C^{-2} versus V_{app} is a straight line, and the intercept to the applied bias axis is $V_{d0}+V_r-kT/q$, where V_r is the Schottky barrier height. Also, from the slope of the intercept, the dopant density N_d of the semiconductor can be extracted.

CHAPTER III

IMPEDANCE ANALYSIS OF AN ANIONICALLY FUNCTIONALIZED POLYACETYLENE BETWEEN METAL ELECTRODES

3.1 Overview

Impedance spectroscopy has been used extensively to study both solid state and electrochemical systems in order to investigate conduction mechanisms [1,2]. Ionic crystals and electrolytes are often the subjects of these studies, in which impedance spectroscopy has been proven very effective[3,4,5,6]. Impedance spectroscopy has also been used recently to probe the properties of ionically and electronically conductive polymers, especially in light-emitting electrochemical cells (LECs) and fuel cells due to their powerful application potential and their many advantages over traditionally used materials [7,8].

Ionically functionalized conjugated polymers, as a new form of inherently mixed ionic-electronic conductors, are a unique system for studying interactions between ionic and electronic carriers. Understanding the fundamentals of mixed ionic-electronic conductors (MIECs) first requires the knowledge of the dynamics of both ionic and electronic carriers, respectively. In this chapter, systematic studies of the dynamics of anionically functionalized polyacetylene (P_A) between two metal electrodes (Au|P_A|Au, showed in figure 3.1) have been carried out using the impedance spectroscopy at temperatures ranging from 308 to 398K. Microscopic processes detected by impedance measurements are analyzed and identified. Information such as ion concentration, ionic DC conductivity, and ion hopping frequency are extracted from modeling both the electrode and ion hopping polarization processes[9]. The transport of ions in the polymer

is also explained in the context of the jump relaxation model[10].

3.2 Sample preparation and measuring techniques

3.2.1 Sample preparation

The anionic conjugated polymer P_A was synthesized by the route of ring-opening metathesis polymerization (ROMP) using an appropriately functionalized cyclooctatetraene (COT) as the monomer. The polymer was subsequently dissolved in purified methanol. A spin-coating technique was then used to deposit a film of P_A in a controlled manner onto a glass slide with a gold film as the electrical contact. The glass slide was cleaned prior to this deposition process by soaking in concentrated hydrogen chloride for at least four hours, followed by rinsing with deionized water. The slide was then soaked in the methanol for more than 15 minutes and then dried. Two metal films were evaporated onto the glass slide under high vacuum (10mTorr): 20 Å of Cr was first evaporated followed by 120 Å of Au. The bottom electrode contact was defined by a physical mask with an area of $0.12cm^2$. To make a film, a polymer solution of 10 μL was deposited onto the prepared glass slide spinning at speed of 700 rpm. The methanol in the polymer solution evaporated in a few minutes and the film color was observed to change from deep blue to golden. The glass slide-polymer structure was then stored in vacuum (20 mTorr) for at least 8 hours. A top electrode contact was made by evaporating a 10nm Au film onto the polymer. The resulting structure is showed schematically in figure 3.1. The sample was kept under vacuum for at least 4 hours, and was then transferred into a

sealed stainless canister where the sample was kept under vacuum (20 mTorr) and annealed at 398K for 8 hours. These procedures produced a consistent polymer thickness of 200nm, as measured by a Dektak profilometer. The samples were confirmed to be intact during the annealing process by spectroscopic measurements in the visible wavelength before and after annealing.

3.2.2 Measurement techniques

Impedance analysis was carried out using a Solartron 1260 impedance analyzer coupled with a Solartron 1294 dielectric interface. This set-up can measure impedances as high as 1 Tohm. The metal container encasing the sample was stored in a Sun environmental chamber for precise temperature stability and control. Impedance spectroscopy was conducted in the temperature range from 308K to 398K, with a step of 10 degrees. At each temperature, samples were swept in the linear frequency range from 1Mhz to 0.01Hz. Experimental control and data collection were done with the SMART software package provided by Solartron Interfaces. Dielectric functions were then calculated from impedance magnitudes and phase angles, based on their relationships introduced in section 2.2.2 of Chapter II.

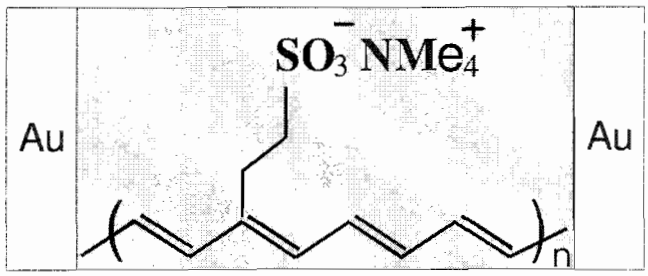

Figure 3.1 Sample structure diagram, with chemical structure of sulfonate tetramethylammonium polyacetylene shown in the active film layer in green. The Au is used for metal electrode on both sides.

3.3 Experimental results

3.3.1 Impedance-related functions and dielectric relaxation processes

Figure 3.2 shows the real part of the complex permittivity (ε') for the Au|P_A|Au sandwich structure. The dielectric response of this structure shows three dielectric relaxation processes in the angular frequency range of 0.06-600000 Hz and at temperatures from 308K to 398K. Despite some qualitative differences, the overall shape of ε' is very similar with temperature over the range of 308K to 398K, which justifies the using the data at a single temperature to describe the main features.

At 398K, three dielectric relaxation processes (corresponding to frequency ranges 6MHz-10KHz, 10KHz-20Hz, and below 20Hz respectively) are observed in the ε' spectra. Each process is characterized by a dispersion in ε' (therefore polarization) as described in figure 2.3.

Very different thickness dependences are observed among the three dielectric relaxation processes as we can see in figure 3.3, which showed the capacitance spectra of samples with various thicknesses at 398K,. The capacitance from 6MHz to 10KHz decreases significantly when samples are thicker. In the 10KHz to 20Hz region, thickness dependence of the capacitance is still present at the high frequency end, but it gradually diminishes as the frequency is lowered. Eventually the capacitances of samples with various thicknesses converge at 20Hz. Above descriptions imply a bulk-related dielectric relaxation process in the 6MHz to 10KHz, and an interfacial process at frequency region from 10KHz to 20Hz. Considering the structure under study is an ion-

functionalized polyacetylene between two ion-blocking metal electrodes, the dielectric relaxation process in 6MHz to 10KHz is assigned to the geometric capacitance charging, and that in the 10KHz to 20Hz region is assigned to the electrode polarization of ionic carriers. Further evidences in support of these assignments will be discussed soon after.

The AC conductivity (σ) spectra show behaviours that are consistent with the aforementioned assignments. Using 398K as an example, the electrode polarization induces a deduction in σ at 100Hz after a plateau in higher frequencies up to 10KHz. With all temperatures included, the high frequency σ around 1 MHz exhibited little temperature dependence, as expected for the geometric capacitance charging.

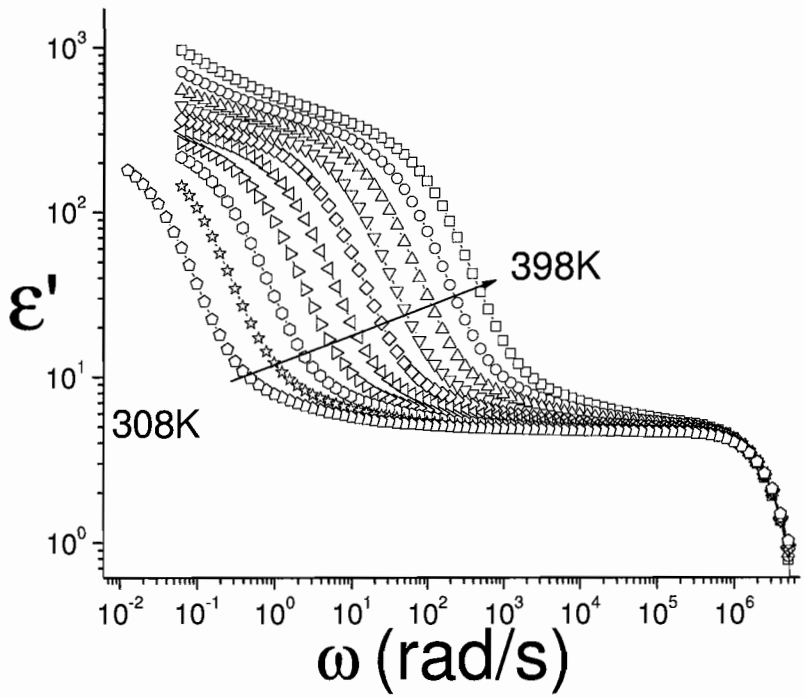

Figure 3.2 Frequency dependent ε' at temperatures from 308K to 398K. Sample is 200nm in thickness.

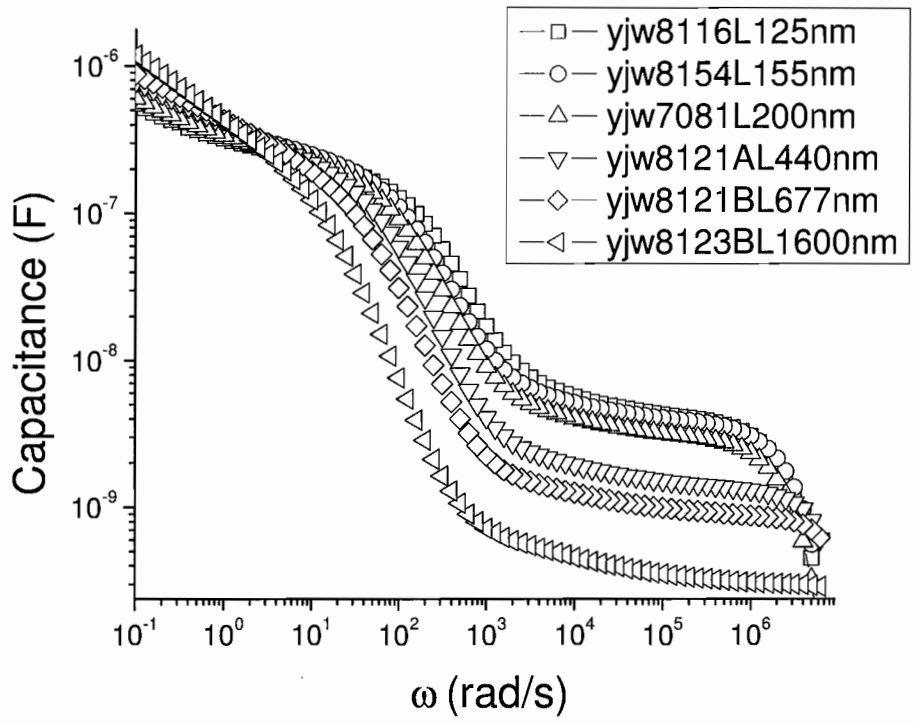

Figure 3.3 Thickness dependence of capacitance spectra. Sample thicknesses vary from 125nm to 1600nm.

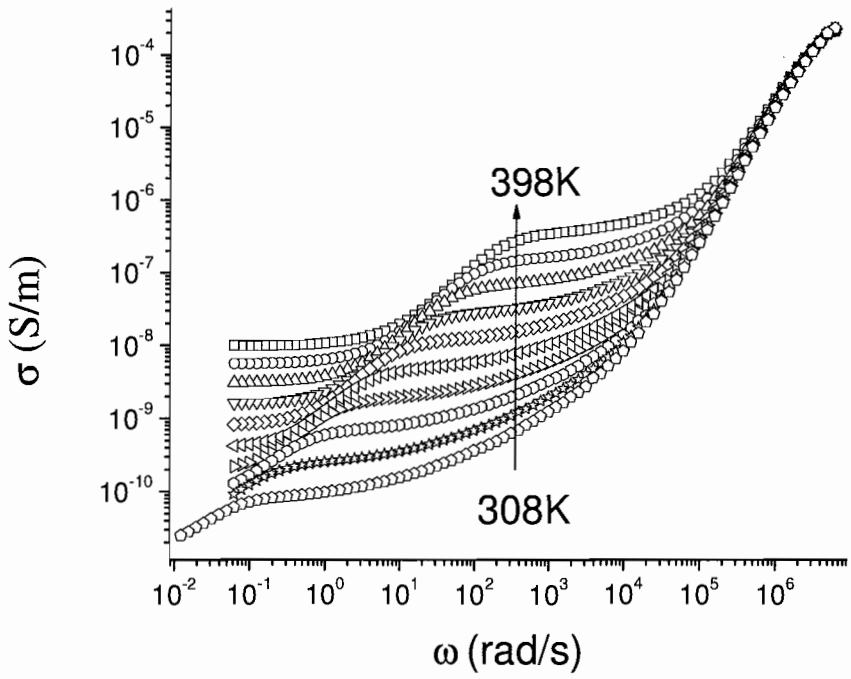

Figure 3.4 Frequency dependent σ from T=308 to T=398 K, stepped by 10 K. Sample thickness is 200nm.

3.3.2 Characteristic frequencies

As discussed in the section 2.2 of chapter II, two sets of characteristic frequencies can be obtained from the impedance-related functions, those from the imaginary part of the complex permittivity ε' (ω_{EL}) and those from the loss tangent (ω_{LT}). As we can see from figure 3.5, peaks in the ε'' are obscured by another process in lower frequencies at 398K, and even more so at lower temperatures. The value of ω_{EL} is then extracted from the derivative of ε'. Peaks in the loss tangent are more well defined (showed in figure 3.6) and ω_{LT} can be identified easily.

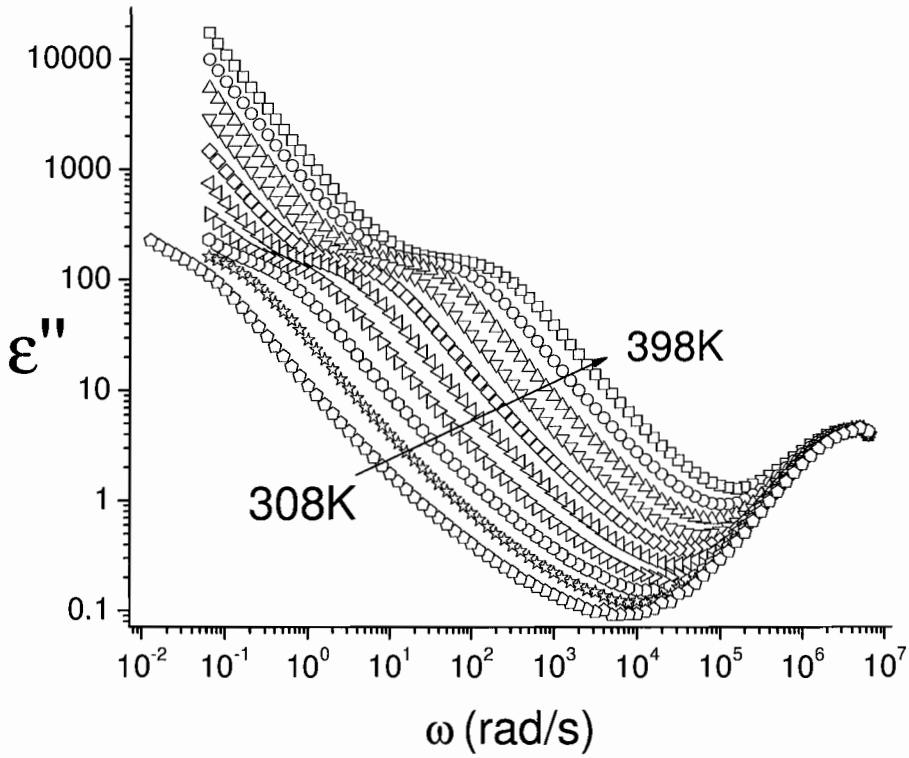

Figure 3.5 Frequency dependent ε'' spectra at temperatures from 308K to 398K. Sample is 200nm thick. Peaks predicted by Debye model are obscured by another dielectric process in the lower frequencies.

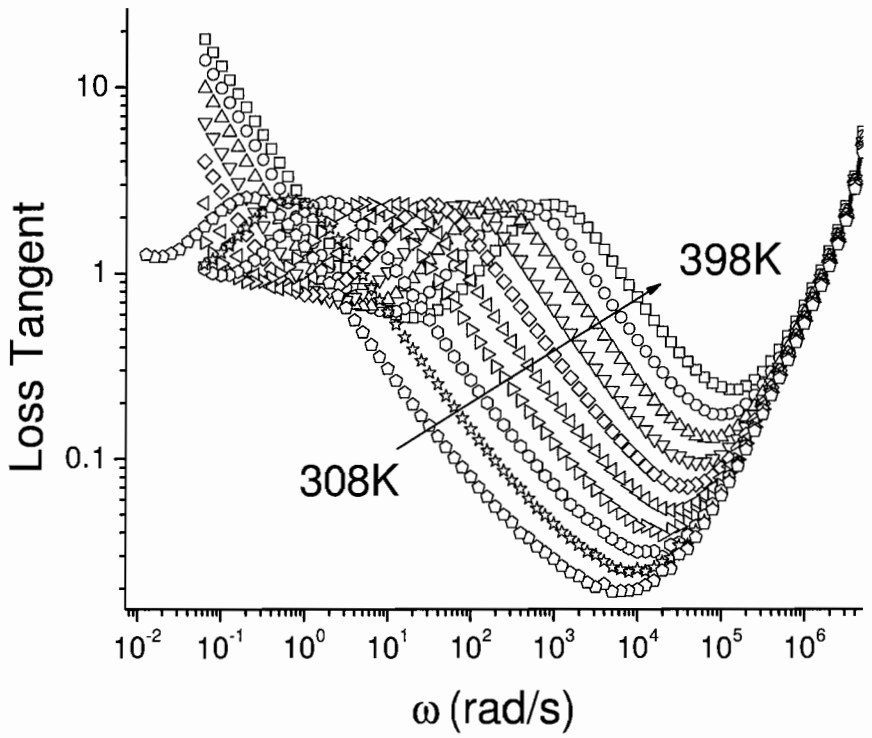

Figure 3.6 Loss tangent spectra at temperatures from 308K to 398K. Sample is 200nm thick. Temperature dependent ω_{LT} corresponds to peak in loss tangent in each temperature.

Temperature dependence of both sets of characteristic frequencies (ω_{LT} and ω_{EL}) followed the Arrhenius temperature dependencies with an activation energy of 0.97eV, as showed in figure 3.7.

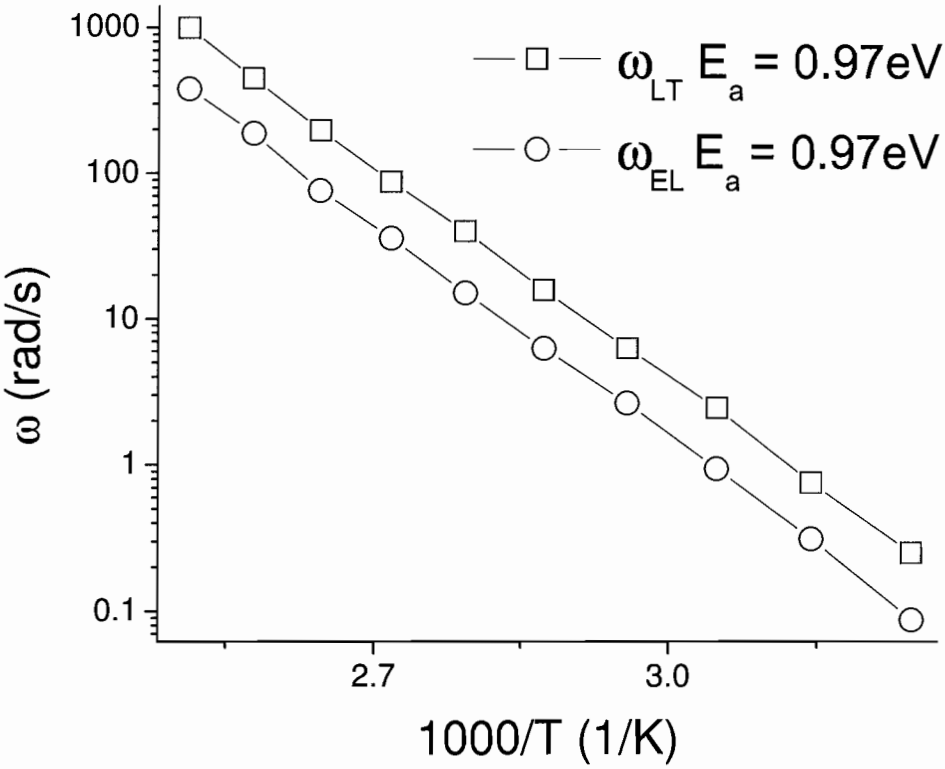

Figure 3.7 Temperature dependence of ω_{EL} and ω_{LT}, both with E_A=0.97eV.

Five samples, all with thicknesses of about 200nm, were measured. The ω_{LT} of these samples are highly reproducible, as showed in figure 3.8.

A comparison of the dielectric response frequency of samples with various thicknesses reveals that ω_{LT} depends on sample thickness as well. As shown below in figure 3.9, overall ω_{LT} decreases when samples are thicker, while the slopes of ω_{LT} - *1/T* relationship remain the same.

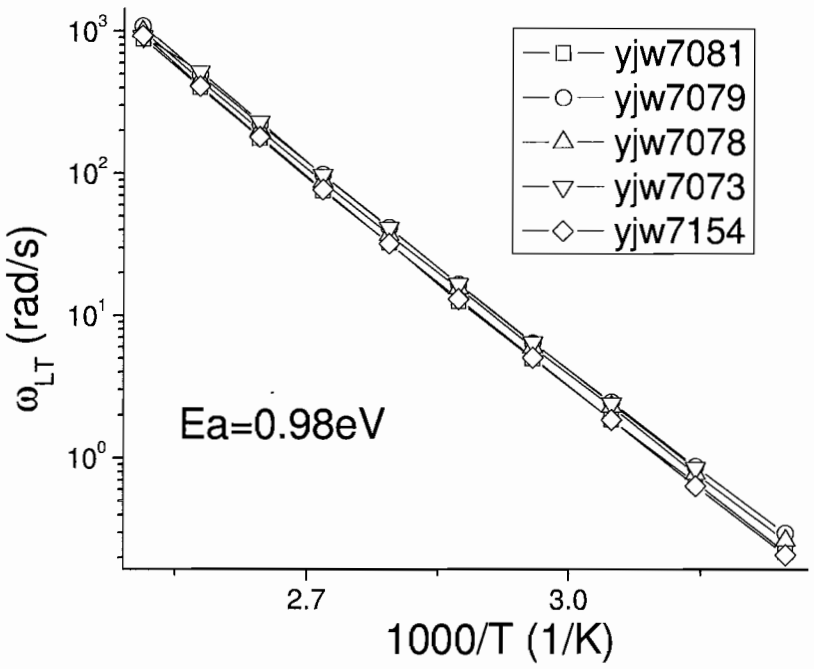

Figure 3.8 The temperature dependence of ω_{LT} for 5 samples with thickness of about 200nm. The results reflect remarkable reproducibility from sample to sample, implying well controlled sample preparation and test procedures.

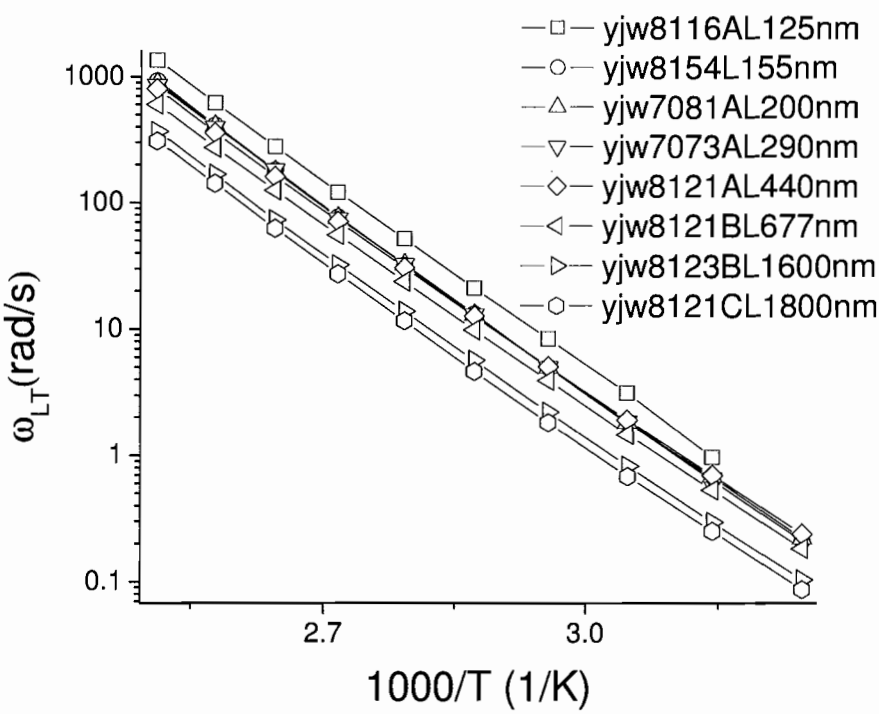

Figure 3.9 The thickness dependence of ω_{LT}. There is a clear and consistent trend that ω_{LT} decreases when sample is thicker.

3.4 Discussion

3.4.1 Assignments of dielectric relaxation processes

As we saw already, the thickness dependence of the impedance-related functions is very informative in connecting them to the specific dielectric relaxation processes. The thickness dependence of the AC impedance is analyzed in details in this section to confirm the assignments of dielectric relaxation processes as described in section 3.3.

The thickness dependence of ω_{LT} in figure 3.9 can be understood with equivalent circuit analysis. The behavior of the system comprised of ionically functionalized polyacetylene thin film between two metal electrodes can be described as in figure 3.10.

The three branches are included to best represent the microscopic processes in the system. Each component and its connection to corresponding microscopic processes are described with details in the figure 3.10. Increasing the thickness induces the following changes: the ionic resistance (R_2) increases and the geometric capacitance (C_0) decreases. At the same time, the double layer capacitance is unchanged. Considering the following relationships:

$$\omega_{EL} \propto \frac{2\pi}{R_2 C_{dl}} \qquad \text{(eq. 3.1)}$$

and the relationship between ω_{EL} and ω_{LT} given in eq. 2.10, we have:

$$\omega_{LT} \propto \sqrt{\frac{2\pi}{R_2 C_{dl}}} \propto (\frac{1}{L})^{\frac{1}{2}} \qquad \text{(eq. 3.2)}$$

It is expected that ω_{LT} is lower in thicker samples, while frequency related to the geometric capacitance charging is expected to be higher.

The above predictiona are confirmed by the conductivity spectra of samples with thickness of 125nm, 280nm, 677nm and 1600nm respectively. As indicated by the arrows in the figure 3.11, ω_{LT} is moving to lower frequencies, while the relaxation frequency of the geometric capacitance charging shifts to the higher frequencies, as sample thickness increases.

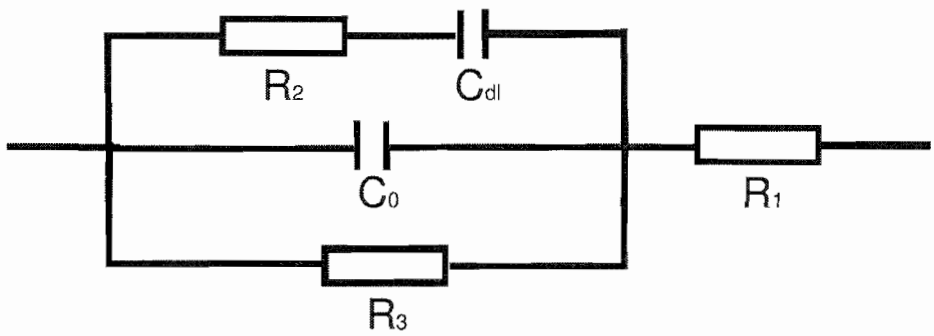

Figure 3.10 The equivalent circuit of the system, where C_0 is the geometric capacitance, R_1 is the contact resistance, C_{dl} is the double layer capacitance, R_2 is the bulk resistance of the active carriers, and R_3 is the electronic carrier transport resistance. Geometric capacitance and double layer capacitance are considered to be in parallel because the charges they store are additive to each other. The bulk resistance (R_2) is related to the thickness in that thicker samples have higher resistance, while the double layer capacitance is mostly a function of the ion concentration and temperature and does not depend on the thickness. The geometric capacitance is inversely proportional to the the thickness. Both the electrode polarization and the geometric capacitance charging can be modeled by the equivalent RC circuits, which are affected by the sample thickness. The connection between these microscopic relaxation process and the thickness through the equivalent circuits is the source of the thickness dependence of impedance spectroscopy.

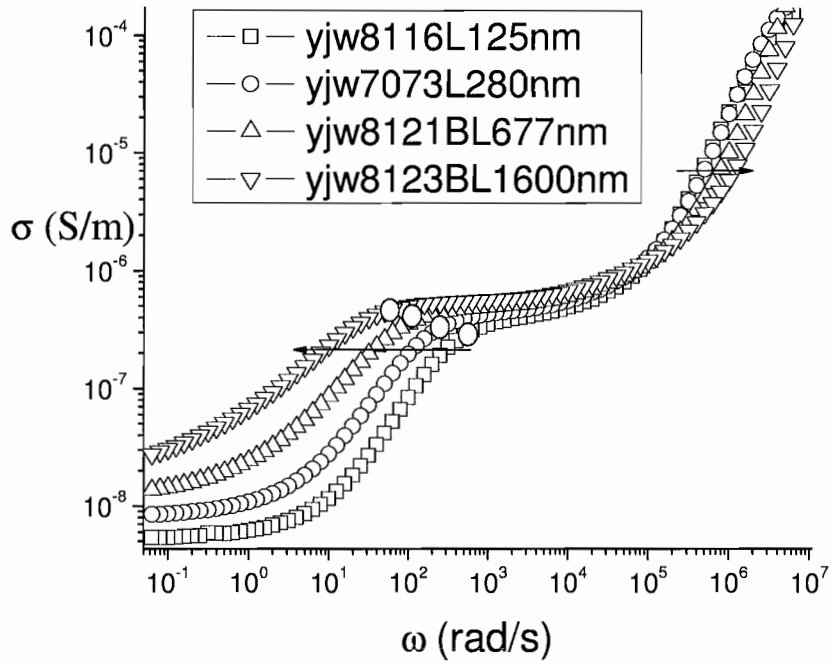

Figure 3.11 Frequency dependent σ at 398K for samples with various thicknesses (125 nm to 1600 nm). As indicated by the arrow, the transition point (as labeled with the gray dots) is moving towards the lower frequency as the sample thickness is increasing. At the same time AC conductivity curve in the high frequency region is shifting to the higher frequency when the sample is thicker.

Analysis of the equivalent circuit shown in figure 3.10 also predicts that the ω_{LT} scales $L^{-1/2}$, as indicated in eq. 3.2. This is confirmed by examining the thickness dependence of ω_{LT}, as shown in figure 3.12. A power of 0.49 is obtained from the fitting the frequency vs *1/L* in the log-log scale.

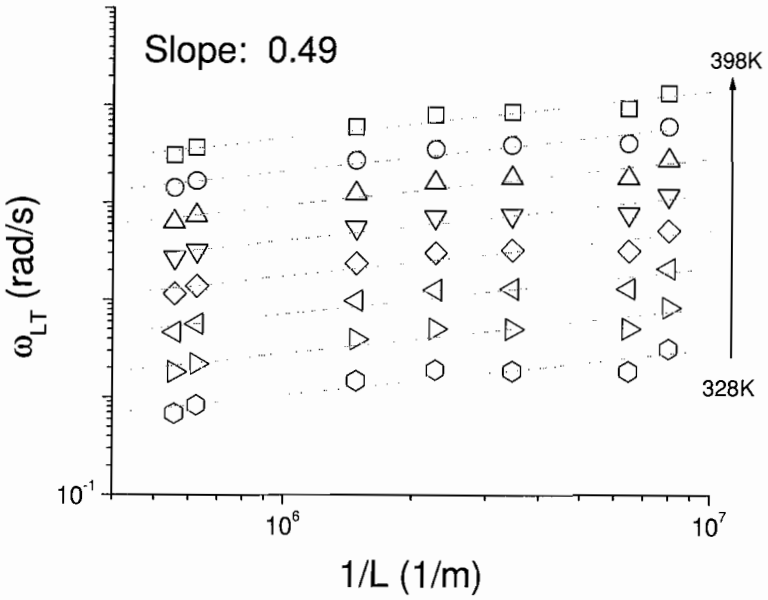

Figure 3.12 The thickness dependence of the ω_{LT}. The slope is about 0.5 consistent with the relationship showed in eq. 3.2.

The analysis discussed so far argues that the dielectric relaxation processes present in the AC impedance are the geometric capacitance charging and the electrode polarization. The active charge carriers contributing to the electrode polarization are believed to be the ionic carriers based on the following evidences:

1. ω_{EL} and ω_{LT} are very low and unlikely to be related to the electronic carriers. Impedance analysis at temperatures from 153K to 263K will be included in Chapter IV, where the relaxations of the electronic carriers are investigated.

2. ω_{EL} and ω_{LT} of unbaked samples are higher when compared with those of baked samples, which is consistent to the fact that the ion mobility is improved the residual

solvent from the spin coating process, which is then removed upon baking.

By assigning the frequency dependent behaviors in each region, further analysis can now be performed to extract information about ion dynamics.

3.4.2 Scaling properties

As mentioned previously, the frequency dependent conductivity at temperature between 308K and 398K are similar in shape, even though ω_{EL} depends heavily on the temperature. To see if the ion conduction mechanism changes with the temperature, the AC conductivity is scaled by the DC conductivity of ions ($\sigma_{DC,}$ which is defined as the conductivity at ω_{LT} at each temperature). The resulting scaled plot is shown in figure 3.13, which clearly shows that σ at these temperatures falls into one master curve in the range from 10^{-6} to 10^{-8} after the scaling process The overlay implies that the relaxation mechanisms are temperature-independent[11,12].

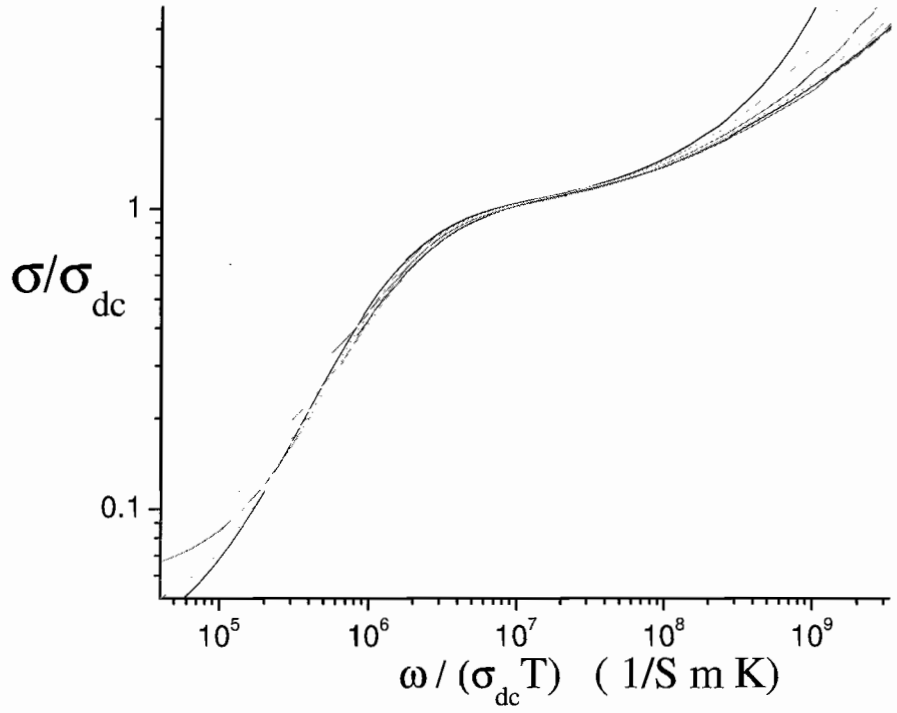

Figure 3.13 Temperature dependent σ from 308K to 398K normalized by the ionic DC conductivity. The σ in the region corresponding to the ion hopping processes converges to one single curve in the range from 10^{-6} to 10^{-8} even the temperature spans from 308K to 398K. This implies that the conduction mechanisms do not change with temperature.

3.4.3 Electrode polarization model

In studying the ion transport dynamics, it is often challenging to separate out the influences of the concentration and mobility on the ionic conductivity[13,14]. Modeling the electrode polarization can be used to extract a wealth of information, including the Debye length, ion concentration, and ion mobility[15,16]. Some relationships typically used in this modelling need to be introduced first.

From the relationship between the double-layer capacitance and the geometric capacitance, we have:

$$\frac{\varepsilon_s}{\varepsilon_\infty} = \frac{L}{2L_D} \qquad \text{(eq. 3.3)}$$

Combining eq. 2.10 and 3.3 yields:

$$\omega_{LT} / \omega_{EL} = \sqrt{\frac{L}{2L_D}} \qquad \text{(eq. 3.4)}$$

Quantities such as ω_{LT}, ω_{EL}, the sample thickness L, and ε_∞ can be measured. The Debye length is then readily calculated with eq. 3.4. In addition, the Debye length L_D, is related to other quantities as follows:

$$L_D = \frac{1}{e}\sqrt{\frac{\varepsilon_\infty \varepsilon_0 kT}{n_0}} \qquad \text{(eq. 3.5)}$$

In this equation the ε_∞ is obtained from the high frequency data. The effective ion concentration is the calculated using on eq. 3.5. The following table shows the results from such modeling:

Table 3.1. Results from modeling with the electrode polarization

T (K)	ω_{LT} rad/s	ω_{EL} rad/s	Debye Length (nm)	Ion Concentration ($1/cm^3$)
398	928.62497	90.05338	0.72882	2.21711E26
388	410.24222	40.78496	0.76599	1.82038E26
378	180.23551	18.98891	0.86024	1.33079E26
368	77.07976	8.33681	0.90661	1.12271E26
358	31.9404	3.63873	1.00582	8.57632E25
348	13.04789	1.52771	1.06243	7.29756E25
338	5.032	0.60399	1.11656	6.3082E25
328	1.84816	0.21068	1.00707	7.39995E25

3.4.4 Jump relaxation model

The AC conductivity in disordered materials is characterized by a strong dispersion, as reported by the large number of experimental results [17,18,19,20,21]. The following are general features of the AC conductivity that are often observed in a disordered material:

a. At the high frequencies, the frequency dependent AC conductivity obeys the power law .

b. At lower frequencies, there is a gradual transition to a frequency independent conductivity.

c. the DC conductivity and the characteristic frequency usually show Arrhenius-type behaviour with the same activation energy.

d. The conduction mechanism is temperature independent, as implied from the fact that the impedance-related functions can be normalized to a master curve by using the characteristic frequency.

The jump relaxation hopping model that was developed while studying ionic conductivity of glasses can accommodate all of the above mentioned features very well. Clearly all of the above features were observed in P_A between metal electrodes, which justifies the application of the jump relaxation hopping model to this model.

The jump relaxation hopping model is based on two closely-related processes that can happen in disordered electrolyte materials. The first is the correlated forward-backward hopping sequences which give rise to the AC conductivity dispersion, while the second is the jump relaxation processes which contribute to a non-zero DC conductivity and non-

Debye relaxation. The overall AC conductivity including contributions from both hopping processes is as follows:

$$\sigma(\omega) = \sigma_{DC}(1 + (\frac{\omega}{\omega_0})^n) \qquad \text{eq. (3.6)}$$

where ω_0 is the ion hopping relaxation frequency, σ_{dc} is the ion DC conductivity, and n is a power index with a value between 0 and 1.

Figure 3.14 illustrates the potential wells where the correlated forward-backward hopping process and jump relaxation process happen.

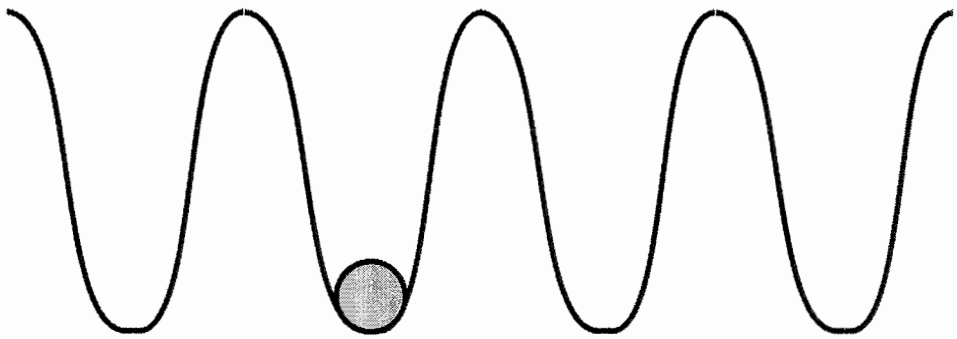

Figure 3.14 The schematic representation of single particle sitting in a potential well. Particle (black circle) can hop forward or backward through thermal activation.

Each ion has a cage-effect minimum due to their Coulomb interactions with environment. An ion hops from the minimum site, for example (A), to the neighbouring site (B) with the assistance of a thermal activation energy. After this initial forward hop there are two possibilities: (1) The ion may hop back to (A) by overcoming a lower barrier than it experiences in forward hopping, which completes a short range ion motion, or (2) the surrounding ion cloud may relax with respect to site (B) and form a new cage-

effect minimum, as shown in figure 3.15. The cage effect minimum causes a non-zero DC conductivity, given a long enough time for relaxation. Also, this shift contributes to a distribution of relaxation times because the longer the ion stays at site B, the larger the time constant for it to complete a backward hop back to site A.

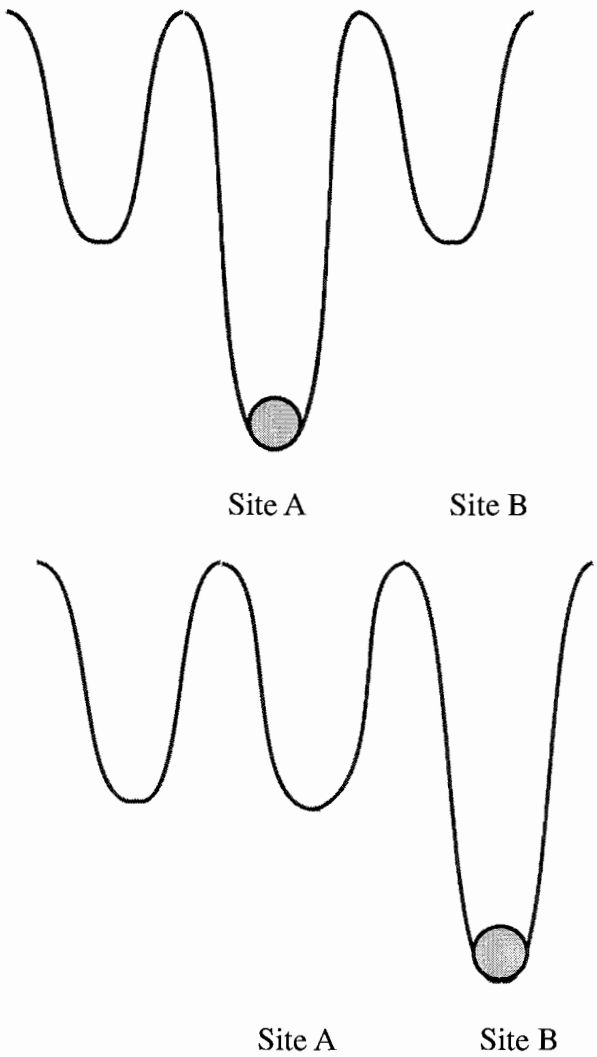

Figure 3.15 The schematic representation of the jump-relaxation process. The relaxation of surroundings after the one step hopping creates a new minimum. Long range motion of particles can be realized by duplicating this process many times along the same direction.

In the Au|P_A|Au system, ion hopping takes place in the intermediate frequency region between that of the electrode polarization and the capacitance charging. For thin samples (<600nm), the latter two processes are very close to each other in term of frequency and leave little room for the ion hopping polarization to be identified. As demonstrated in figure 3.11, those two processes moved towards two ends respectively in thick samples (>600nm), making it possible for the ion hopping polarization to be observed. Figure 3.16 shows the ε' spectra of a 1600nm thick sample. The ion hopping polarization readily shows up as indicated in the figure.

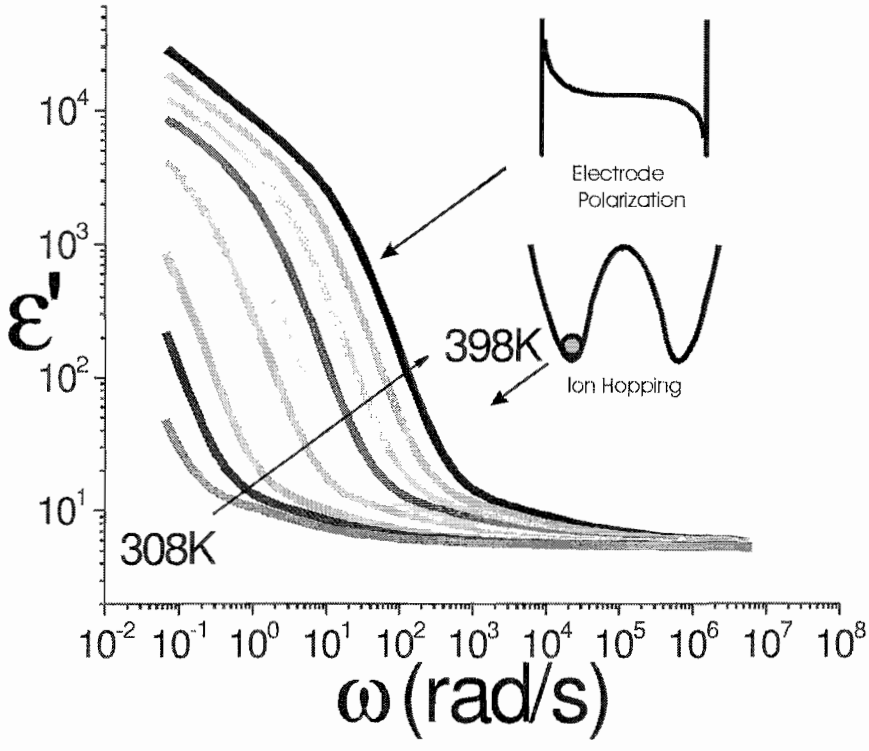

Figure 3.16 Frequency dependent ε' of a 1600nm thick sample at temperatures from 308K to 398 K, stepped by 10 K. The underlying mechanisms of the ion hopping and electrode polarization are described by the inset diagrams.

The Jump relaxation model contends that the DC conductivity and dispersion at higher frequencies are due to the same mechanism: ion hopping. The transition between the two is closely related to the hopping rate of ions in the solid electrolyte. The AC conductivity is usually represented by the Jonscher expression (eq. 3.5). Once the value of the DC conductivity is assigned, the hopping frequency is determined as the frequency in which the AC conductivity doubles relative to the DC conductivity. The results of hopping frequencies determined with this method are shown below in figure 3.17.

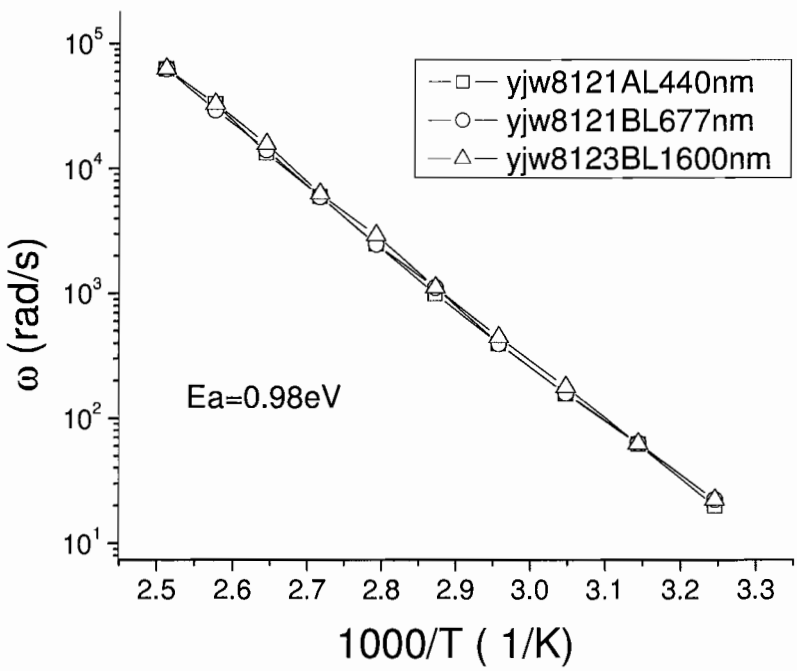

Figure 3.17 The temperature dependence of the hopping frequencies which are determined by assigning the frequencies where the AC conductivity is twice of the DC conductivity. Hopping frequencies of samples with thickness ranging from 440nm to 1600nm are compared. Clearly they overlap very well even the sample thicknesses are very different. Also the hopping frequencies show the Arrhenius type temperature

dependence, from which the activation energy of 0.98eV can be extracted.

It can be seen from this figure that the hopping frequencies of samples with thicknesses ranging from 440nm to 1600nm are almost identical. This is consistent with the fact that the hopping process is intrinsic and should not depend on factors such as the thickness.

3.5 Conclusions

Impedance analysis of Au|P_A|Au sandwich structures reveals multiple relaxation processes in the frequency range from 0.01Hz to 1MHz. Based on the analysis of their temperature and thickness dependence, those dielectric processes were carefully assigned to be the geometric capacitance charging, the ion hopping and the electrode polarization. Also, in the framework of the ion hopping and the electrode polarization, key quantities in Au|P_A|Au such as the activation energy, the effective ion concentration, the ionic DC conductivity, and the ion hopping rates were obtained. The activation energy, which was extracted from the characteristic frequency of the electrode polarization, was 0.98eV. The effective ion concentration is on the order of 10^{20} and showed a modest temperature dependence. The ionic DC conductivity strongly depends on the temperature and ranges from 10^{-10} to 10^{-7} S/cm from 308K to 398K. The ion hopping frequency spans a wide range from 10Hz to 4000Hz with temperatures between 308K and 398K.

CHAPTER IV

IMPEDANCE ANALYSIS OF ELECTRONIC CARRIERS IN AN ANIONICALLY FUNCTIONALIZED POLYACETYLENE BETWEEN METAL ELECTRODES

4.1 Overview

There are possibly five species that participate in the relaxation process in the anionically functionalized polyacetylene (P_A) shown in figure 3.1, including neutral molecules, anions, cations, electrons and holes. In general, electronic carriers respond to electrical stimulus much faster than ionic carriers. In the mixed ionic-electronic conductor P_A , both ionic and electronic carriers can in principle contribute to conduction making it very challenging to unequivocally assign relaxation processes to certain species. In chapter III, the relaxation peak seen in the angular frequency range of 1 - 100 rad/s at temperatures from 308K-398K is attributed to ion conduction, more or less by experience and qualitative observations. Since electronic carriers are expected to respond faster than their ionic counterparts, it is possible to distinguish ionic from electronic carriers based on their activation energy. The assignments of the dielectric relaxations measured in chapter III to ionic processes assume that there is a negligible intrinsic density of electronic carriers. This assumption can be checked by intentionally injecting electronic charges into the system through an applied bias (V_{app}) and then comparing the resulting dielectric response and in particular its temperature dependence to the measurements in chapter III where $V_{app} = 0$. If the assignments are correct, it is expected that lowering the temperature below room temperature will cause the processes observed at $V_{app}=0$ to shift out of the experimental frequency range and new processes

corresponding to the injected electrons will shift in. In this chapter, such low temperature measurements with V_{app} nonzero are reported. These measurements help confirm the assignments made in chapter III and provide information on the transport and polarization process of electronic carriers. It is noteworthy that unlike in more conventional semiconductors, injected electronic carriers remain in the system at sufficiently low temperature because they are compensated by ions to maintain charge neutrality. Those ions are immobile at low temperatures and cannot relax back to equilibrium. In this sense the injected electronic carriers are trapped in the system at low temperature.

The set of experiments described herein was inspired by previous work done on frozen PIN junctions and junction formation by capacitance spectroscopy in polymer light-emitting electrochemical cells (PLECs)[1,2,3]. The results from these experiments can offer important information regarding charge injection and operation mechanisms of PLECs.

4.2 Experimental procedures

Samples were fabricated and annealed using the same procedures described in chapter III (section 3.1). Additional carriers were injected into the polymer by applying a V_{app} for a certain period of time at 328K. This charge injection was accomplished while the sample was stored under active vacuum. The sample was then kept under V_{app}, and cooled down to 173K at an average rate of 8c/min with liquid nitrogen. The impedance measurement was carried out in the temperature range of 173K to 263K with a step of 10 degrees. At each temperature, the frequency was swept from 1M rad/s to 1 rad/s.

Impedance spectroscopy experiments were also conducted by applying both a DC voltage (V_{DC}) and a small amplitude AC voltage on the sample, while the temperature was held constant. These experiments were performed after electronic carriers had been introduced with V_{app} at room temperature and then cooling samples down while holding them at V_{app}. Both forward and reverse V_{DC} (polarity relative to V_{app}) were applied to the sample during the impedance spectroscopy measurement.

4.3 Experimental results

4.3.1 Small amplitude AC impedance

Figure.4.1 shows the ε' spectra at temperatures from 173K to 233K for V_{app}=1.7V. Some similarities in term of shapes were observed between ε' spectra in the temperature range of 308K to 398K for $V_{app}=0$ (Chapter III) and that in the temperature range 173K to 233K for $V_{app}=1.7V$ (figure 4.1). In both cases, there are three dispersions in the ε' spectra, with the one in the high frequency region independent of temperature while that in the intermediate frequency region highly sensitive to temperature. The similarities are sufficiently strong to justify assigning the features in the ε' spectrum for V_{app} = 1.7V (figure 4.1) in the same way as with V_{app}=0 (Chapter III), but for electronic rather than ionic charge carriers. Therefore, the three dielectric relaxation processes at low temperatures are assigned to: geometric capacitance charging, electronic carrier transport, and the polarization of electrons against the electrodes. Further support for these assignments will be provided in the discussion section.

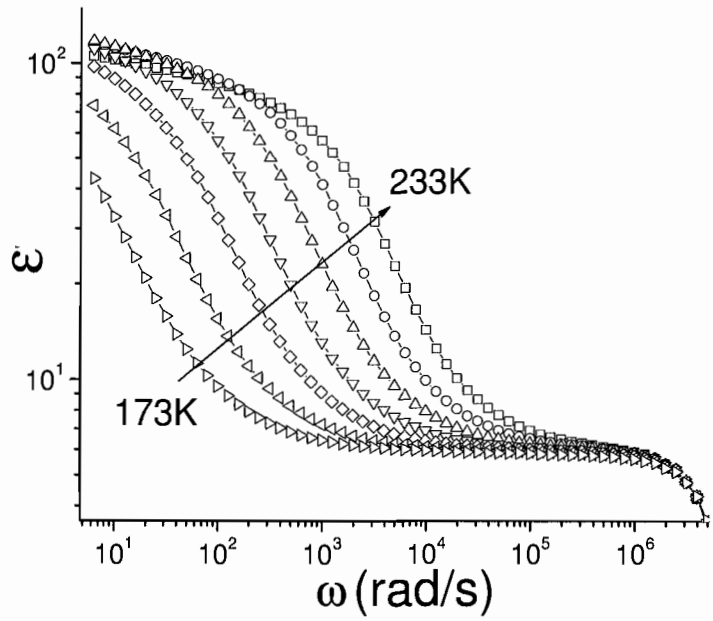

Figure 4.1 Frequency dependent ε' in the temperature range from 173K to 233K. The value of V_{app}=1.7V, and the film is 200nm in thickness.

Despite the overall similarity between the ε' spectra for V_{app} = 1.7V between T= 173K to 223K and that for V_{app} =0 between T= 308K to 398K, some differences were observed between them, especially in the low frequency region. The imaginary part of the complex permittivity (ε'') for V_{app} = 1.7V in the low temperature region (173K to 233K) shows a clear peak, as illustrated in figure 4.2. Correspondingly, in figure 4.3, the AC conductivity (σ) for V_{app}=1.7V (173K to 233K) continuously decreases as the frequency is lowered, which is in clear contrast to the plateau that often appears in σ at low frequencies for V_{app} =0 (328K to 398K). The implications of these observations will be examined in the discussion section.

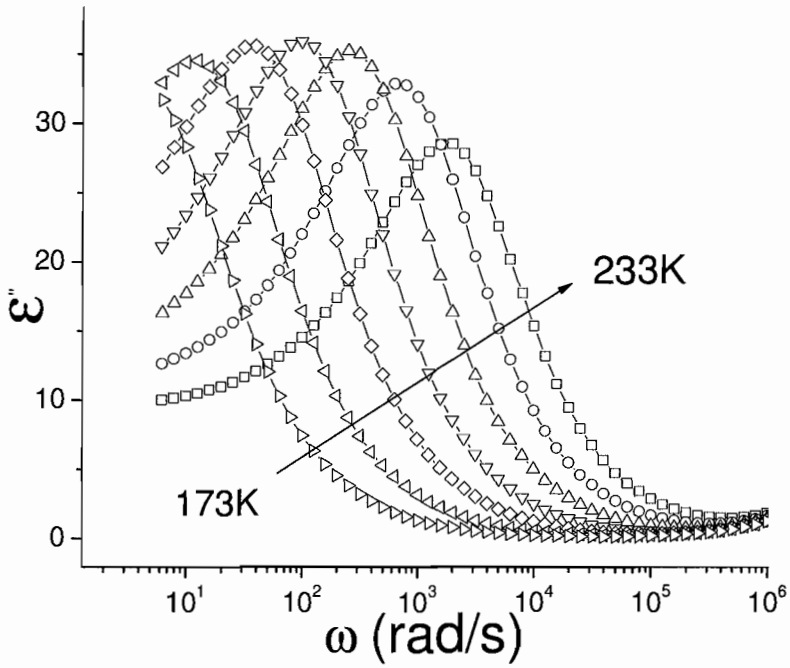

Figure 4.2 Frequency dependent ε'' in the temperature range from 173K to 233K. The value of V_{app} is 1.7V and sample thickness is 200nm. For both figures 4.1 and 4.2, the characteristic frequencies are from 1 rad/s to about 300 rad/s, which is higher than those observed in the temperature range from 308K to 398K.

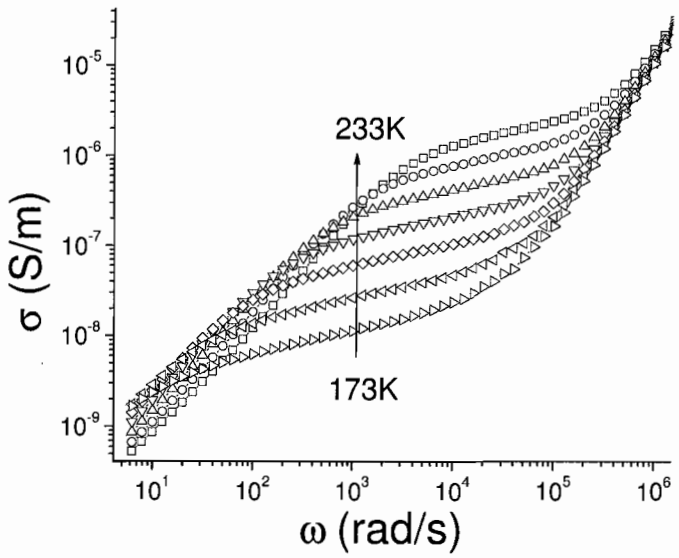

Figure 4.3 Frequency dependent σ in the temperature range from 153K to 233K, with a step size of 10 degrees as a function of angular frequency. The value of V_{app} is 1.7V and the sample thickness is 200nm.

The loss tangent measured for the Au|P_A|Au sample with V_{app}=1.7V at temperatures spanning from 173K to 223K is shown in figure 4.4. As can be seen, there is a well-defined peak in the loss tangent, and there is no dispersion in the low frequency region.

Using the same technique described in section 3.2.2 in chapter III, two sets of frequencies related to electrode polarization can be extracted from either the peak in the imaginary part of the complex permittivity in figure 4.2 (ω_{EL}) or the peak of the loss tangent (ω_{LT}). As shown in figure 4.5, their temperature dependence follows an Arrhenius relationship with an activation energy of 0.34eV.

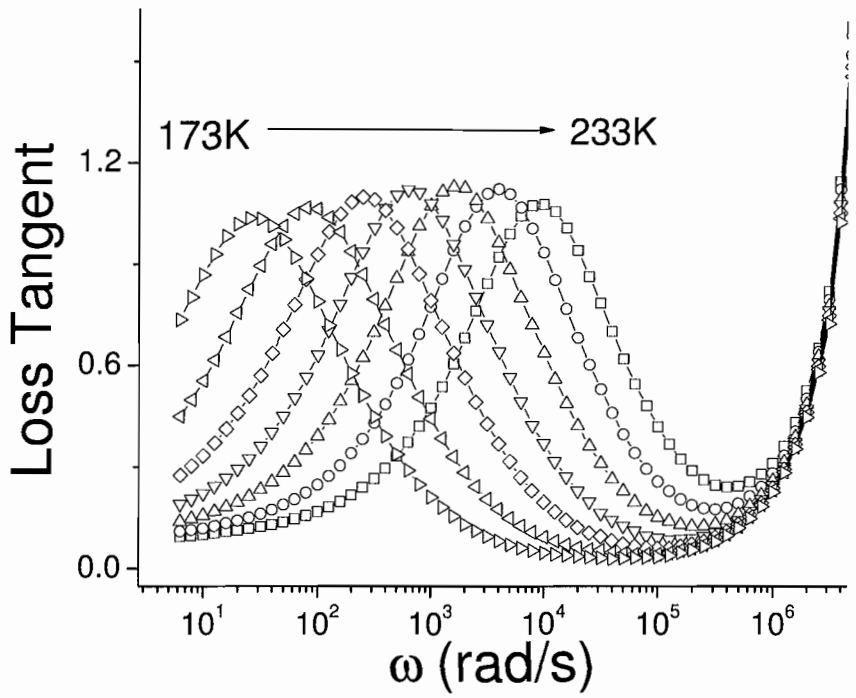

Figure 4.4 Frequency dependence of the loss tangent in the temperature range from 173K to 233K. The value of V_{app} is 1.7V, and the sample thickness is 200nm. In contrast to the higher temperature (308K to 398K) data, well defined peaks are observed in the loss tangent at these temperatures.

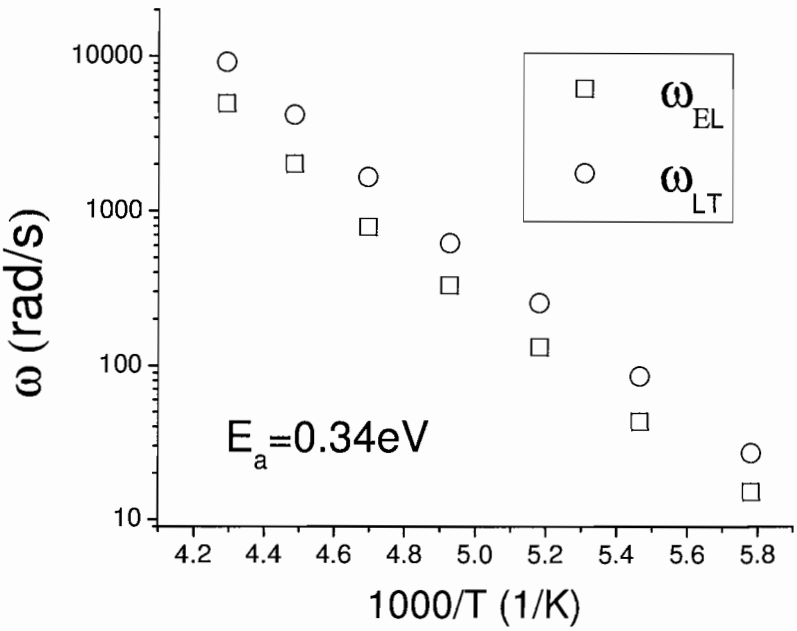

Figure 4.5 Frequencies related to the electrode polarization ω_{EL} (□) and ω_{LT} (○). Both show Arrhenius-type behavior with an activation energy of 0.34eV.

Further investigations into the dielectric response in the low frequency region were carried out by the adjusting V_{app} used to introduce the electronic carriers. This set of experiments was done by first introducing electronic carriers into P_A by applying a DC voltage of either 1.5V, 1.7V or 2V for 20 minutes at room temperature and then cooling the sample down to 173K for impedance measurements. The V_{app} was held constant during the cooling and turned off right before the start of the impedance measurement at 173K.

A difference in the peak position in the loss tangent can also be noted in figure 4.6. Apparently, increasing the V_{app} shifts the characteristic frequency towards higher values.

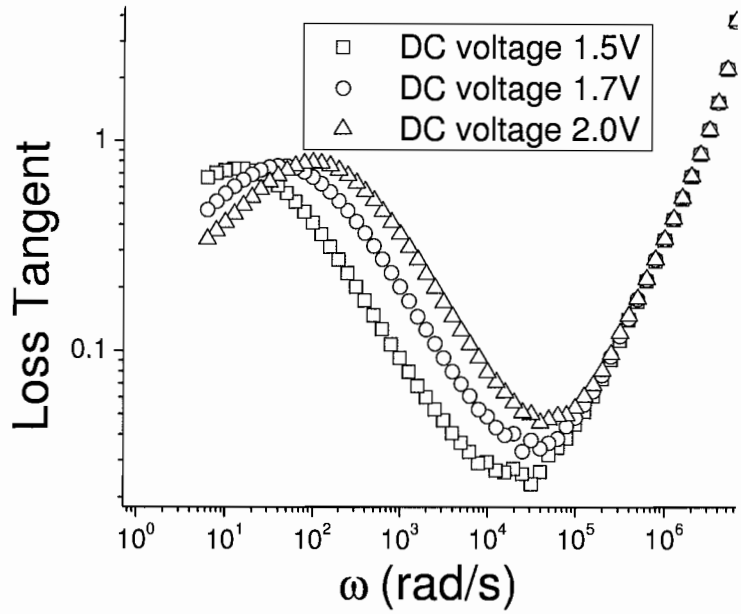

Figure 4.6 The DC voltage (V_{app}) dependence of the loss tangent at 173K as a function of frequency for V_{app}=1.5(□), 1.7(○), and 2.0 V (Δ).

Figure.4.7 shows the AC capacitance with V_{app} of 1.5V, 1.7V, 2.0V. The double layer capacitance at each V_{app}, which corresponds to the capacitance at ω_{LT} as defined by loss tangent peaks in figure 4.6, is labeled by a cross in figure 4.7 and shown to be the same for V_{app} at 1.5V,1.7V, and 2.0V. At the same time, the AC conductivity between 60 rad/s and 6000 rad/s also increases substantially, as showed in figure 4.8.

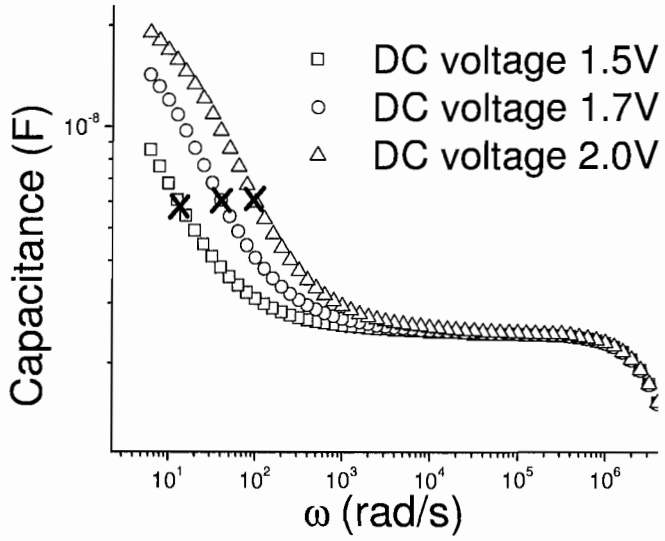

Figure 4.7 Frequency dependent capacitance as a function of DC voltage (V_{app}) at 173K. Cross indicates capacitance at ω_{LT} for each V_{app}, and the legend indicates the V_{app} used to introduce electronic carriers into the device at room temperature.

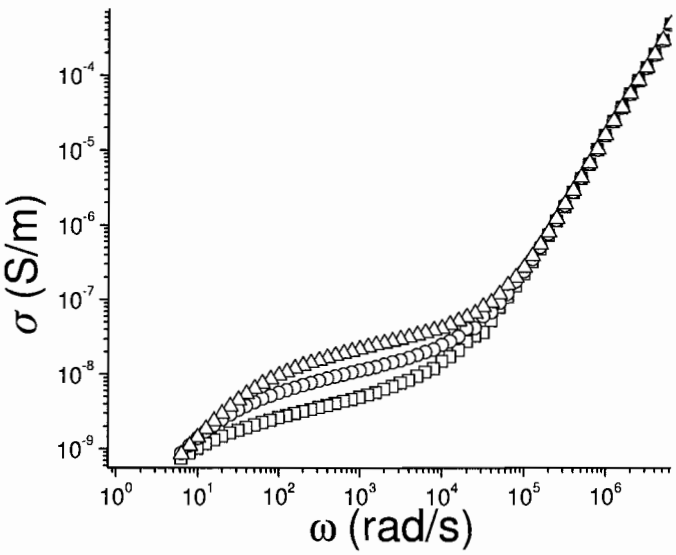

Figure 4.8 Frequency dependent σ at 173K for charging under V_{app}=1.5V(□), 1.7V (○), and 2V (Δ) respectively at 308K

4.3.2 Influence of V_{DC}

In order to manipulate the behavior of the injected electronic carriers, a DC voltage (V_{DC}) was applied along with a small amplitude AC signal to samples into which electronic carriers had been injected with V_{app} and the temperature lowered to freeze ionic carriers. As we can see in figure 4.9, which shows the AC conductivity at various V_{DC}, the influence of V_{DC} on the impedance-related functions can mostly be found in the low frequency region. In the intermediate and high frequency regions, the results are largely the same. The low frequency conductivity increases when the applied V_{DC} is higher.

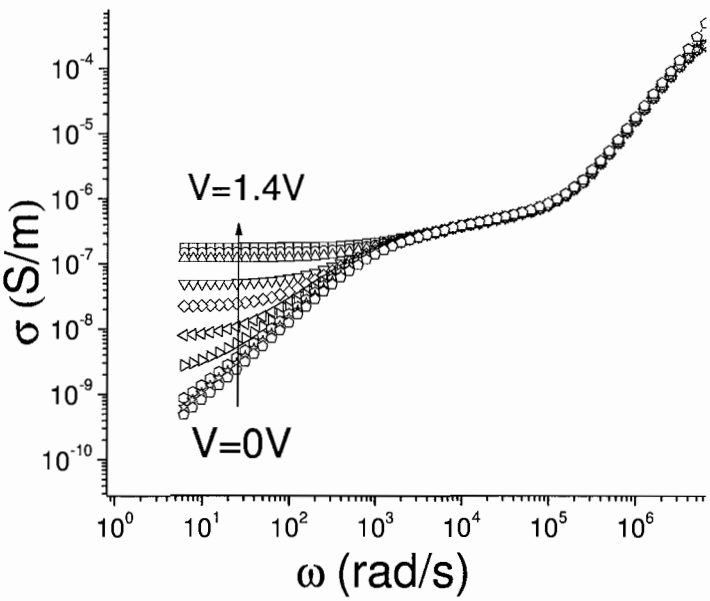

Figure 4.9 Frequency dependent σ under V_{DC} from 0V to 1.4V at 203K. The difference in the conductivity lies mostly in the low frequency region from 1 rad/s to about 100 rad/s. In general, the low frequency conductivity increases along with increasing values of V_{DC}.

The overall effect of the DC voltage on the derivative of ε' is showed in figure 4.10. The inset in this figure illustrates the V_{DC} dependence of ω_{EL}, which first decreases with increasing V_{DC} and then increases after peaking at about 0.7V.

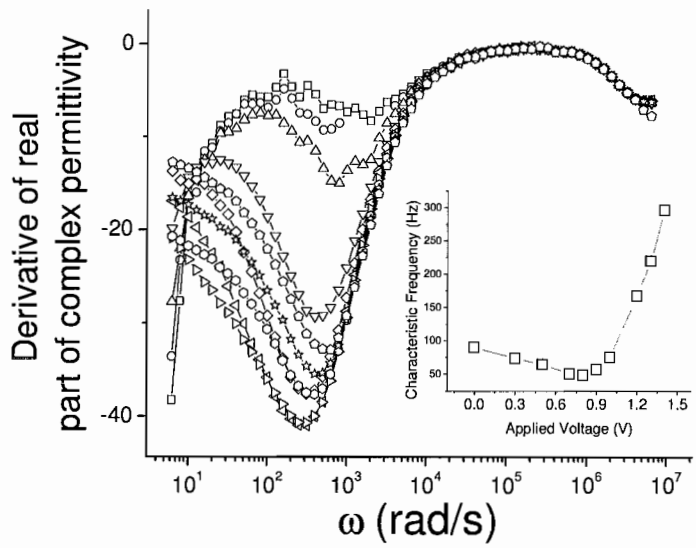

Figure 4.10 Derivatives of the ε' spectra at 203K. The inset illustrates the V_{DC} dependence of the characteristic frequency ω_{EL}.

The V_{DC} also affects the behavior of the capacitance. As shown in Figure 4.11, the capacitance in the low frequency range exhibits a considerable spread with V_{DC} ranging from 0V to 1.5V. It is interesting to note that when comparing the capacitance at the same frequency at various V_{DC}, the value of the capacitance first increases, then peaks at about 0.7V, and finally decreases.

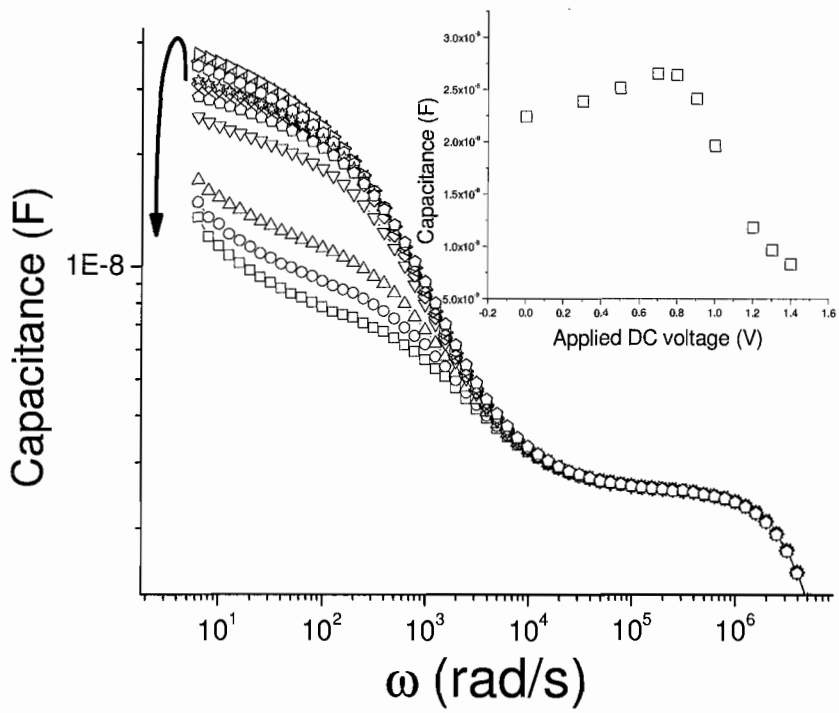

Figure 4.11 The frequency dependence of the capacitance under V_{DC} from 0V to 1.4V at 203K. The arrow indicates how the capacitance changes while the V_{DC} increased from 0V to 1.4V. The inset illustrates V_{DC} dependence of the capacitance at 60 rad/s.

Small amplitude AC impedance was also carried out while the sample was under reverse bias. As with the forward V_{DC}, there is not much difference in the impedance related functions in the intermediate and high frequency, as showed in figure 4.12. However, the reverse V_{DC} shows very little effect in the low frequency region. This is clearly in contrast to the forward bias case.

The reverse V_{DC} dependence of the capacitance at the same frequency exhibits less change when compared with that in the forward V_{DC} case. The overall effects of V_{DC} on capacitance including both forward and reverse V_{DC} are shown below in figure 4.13.

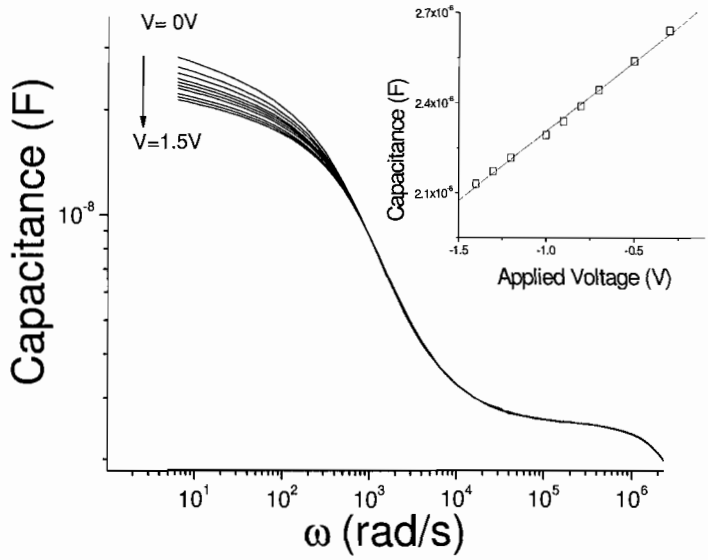

Figure 4.12 Frequency dependent capacitance as a function of reverse DC voltage (V_{DC}) at 203K. The inset shows the capacitance at 6 rad/s as function of reverse V_{DC}.

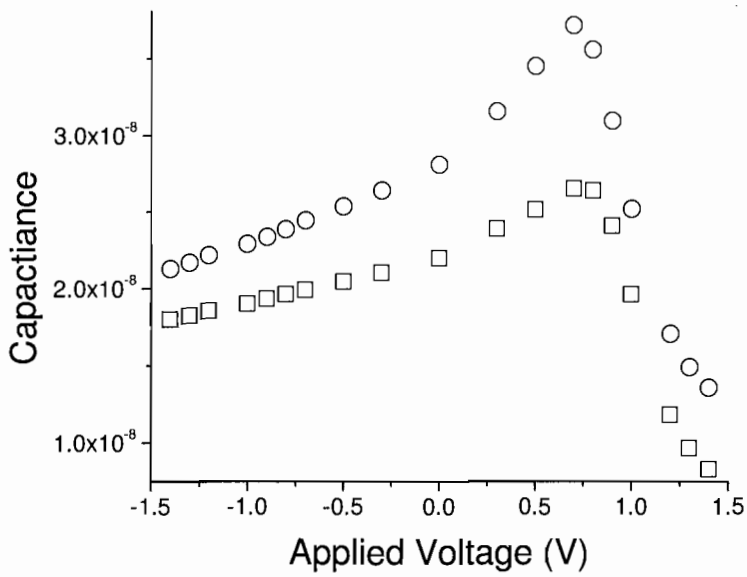

Figure 4.13 Capacitance as a function of V_{DC}, showing both reverse and forward bias. Capacitances at two frequencies, 60 rad/s (□) and 6 rad/s (○), are selected to demonstrate the effects of V_{DC} on them. Apparently forward V_{DC} exerts much more influence on capacitance than the reverse V_{DC}.

4.4 Discussion

Due to the immobility of the ions at the temperature employed, the P_A between metal electrodes described in this chapter behaves in a manner similar to traditional ion-free organic semiconductors and the response to electrical stimulus is solely due to the presence of mobile electronic carriers [4,5,6]. In general, the transport of electronic carriers in conducting polymers is a combination of both band-like conduction within the polymer chain and inter-chain hopping. From impedance measurements at temperatures ranging from 173K to 233K, ω_{EI} and ω_{LT} were determined. It was shown that both the conductivity and the characteristic frequencies of the thermally activated hopping process follow Arrhenius-type behavior, with an activation energy of 0.34eV.

4.4.1 Impedance-related functions

As mentioned in the section 4.3, three dielectric processes are seen by impedance measurement at low temperatures. They are the geometric capacitance charging, active carrier transport, and electrode polarization. The nearly frozen ionic carriers could not be responsible for these processes considering that the ω_{EL} in the low temperature range (173K to 233K) studied in this chapter are higher than those at higher temperatures (308K to 398K) with V_{app}=0. The only charge carriers that can then exhibit the dielectric relaxation in the low temperature, $V_{app} \neq 0$ experiments are the electronic carriers that were injected at the 328K under V_{app}. Therefore, the frequency dependence of the impedance-related functions at reduced temperature is due to the dielectric relaxation processes of the electronic carriers. In conjugated polymers, the electronic conduction is

limited by the inter-chain charge transport, which is a hopping process. Therefore instead of ion hopping, we are probing the electronic carrier hopping at temperatures from 173K to 233K.

As we can see from loss tangent and ε'' spectra, well defined peaks were observed at temperatures from 173K to 233K. The low frequency relaxation that was observed in the V_{app}=0 experiments at higher temperatures was not observed in the low temperature $V_{app} \neq 0$. In addition, the σ decreases continuously at low frequencies after electrode polarization. In contrast, the σ observed for the V_{app}=0, higher temperature experiments was observed to plateau at low frequency, which was attributed to the electrode being non-blocking to electronic carriers. The steady decrease in the σ with decreasing frequency for the $V_{app} \neq 0$ experiments implies the electrode is substantially more blocking at the lower temperatures.

4.4.2 Characteristic frequency of the electrode polarization

As we noticed in figure 4.7, ω_{LT} increases with higher V_{app}. In a simplified equivalent circuit, the characteristic frequency of the RC circuit is determined by the capacitance and resistance. In this specific situation, the capacitive component is the double layer capacitance, and the relevant resistor is the bulk resistance of electronic carriers. The increase in the ω_{LT} results from the fact that the double layer capacitance remains the same(figure 4.7), while the conductivity of electronic carriers increases by 9 fold (figure 4.8) when the V_{DC} is increased from 1.5V to 2V. This equivalent circuit analysis confirms

the assignment of the low frequency dielectric response to electrode polarization, in a similar way as demonstrated in chapter III.

The characteristic frequencies were determined to be between 100 rad/s to 10k rad/s, which is much higher than those determined from impedance measurements at temperatures higher than 308K. This clearly rules out the possibility that the dielectric relaxations detected at T = 308K and at higher temperatures are due to electronic carriers, indicating that P_A does indeed have a very small intrinsic carrier density. Furthermore, the activation energy of electronic carrier hopping is about 0.34eV, which is much lower than that measured for ion hopping. This is reasonable, because the size of the ions is much larger than that of the electronic carriers. Therefore, it takes much more thermal energy to mobilize ions to neighboring sites.

4.4.3 Effects of V_{DC}

As showed in figure 4.9, even though the conductivity at low frequency and with V_{DC} =1.4V is approximately three orders of magnitude higher than that with V_{DC}=0V, the conductivity in the intermediate frequency region remains almost unaffected. The conductivity at low frequency is closely related to the interfacial processes, while that in the intermediate region results from the electronic carrier hopping process. The main factors determining the rate of hopping transport are the carrier concentration and mobility. The constant hopping conductivity in the intermediate region demonstrates that the electronic carrier concentration and mobility are unchanged even with the dramatic

enhancement of charge injection across the interface. These results suggest a scenario that all the charges present detected by impedance spectroscopy were injected by holding V_{app} at 328K. After the cooling, all the charges injected at one electrode by the V_{DC} are transported and collected at another electrode and where the device is under both a dynamic equilibrium and a steady state. In addition, using this scenario, one would also expect the characteristic frequency to be determined solely by the double layer capacitance, given the fact that the bulk resistance does not show any V_{DC} dependence. To see this connection, the inverse of the capacitance is plotted together with the characteristic frequency. In general, they follow a very similar trend with a decrease, followed by a minimum at about 0.7V, and then a sharp increase as the V_{DC} is increased from 0V to 1.4V as shown below in figure 4.14.

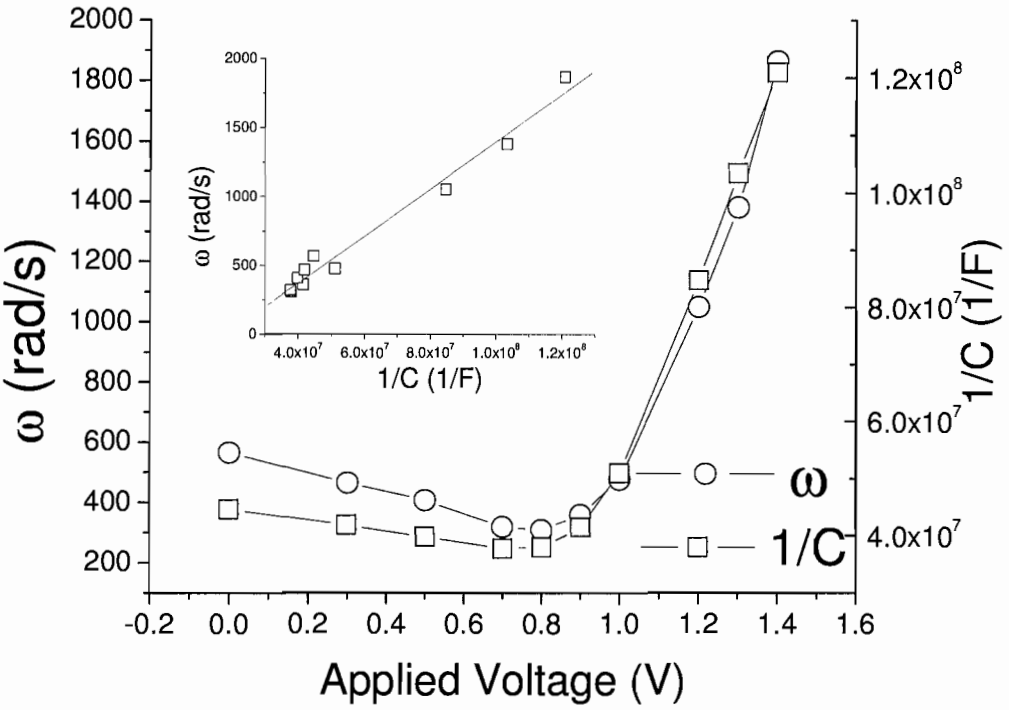

Figure 4.14 Frequency as a function of V_{DC}, illustrating the relationship between the double layer capacitance and the characteristic frequency at 203K. The frequency is also plotted versus the inverse of the capacitance in the inset.

The influence of V_{DC} on the AC conductivity at low frequencies clearly demonstrates that the electrode transparency can be tuned from blocking (high ρ, non-Faradic) to non-blocking (ρ=0, Faradic) with the application of V_{DC}. The effects of discharging have been discussed in details in chapter II 2.3.3. Extensive studies on this subject were carried by J.R.Macdonald [7,8,9] .

The dependence of the capacitance on the V_{DC} applied during the impedance measurement is due to the change of electrode transparency, as described in eq 2.26. In the voltage range from 0V to 0.7V, the capacitance increases because of a stronger

polarization under the increased field. When the voltage reaches a high enough value, charge injection occurs. The charge transport across the interface decreases the concentration of the space charge at the interface, which therefore reduces the double layer capacitance.

The frozen ions are equivalent to the dopants in traditional semiconductor junctions. Therefore the frozen P_A between two metal electrode acts like a semiconductor junction, with built-in field formed with ions redistributed at 328K with V_{app} and then frozen at 173K. The ionic carriers still play a role in electronic carrier transport across the interface by way of built-in potential, as illustrated by the very different behaviors of the capacitance under forward and reverse V_{DC}[10,11,12].

4.5 Conclusion

In addition to studies on the dynamics of the ionic carriers at temperatures from 308K to 398K in chapter III, complementary impedance analysis on electronic carriers (extrinsic) were carried out in order to further confirm the assignment of the relaxation processes discussed in chapter III and to investigate the electrical properties of frozen devices. The electronic carriers introduced externally were probed by a small amplitude AC signal, with or without the application of V_{DC} at temperatures from 153K to 233K, in which the ionic carriers are believed to be immobile. The characteristic frequencies of electronic carrier relaxation are between 100 rad/s and 10K rad/s with temperatures ranging from 173K to 233K. Also, ω_{LT} vs 1/T shows Arrhenius-type behavior, with an activation energy of about 0.34eV. Impedance analysis with V_{DC} up to 1.5V at 203K show that the low frequency (<1200 rad/s) conductivity increases as the V_{DC} increases,

while that at higher frequencies remain unaffected. V_{DC} applied during the impedance measurement affects the electrode kinetics as shown in the variation in the low frequency conductivity. At the same time, the conductivity related to the hopping transport of electronic carriers does not change with V_{DC} because the electronic concentration is not affected. In addition, the capacitance at 6 rad/s and 60 rad/s increase first with forward V_{DC}, peaks at about 0.7V, and is then seen to decrease.

However, with reverse V_{DC}, the capacitance is only seen decreasing gradually with increasing V_{DC}, although not as much change is seen as in the forward bias case. The electrode transparency, which is affected by the V_{DC} is the key to understanding these behaviors. At low temperatures (<233K) and low voltages (<0.7V), the electrodes are blocking to the electronic carriers. Either higher temperature (>233K) or higher V_{DC} (>0.7V) varies the electrode transparency from blocking to non-blocking. Under the high V_{DC} (>0.7V), electronic carriers can be injected as evidenced by the enhanced AC conductivity at low frequencies (<1200 rad/s). So the description of the system switches from one characterized by blocking electrodes when the V_{DC} is low (<0.7V) to one where the electrodes are non-blocking at higher voltages.

The measured activation energy for electronic carriers confirms that the relaxations observed at temperatures from 308K to 398K are related to the ionic carriers.

CHAPTER V

IMPEDANCE ANALYSIS OF AN ANIONICALLY FUNCTIONALIZED POLYACETYLENE UNDER DC VOLTAGE BETWEEN METAL ELECTRODES

5.1 Overview

Advances in electronic instrumentation have allowed impedance spectroscopy to become a powerful tool for studying both the relaxation processes and the operational mechanisms of organic and inorganic devices [1,2,3]. There have been many studies in which impedance spectroscopy was utilized to investigate charge injection and transport, the role of an interfacial layer, and the effects of trapping states in semiconductor devices containing a conducting polymer as the active layer [4,5,6].

It is generally agreed that ions in polymer light-emitting electrochemical cells (PLECs) are instrumental in enhancing electronic charge injection and lowering the threshold voltage. However, the exact nature of this process is still somewhat vague [7]. To better understand the role of ionic carriers in electronic charge transport, the knowledge of ion dynamics during substantial charge injection is necessary. Studies in chapter III focused on near-equilibrium investigations of the electrical properties of an anionically functionalized polyacetylene sandwiched between two gold electrodes (Au|P_A|Au). The studies described in Chapter III utilized a small amplitude AC stimulus so not to perturb the system significantly. While it is very important to understand the near-equilibrium properties of the Au|P_A|Au structure, there are possibly many interesting phenomena, such as electrochemical doping and junction formation that can occur when the system is driven away from equilibrium by a DC bias (V_{DC}). The non-equilibrium

status of the system can then be probed by a small amplitude AC signal in order to extract information. This type of measurement, namely the AC impedance with V_{DC}, has been used extensively in measuring semiconductor interfaces [8,9], and it has proven to be powerful in studying the operational mechanisms of polymer electrochemical cells [10,11]. In the context of this chapter, AC impedance with V_{DC} is used to simultaneously to measure electronic charge transport and ion dynamics properties. In this aspect the work in this chapter connects to that in chapter III, which reported studies on ion dynamics, and that in chapter VI, which focuses on the electrical measurements in the time domain.

5.2 Experimental procedures

The anionically functionalized polyacetylene (P_A) was synthesized by using of ring-opening metathesis polymerization of an anionically functionalized cyclooctatetraene (COT) as the monomer. The polymer was subsequently dissolved in methanol that had been distilled from (Mg,CaH_2). Spin-coating was used to deposit a thin film in a controlled way onto a glass slide, as described in more detail in Chapter III, section 3.2.

Impedance analysis was carried out using a Solatron 1260 impedance analyzer coupled with a Solatron 1294 dielectric interface. This set-up can potentially measure impedance as high as 1 Tohm. The sample was stored in a stainless steel canister which then is set up in a Sun environmental chamber temperature control. Impedance spectroscopy was conducted using 10 degrees step from 308K to 398K. At each temperature, the sample was swept in the frequency range from 1MHz to 0.01Hz.

The dielectric functions were then calculated from the impedance.

For reliable impedance measurements, the device under test has to be in a steady state, because transient components in response to DC stimuli introduce error in the impedance measurement results. It was determined that for the time domain electrical measurement (in chapter VI), the sample needed 4 hours to reach steady state. Therefore, the DC voltage (V_{DC}) was held steady for 4 hours before the AC signal was applied for the impedance measurement.

Current response in the time domain was measured with a Keithley 236 source measure unit and data was collected with a custom Labview program. The sample under investigation was sealed in the stainless steel canister and kept under vacuum during the measurement. Temperature was controlled by a Sun system EC10 environment chamber. The V_{DC} was applied for 4 hours to bring the sample to steady state, followed by a small amplitude voltage oscillation of magnitude 10mV. The sampling rate for these current measurements was 10pt/s.

5.3 Experimental results

AC impedance with $V_{DC} = 0$ of P_A between two electrodes were understood within the frame of electrode polarization and the ion hopping mechanism that can be found in chapter 3, section 3.3. Based on those experiments and analysis, the effects of V_{DC} in addition to the small amplitude AC signal are studied. The capacitance spectra under V_{DC} at temperatures 308K, 328K and 348K are showed in figure 5.1. The effect of V_{DC} on capacitance is small until 0.5V or higher. For T = 328K and 348K and in the low

frequency region, the capacitance decreases considerably for V_{DC} = 0.5V when compared with those at lower V_{DC}. The decrease becomes even more dramatic at T = 308K, when the dielectric constant turns to negative at low frequency.

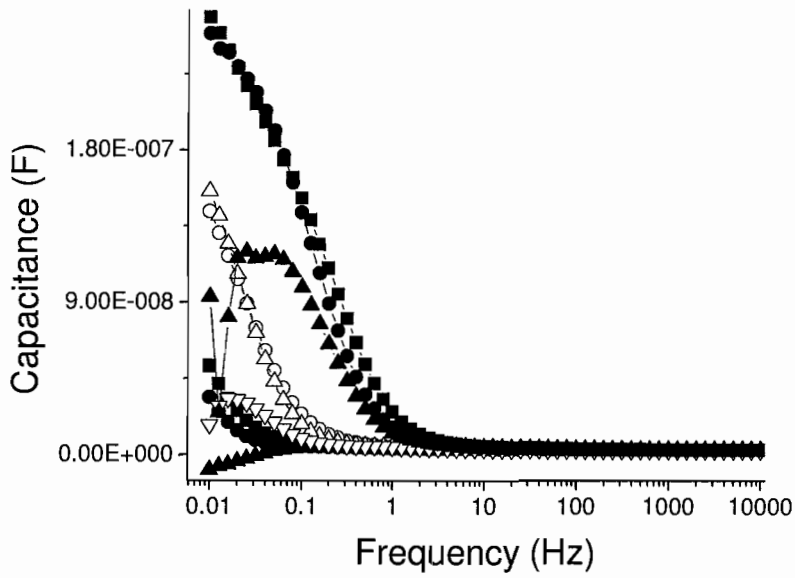

Figure 5.1 Frequency dependent capacitance under various V_{DC} for three temperatures: T = 308K (solid symbols), 328K (empty symbols), and 348K(solid symbols with lines). For each temperature, tests are done at the following V_{DC} 0V (squares), 0.3V (circles) and 0.5V (triangles).

Impedance measurement with $V_{DC}=0$ in chapter III demonstrates scaling properties in impedance-related functions at temperatures from 308K to 398K. As demonstrated in figure 5.2, the ε' spectra at 308K,328K and 348K converges into one curve after normalizing with the characteristic frequency from the loss tangent (ω_{LT}) at each temperature. However, as shown in figure 5.3, there are significant deviations from the scaling properties in the low frequency region when the V_{DC} is non-zero, and peaks

appear at different frequencies for T = 308K, 328K, and 348K. For frequencies higher than 1Hz, the scaling properties still hold. At this point, we can see that the deviations from scaling properties and the appearance of negative capacitance for T = 308K at low frequency cannot be attributed solely to the rate of the relaxation process.

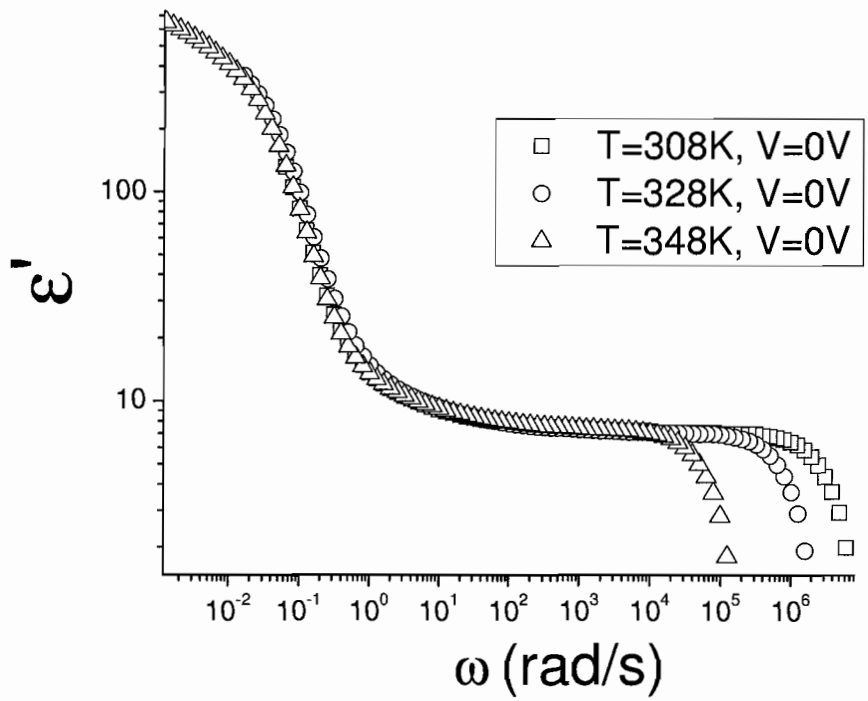

Figure 5.2 Frequency dependent ε' at T = 308K, 328K, and 348K after the frequency is normalized with ω_{LT} at each temperature .The V_{DC} is zero for all three temperatures.

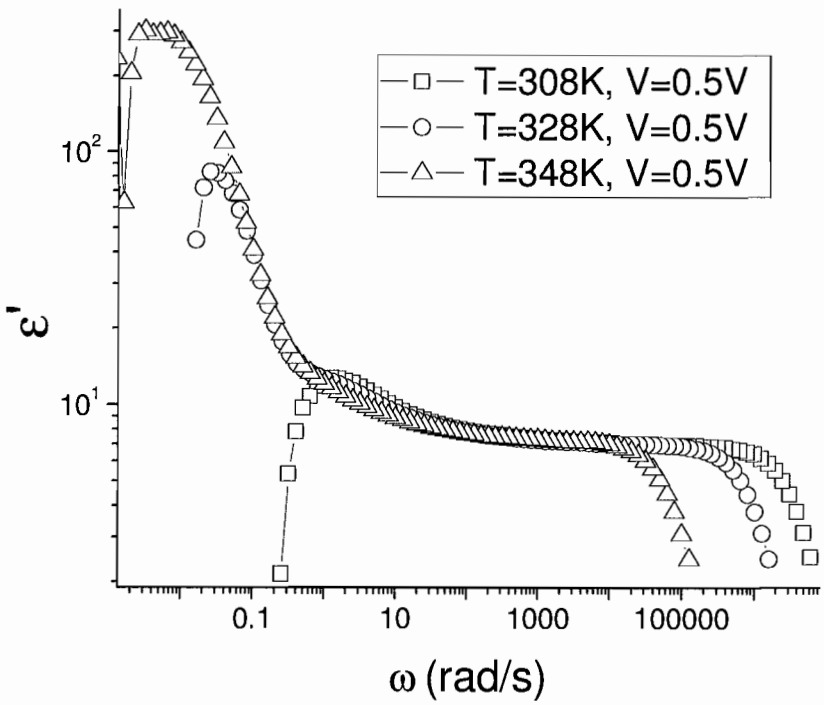

Figure 5.3 Frequency dependent ε' at T = 308K, 328K, and 348K after normalization with ω_{LT}.

Impedance analysis was also carried out where the applied voltage was higher than 0.5V, and the absolute value of the real part of the permittivity is shown in figure 5.4. As described above, the real part of the permittivity starts to become negative at low frequency when the V_{DC} is 0.5V or greater. Also, an enhancement of the capacitance is observed at intermediate frequencies (0.1Hz to 1000Hz).

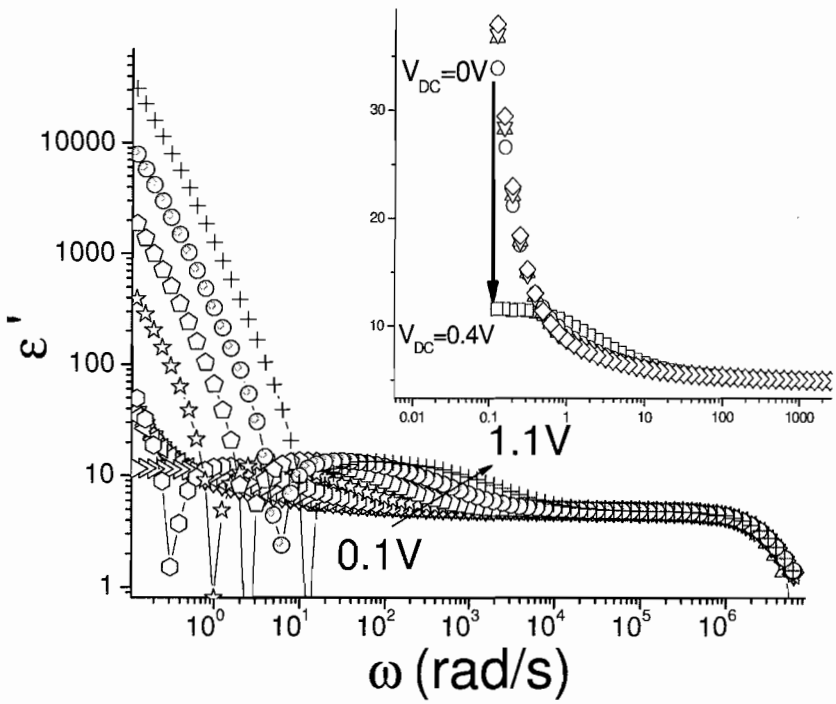

Figure 5.4 Frequency dependent ε' at T = 308K with applied V_{DC} from 0V to 0.9V. The inset expands the low frequency region with V_{DC} from 0V to 0.4V to demonstrate the decrease of ε'

Correspondingly, the σ is affected dramatically also by the V_{DC}, especially when V_{DC} is higher than 0.5V, as shown in figure.5.5. The σ in the low frequency regime (around 0.1 Hz) increased by 3 orders of magnitudes at V_{DC}=0.9V when compared with that at V_{DC} = 0V. The conductivity in the intermediate frequency region (from 10Hz to 1KHz) is also enhanced by the V_{DC}, although not as much as that at the lower frequencies.

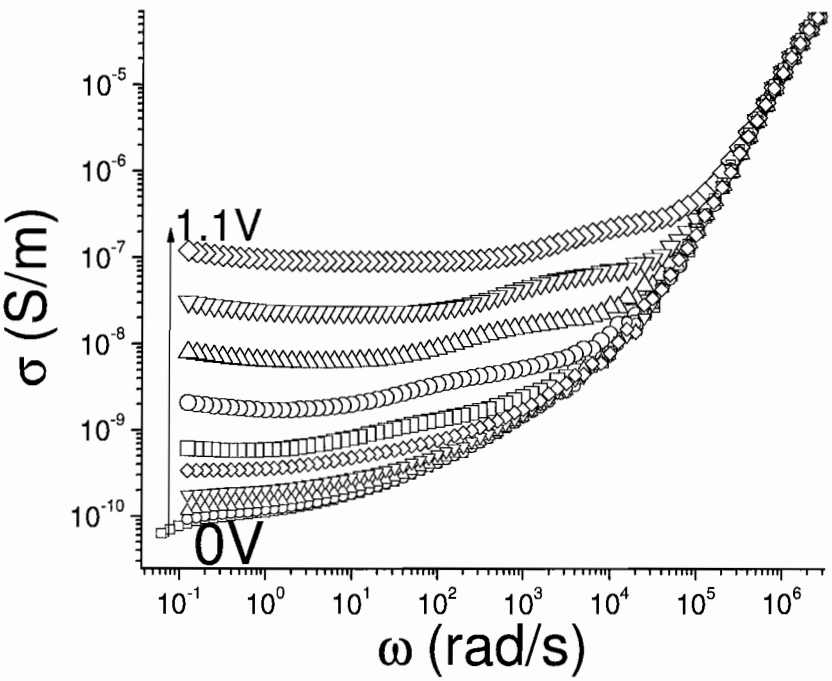

Figure 5.5 Frequency dependent σ at T = 308K with V_{DC} from 0V to 1.1V.

The influence of V_{DC} on capacitance is present only in the low frequency region, as shown in figure 5.6. In addition, there is little difference between the capacitance at 0V up to 0.3V. When the V_{DC} becomes greater than 0.3V, the low frequency capacitance starts to decrease. The V_{DC} dependence of the capacitance is illustrated by selecting a representative low frequency (25mHz), as shown in figure 5.7. The capacitance increases by a modest amount as the V_{DC} increases from 0V to 0.3V. In contrast, the capacitance starts to decrease greatly when the V_{DC} is higher, and finally becomes negative at 0.5V.

The influence of both V_{DC} and charge injection can be seen more clearly from the frequency dependence of the conductivity. Not surprisingly, the conductivity in the low frequency region increases when the applied V_{DC} is increased from 0V to 0.5V as showed in figure 5.8.

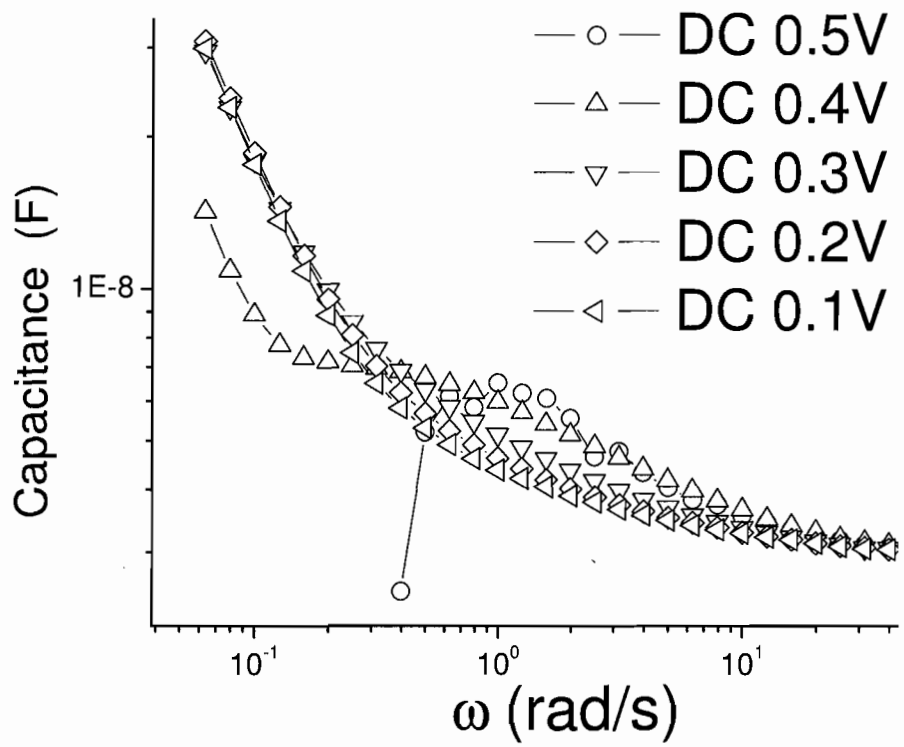

Figure 5.6 Frequency and V_{DC} dependence of the capacitance in the low frequency region at T = 308K. The inset shows the whole spectrum from 0.01Hz to 1MHz to demonstrate that differences in the capacitance are only introduced by the V_{DC} in the low frequency region.

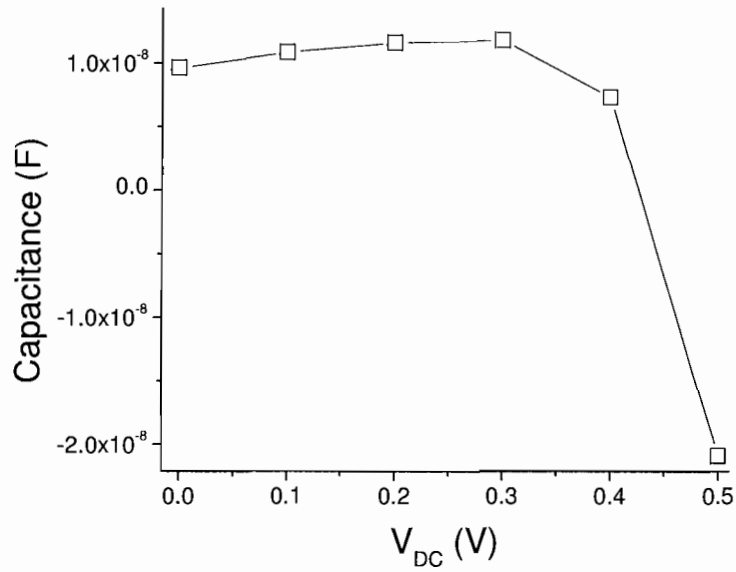

Figure 5.7 Applied voltage dependence of the capacitance at T = 308K for 25mHz.

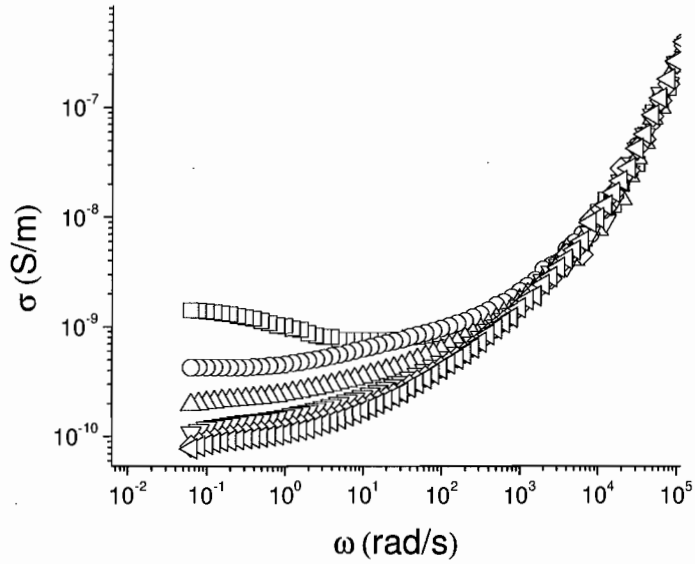

Figure 5.8 Frequency dependent σ for T = 308K under the V_{DC} range from 0V to 0.5V. There is a noticeable increase in the σ when V = 0.5V as the frequency is lowered.

As shown in figure 5.9, σ in the low frequency region goes up as the frequency is lowered at both T = 308K and 328K. However, the degree of increase at 328K is not as dramatic as that at 308K.

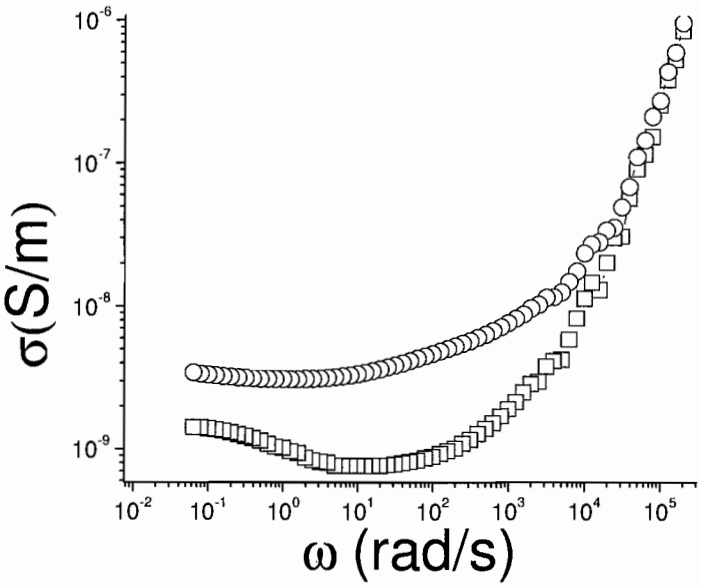

Figure 5.9 Frequency dependent σ at T = 308K (□) and 328K (○) with V_{DC}=0.5V.The increase of conductivity with lower frequency is only present at 308K. At T= 328K, the conductivity only shows a gradual decrease as the frequency is lowered.

5.4 Discussion

5.4.1 Influence of ion motion on impedance measurement

As discussed in the section 4.4.2 in chapter IV, the influence of V_{DC} on the capacitance can be understood within the framework of both electrode polarization and electrode processes at the interface. Therefore, both double layer formation and Faradic processes at the electrodes are key elements in explaining the V_{DC} dependence of the AC

capacitance, as proposed and confirmed in the chapter IV. Similar procedures can be applied in this chapter, except that ions are mobile and need to be included in analysis.

Clearly there is a Faradaic process at the electrodes in which charge is transferred across the interface. The charge transferred causes redistribution of ionic carriers, which leads to the decrease in the ionic space charge concentration close to the interface. Beyond the similarity in the trend of the V_{DC} dependence of the capacitance at low temperatures (173K-233K) and high temperatures (308K-348K), the two do differ in the degree of change upon the application of V_{DC}. The capacitance at low frequency at 308K decreases more dramatically and becomes negative at 0.5V (figure 5.7). Considering that the charge injection is enhanced by the mobile ions at 308K, more electronic carriers can be transported across the interface. The decrease of ionic space charge is more apparent compared with that seen where T = 173K in Chapter IV.

However, it is interesting to note that the σ shows a different frequency dependence at 0.5V from that at the lower V_{DC}. In contrast to the continuous decrease of σ as the frequency is lowered, the conductivity is seen to first decrease and then increase at V_{DC} = 0.5V. The absence of this aberration at T = 173K indicates that it results from the interaction of mobile ions and electronic carriers and that the DC conductivity at low frequency is related to the ion diffusion. In response to the stimulus, ions move towards the interface in response to the electrical stimulus. When the frequency is higher than the typical ion response frequency, the motion of the ions lags behind the electric field.

Thus, the ability of ions to assist the electronic charge injection is limited. At lower frequencies, the ions move fast enough to accommodate the changing electric field, and the charge injection is enhanced tremendously in this case. The differential conductivity therefore increases when the frequency is lower because of the relaxation of ions.

The ion diffusion process is highly temperature dependent. Based on the above analysis, the conductivity enhancement in the low frequency is associated to the ion diffusion process. It is expected that this behavior depends on the temperature also. This makes sense, considering that the ion dynamics is very different at these two temperatures. The ion mobility is higher at 328K, and correspondingly the ion relaxation frequency is higher. The increase in σ occurs at higher frequency, which coincides with the decrease of σ due to the blocking electrode. In addition, ion conductivity increases to a large degree with temperature. The increase of σ due to V_{DC} at T = 328K is overshadowed by the enhancement in the ion conductivity. Therefore it is easier to see the increase in conductivity when the frequency decreases at T = 308K compared with that at T = 328K.

The rise of conductivity in the low frequency region seems to be unique to this system. It results from the coupling of two processes of very different rates: a faster electronic transport process and a slow ion relaxation process. Thus, these results indicate that the impedance analysis under V_{DC} can offer rich information about interactions between electronic and ionic charge carriers.

5.4.2 High DC voltage

At higher V_{DC}, more dramatic changes in the impedance-related functions can be seen in the low frequency region. As shown in figure 5.4 and 5.5, the effects of higher V_{DC} can be summarized as follows:

1. The capacitance in the low frequency region becomes more and more negative.
2. The frequency where the low frequency dispersion starts to take off shifts to higher values
3. The slope of the real part of the permittivity in the low frequency region is about -1.5 when the V_{DC} is above 0.5V.

These results are difficult to explain because the processes involved are not just dielectric relaxation. Indeed, the regime in question contains both substantial charge transport across the interface as well as all of the microscopic dielectric processes such as ion relaxation, electrode polarization, and geometric capacitance charging. Conventional impedance analysis is not enough to account for all of the above contributions. It is necessary, therefore, to go to a time domain measurement and simulation for explanation.

5.4.3 Normalization at various temperatures

Abnormal capacitance at low frequency has been observed in various systems and attributed to different mechanisms specific to the system under study. In devices with anionically functionalized polyacetylene as the active layer, both ionic and electronic

carriers can contribute to the impedance related functions, as shown in the previous chapter. To identify the major source of negative capacitance, AC impedance analysis under V_{DC} with frozen ions was performed in Chapter IV. Large amount of electronic carriers were injected into the device before the ions were frozen. However, the capacitance does not change sign in that case. This indicates that the electronic carriers alone are not enough to create the abnormal capacitance behavior. The dynamic response of ions is necessary for the negative capacitance. Jonscher has proposed an electrochemical model to explain the dielectric dispersion and negative capacitance at low frequencies in electrochemical systems, in which the Faradic process in the region close to the electrodes causes the diffusion of ions from the bulk to the interface[12]. As discussed earlier, this model is sufficient to explain the temperature dependence of the capacitance when the V_{DC} is 0.5V or lower. However, one problem with this model is that with the ion mobility as the dominant factor, the behavior of the frequency dependent capacitance is scalable in terms of temperature, as illustrated in Chapter 3, figure 3.12. Clearly this is not the case for impedance measurements under V_{DC}. The answer must therefore lie in the interaction between the ionic and electronic carriers. When the V_{DC} is higher than 0.5V, the charge injection and transport are largely enhanced by the assistance of ions. This indicates that the system is in the electronic charge transport regime and needs to be treated as an electronic conductor, and not merely as a dielectric material.

The interaction of ionic and electronic carriers can be explored by transient current measurements under V_{DC}. Both types of carriers contribute to the transient current. However, the contribution from ionic carriers is only present at the early times of applied voltage, while the contribution from electronic carriers is closely related to the ion redistribution process and accounts solely for the steady state current. In general, the transient current decays continuously over time with low V_{DC} and starts to increase only when the V_{DC} is 0.5V or more. A detailed discussion of the current transience can be found in chapter VI, section 6.3. The current decay followed by this increase is indicative of inductive behavior in terms of the phase shift between the current and applied voltage. The connection between the measurements in the time domain and frequency domain can be established using a Fourier transform. To build this relationship, the measurement in the time domain is carried out (showed in figure 5.10) and simulations using Fourier transform are done to compare with the results from the frequency domain.

In general, the displacement current associated with the ion redistribution and formation of the double layer is capacitive, (in which the current leads the voltage). At the same time, the electronic charge injection could potentially generate inductive behavior since it usually initiates on a finite timescale related to the redistribution of the ions.

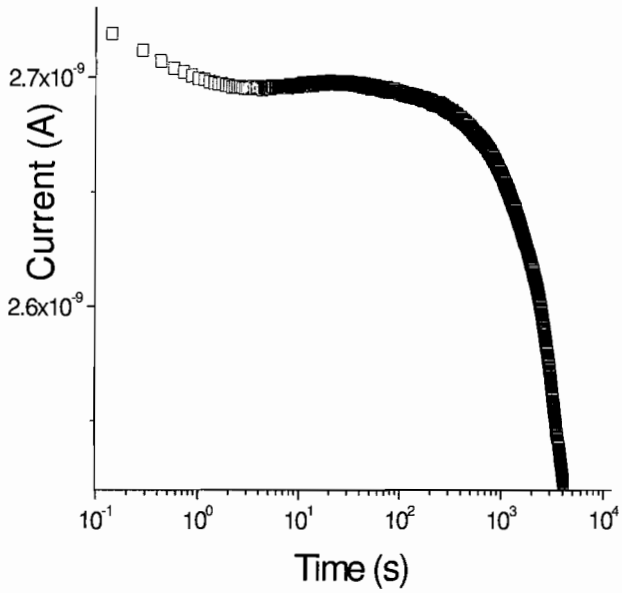

(a) T =308K

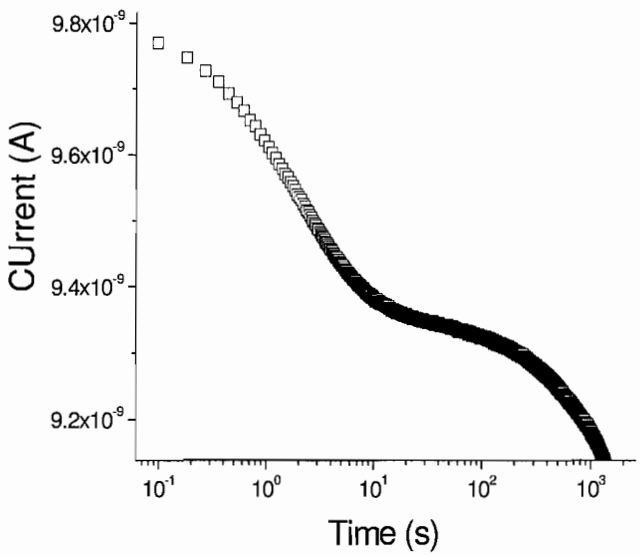

(b) T =328K

Figure 5.10 Transient current measurements at (a). T = 308K and (b). T = 328K as a function of time, both with a V_{DC} of 0.5V.

Experimental results from transient current measurements under applied V_{DC} can be used to infer the properties of the displacement current and the current associated with the electronic carrier injection because the initial current is representative of the former and the steady state current of the latter. The initial current-applied voltage relationship is linear while the steady state current changes exponentially with the applied voltage.

5.4.4 Capacitance calculations [13]

Impedance spectroscopy measurements are related to the time domain measurements by a Fourier transform. The observation of negative capacitance for a great number of diverse materials requires a generally applicable approach for an explanation, rather than assigning the origin to some physical mechanism specific to the system under study. Much work has been done from the viewpoint of defining and calculating the capacitance in the time domain in order to understand the origin of negative capacitance.

The current response to a small amplitude voltage step can be separated into three parts: a step-like current which contributes to the DC conductivity, an impulse-like current which is associated with the geometric capacitance, and a relaxation current ($\delta I(t)$) which results from the dielectric process. The AC capacitance ($C(\omega)$) can be calculated by Fourier transform as follows:.

$$C(\omega) = C_0 + \frac{1}{\Delta V}\int_0^{\infty} \delta I(t)\cos(\omega t)dt \qquad \text{eq. (5.1)}$$

Where C_0 is geometric capacitance, ΔV is voltage step as stimulating signal.

As can be seen from the above equations, the frequency dependence of the capacitance is determined by the cosine transform of the transient current in response to the small step in DC voltage ΔV. One example is depicted in figure 5.11 with both the cosine function with certain frequency and the transient current measured. Depending on the evolution of the transient current, the following three cases are possible:

1. If the transient current decreases monotonically (as in the case where a capacitor is discharged), the transform will be positive for all frequencies.

2. For the monotonically increasing transient current, the real part of its Fourier transform will be negative for all frequencies.

3. If the transient current does not decrease monotonically, the Fourier transform will be positive or negative for a limited frequency range.

Simulations based on equations 5.1 were carried out for two situations: V_{DC} = 0V with a 10mV step (Δ V) at T = 348K and V_{DC} = 0.5V with a 10mV step (Δ V)) at T = 308K. The transient current at T = 348K at V_{DC}=0V was preferentially selected because the current at T = 308K was very noisy. The capacitance calculated from these simulations follows the trend of low frequency dispersion in the measured capacitance at 348K very well, although there are some qualitative discrepancies between the two. However, the similarity is such that it demonstrates that the procedure for the simulation does indeed seem to work. Further simulation based on the transient current at V = 0.5V at T = 308K was also performed and the results are shown above in figure 5.12 and 5.13. The key features, such as low frequency dispersion, negative capacitance at very low frequency,

and a plateau at intermediate frequency are present in both the experimental and the simulated capacitance. These results strongly support the argument that the negative capacitance is closely related to a certain transient current profile, namely the delayed current increase.

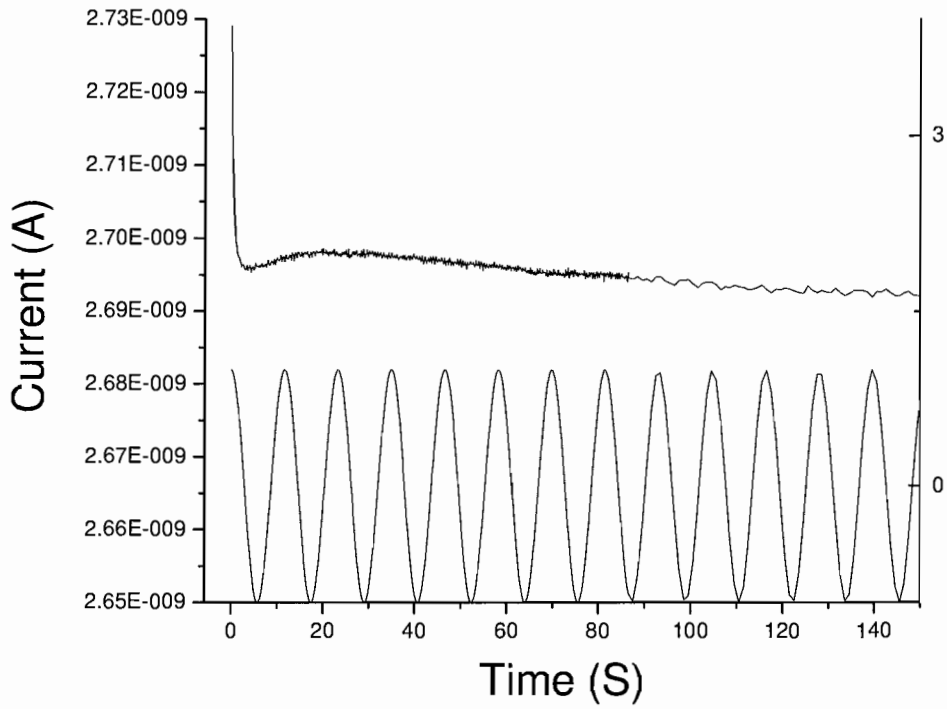

Figure 5.11 Potential step current and Cosine function with period of 1 second as a function of time. The sum of their product is very sensitive to the angular frequency of the Cosine function.

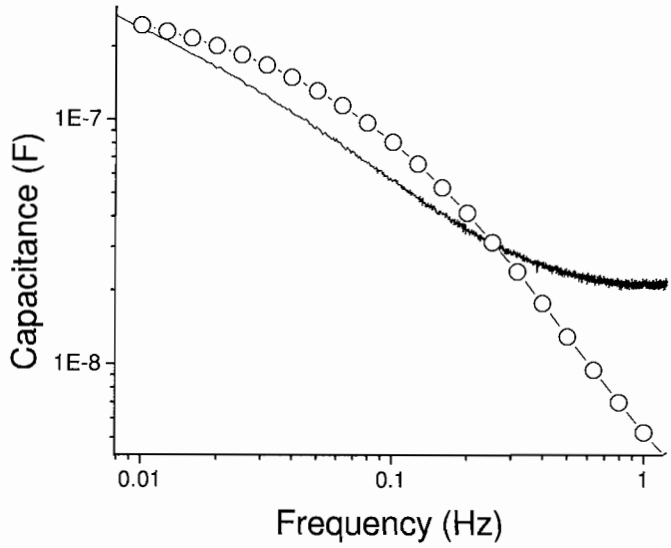

Figure 5.12 Capacitance measured with impedance spectroscopy (○) and that calculated from the Fourier transform of transient current (line) as a function of frequency at T = 348K. The V_{DC} is zero in both cases, while the small amplitude step is 10mV.

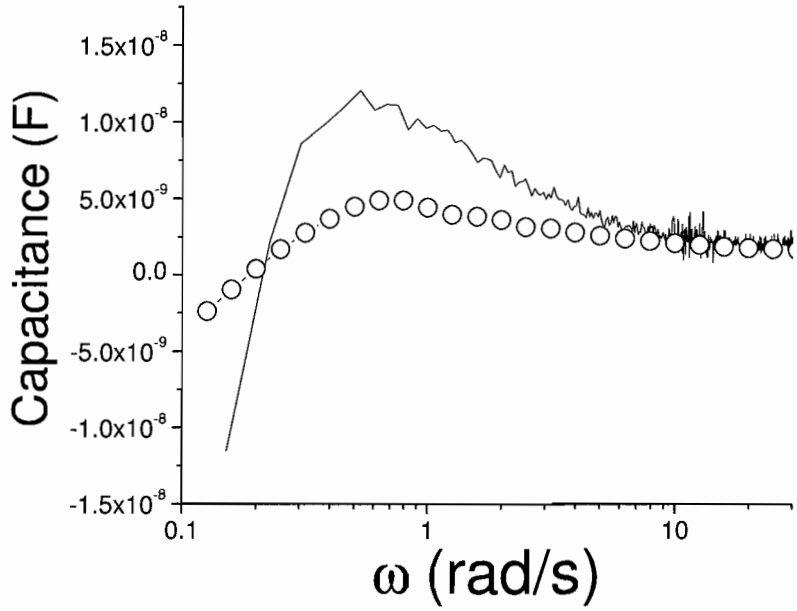

Figure 5.13 Frequency dependence of the capacitance with V_{DC}=0.5V(○) and that from the Fourier transform of the transient current at V_{DC}=0.5V with a small step of 10mV (solid line). The temperature is 308K in both cases.

5.5 Conclusions

The impedance analyses were executed by probing the samples with a small amplitude AC signal while they were under the influence of DC voltage (V_{DC}). It is observed that the capacitance at low frequency (<20Hz) increases modestly with V_{DC} in the range of 0V to 0.3V, and then decreases significantly as the V_{DC} continues to increase. Correspondingly the low frequency conductivity is enhanced when the applied V_{DC} is higher than 0.3V, which indicates that the interaction of electrode polarization and carrier injection is contributing to the V_{DC} dependence of low frequency capacitance.

It is observed that σ increases while the frequency is lowered when the frequency of the electric field is below the ion relaxation frequency. This interesting relationship between the timescale of AC signal and the ion relaxations leads to the theory that the ability of ions to accommodate the change due to the external stimulus is crucial to the charge injection and that charge injection is enhanced due to the ion redistribution. In Chapter VI, this argument will be expanded with the comprehensive investigations of the electrical properties of the anionically functionalized polyacetylene sandwiched between two metal electrodes.

It is observed that capacitance in the low frequency region becomes negative when the V_{DC} is 0.5V or greater. Simulations based on the Fourier transform of the transient current under V_{DC} indicated that the transient current resulting from the interaction of ionic and electronic carriers contributes to this observed negative capacitance. Especially,

the delayed current rise-up that appears only when the V_{DC} is higher than 0.5V gave rise to inductive behaviors, therefore the negative capacitance. In addition, the AC capacitance can be roughly reproduced from the Fourier transform of the transient current.

CHAPTER VI

ELECTRICAL CHARACTERIZATION OF AN ANIONICALLY FUNCTIONALIZED POLYACETYLENE BETWEEN METAL ELECTRODES

6.1 Overview

Recently, there has been extensive studies on light-emitting electrochemical cells (LECs)[1,2]. The presence of ions in the active material of LECs has been shown to affect their electrical properties[3]. However, key issues are still not clear such as the role of ionic carriers on electronic carrier injection, and the carrier and electric field distributions. In this chapter, the charge transport properties of sandwich structures containing the anionically functionalized polyacetylene P_A (see figure 3.1) as the active layer are investigated. Transient current measurements under applied DC voltages (V_{app}) ranging from 0V to 1.5V are carried out. These measurements, combined with data gathered from monitoring the relaxation of samples from steady state under either a short-circuit or open-circuit configuration, are analyzed to infer the carrier and electric field distributions.

6.2 Experimental procedures

Samples were prepared in the same way as described in Chapter 3. During measurements, samples were enclosed in a stainless steel container sealed with a copper gasket and evacuated with an Axiden 2010 standard vane system pump to generate a vacuum of about 20mTorr. The vacuum container was then set in a Sun Electronics EC10 environmental chamber to control temperature. Current-voltage measurements were

carried out with a Keithley 236 source-measure unit, which was controlled by a custom Labview program. Control experiments were done to confirm that the voltage applied did not degrade or irreversibly change the sample. The measurements were also carefully designed to avoid any history effects, in that samples were fully relaxed by a combination of short circuiting and annealing.

There are many measurement techniques involved in this chapter, so it is helpful to describe each of them at the outset:

1. Potential step - the potential is instantaneously stepped from 0V to a steady voltage, V_{app}, and the resulting current transient is measured. The V_{app} ranges from 0V to 1.5V in this chapter.
2. Short-circuit relaxation - samples are first driven to steady state under a certain V_{app}, and then they are switched to a short-circuit configuration, and the current through the short circuit is measured. The V_{app} mentioned in the context of short-circuit current (I_{SC}) measurements refers to the driving DC voltage.
3. Open-circuit relaxation - samples are first driven to steady state under a certain V_{app}, and then they are switched to an open-circuit configuration and the voltage across the open-circuit, V_{OC}, is measured.
4. Fast current-voltage sweep - samples are first drive to steady state under a certain V_{app}, and then a fast linear voltage sweep is conducted while the current is measured.

For any measurement involving a potential step away from equilibrium, the sample was always short circuited for a sufficiently long time so as to return the sample to

equilibrium. Many control experiments were done to test the stability of the samples under the extreme of the measurement situations explored. For example, DC voltages sufficient to pass current densities of ~5mA / cm^{-2} were applied for more than 10 hours at elevated temperatures. The samples showed very good stability under these extreme measurement conditions. For example, sample yjw7272 was tested for 30 hours at 0.1V, 0.5V, 0.8V and 1.2V, as showed in figure 6.1.

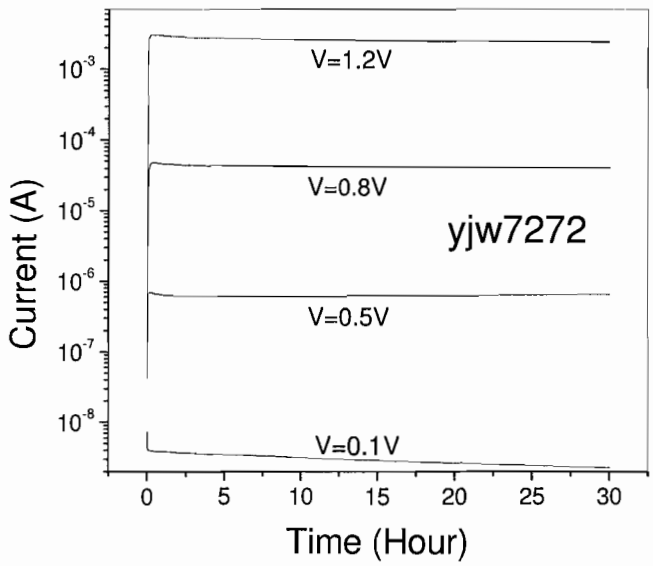

Figure 6.1 Transient current in response to potential steps V_{app} = 0.1V, 0.5V, 0.8V and 1.2V (as labeled) at 328K. There is little change in current for about 30 hours after current reaches a peak at about 1h.

The sample demonstrated exceptional stability at all of these voltages, and there was no sign of degradation even at high current densities (>20mA/cm^2) for 30 hours. The experimental results also showed high reproducibility both for repeated measuremet on

one sample and from sample to sample. Most of the experiments were done at 328K because of both the relatively high ion mobility and good sample stability achieved at this temperature. Temperatures higher than 328K would certainly increase the ion mobility, but the samples cannot be studied over the full range of V_{app} due to the higher DC current and thermal energy. However, some measurements at 308K and 348K were also carried out to explore the temperature dependence of the electrical properties.

To explicitly demonstrate that the relaxation procedure employed sufficiently relaxed the sample, a series of potential steps over the range of 0.1 to 1.5 V was conducted and then repeated. For each step, V_{app} was held for 4 hours and then the sample was relaxed for 8 hours in the short-circuit configuration. The currents measured 4-hours following each potential step are shown in figure 6.2. The potential step measurements showed good reproducibility when the 8-hour short-circuit relaxation protocol was employed.

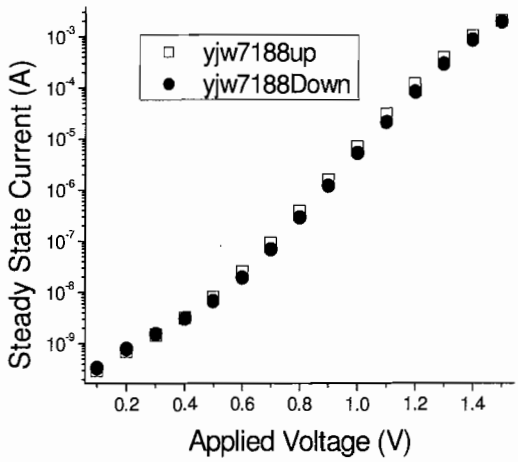

Figure 6.2 Steady-state current from potential step measurements plotted as a function of V_{app} where the filled symbols (●) are from stepping down from 1.5V to 0.1V, and the open symbols (□)) are from stepping up from 0.1V to 1.5V. For each V_{app}, the current at the 4th hour is taken as the steady state current.

6.3 Experimental results

The results of potential step experiments over the range of V_{app}= 0.1V to 1.5V are shown in Figures 6.3 and 6.4. The experimental results are split into two graphs so the features at low (up to 0.7V, Figure 6.3) and high V_{app} (>0.7V, Figure 6.4) can both be clearly identified. As can be seen, the form of the transient current depends on the value of V_{app}. When V_{app} is between 0 and 0.3V, the current decays continuously over the whole period of the measurement. At 0.4V, the initial current decay is followed by a modest upturn at 200 seconds. The upturn becomes more and more apparent as V_{app} increases, and the shape of the current transient after the upturn depends on V_{app}. At V_{app} = 0.5V the current maximizes after the upturn and a peak is observed. As the V_{app} increases, the peaks become less evident giving way instead to a monotonic increase to the steady-state value. Close examination of the current transients in figures 6.3 and 6.4 reveals that the current continues to decrease with time, albeit slowly, after the maximum. It is worthwhile to notice that the percent decrease from the peak current to the steady-state current goes down as the V_{app} increases, from about 50% at 0.5V, to about 6% at 1.5V. This behavior is reproducible when measured again, and therefore, it rules out the possibility that the decrease in the transient current is due to degradation of the material. The implication of these observations will be analyzed in the discussion section. Overall, the change in current after two hours was observed to be minimal, so the sample was considered to be in steady state after holding V_{app} constant for 4 hours. The extent to which steady state had truly been achieved can be seen in figure 6.1, which shows current transients out to thirty hours. The current at 4 hours is similar to that at 30 hours.

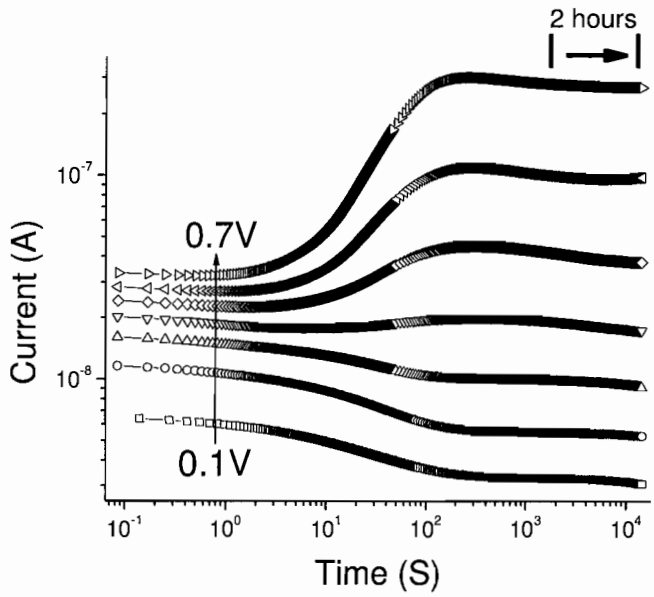

Figure 6.3 Transient current in response to potential steps in the range V_{app} = 0.1V to 0.7V (as labeled) and plotted in a log-log scale to show the major features at all the time scales involved.

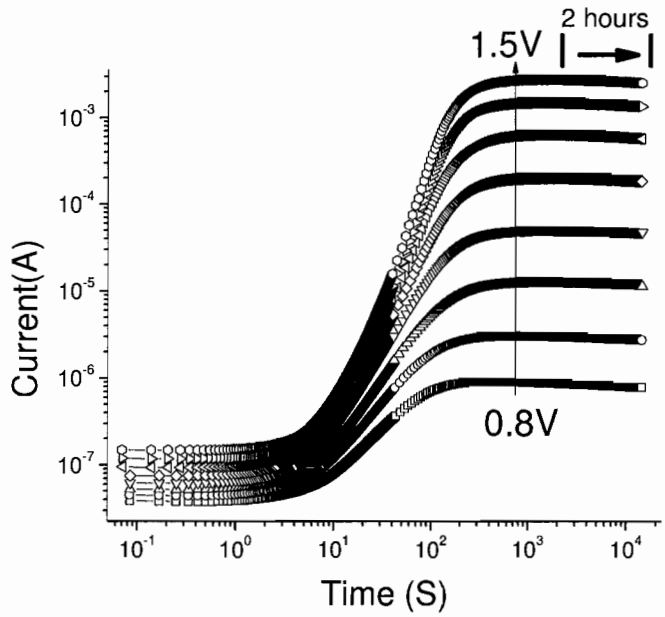

Figure 6.4 Transient current in response to potential steps in the range V_{app} = 0.8V to 1.5V (as labeled) and plotted on a log-log scale.

The current at 4 hours after the potential step, which as described above, is taken as the steady-state current, I_{SS}, is shown in Figure 6.5 as a function of V_{app}. The I_{SS}-V_{app} curve has a sigmoidal shape in the semilogaritmic representation of Figure 6.5, with I_{SS} increasing more rapidly with intermediate V_{app} than with lower or higher V_{app}. The I_{SS}-V_{app} relationship is clearly different from what predicted by the space charge limited current model, as discussed in section 1.7 of chapter I.

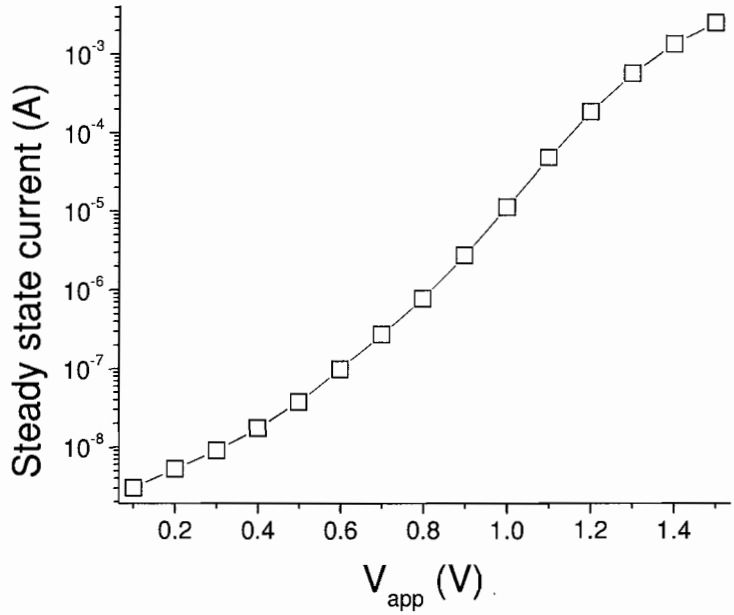

Figure 6.5 Steady-state current versus V_{app}.

As discussed in chapter III, section 3.2.2, impedance studies were used to conclude that ion transport in the polymer is a thermally activated process with an activation energy of about 0.98eV. Hence, the current transients of the Au | P_A | Au structure are expected to be strongly temperature dependent with the temperature dependence

providing insight into ion dynamics. Consequently, potential step experiments were performed at a limited number of temperatures. Figure 6.6 shows the results of potential step experiments at T = 298K, 315K and 328K. Data with V_{app} = 0.6V are shown because at intermediate voltages such as this, the current transient shows the richest behavior. The curves at the various temperatures are similar in shape, but the onset time (t_{onset}), corresponding to the large increase in current, shifts earlier as the temperature increases.

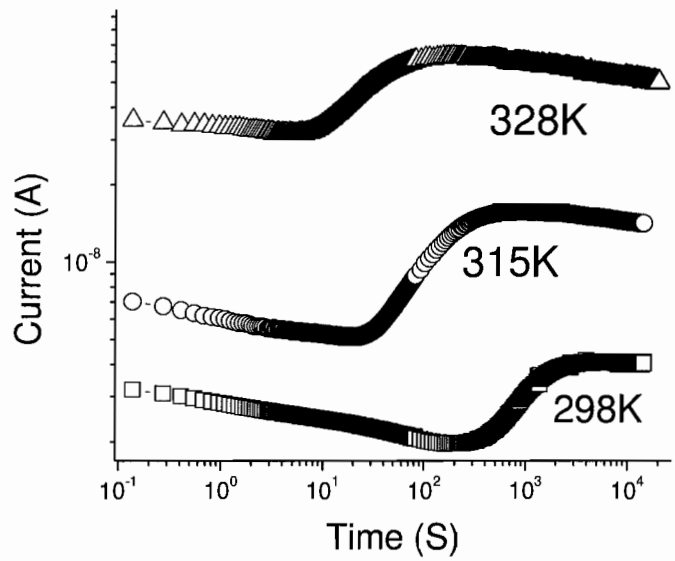

Figure 6.6 Transient current in response to a potential step with V_{app}=0.6V at T = 298K, 315K, and 328K (as labeled) for sample yjw8080A.

The t_{onset} is indicative of the timescale for double layer formation, and consequently, the activation derived from the temperature dependence of this timescale should correlate with that measured for the ionic conductivity using impedance measurements (see Chapter 3). Figure 6.7 shows the temperature dependence of t_{onset}^{-1}, and the resulting

activation energy was calculated to be 1.04 eV, which is very close to that measured using impedance spectroscopy.

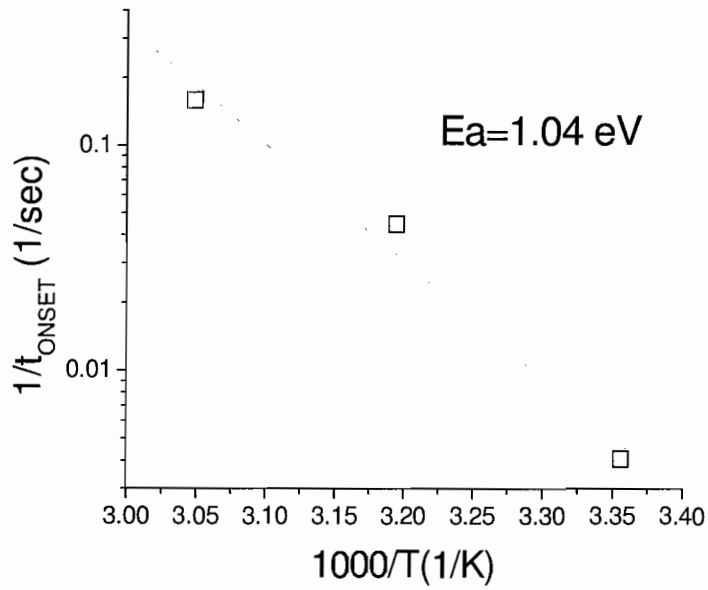

Figure 6.7 Arrhenius plot of t_{onset}. The derived activation energy is 1.04eV.

When the Au | P_A | Au structures are subjected to a potential step there is presumably a substantial redistribution of ions and injection of electronic charge carriers. As discussed below, these processes lead to the complex current transients measured in the potential step experiments above. Additional insight into the steady-state charge distribution was pursued by using three different types of measurements: short-circuit relaxation from steady-state, open circuit relaxation from steady-state, and fast IV characterization of the steady-state.

Figure 6.8 shows the results of short-circuit relaxation measurements. These I_{SC} transients show decays that cannot be described simply by either

exponential or power law behavior. By integrating the I_{SC}, the charge injected into the sample can be estimated. The total charge extracted using this method increases exponentially with V_{app} during the potential step, as shown in figure 6.9.

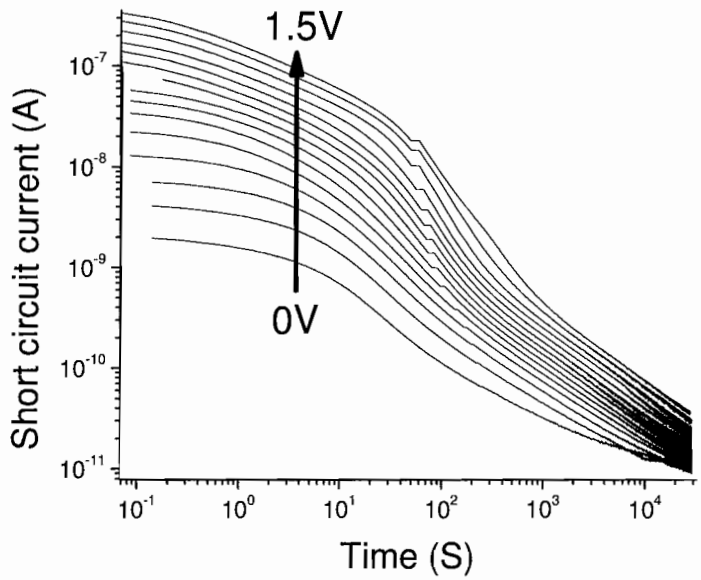

Figure 6.8 Short-circuit relaxation current after a potential step of V_{app} from 0.1V to 1.5V had been applied for 4 hours.

The results of open-circuit relaxation measurements for V_{app} from 0.1V to 1.5V are showed in figure 6.10. The arrow indicates how the first measured voltage in the open-circuit configuration (V_{OC}) changes with V_{app}. Figure 6.11 shows this initial V_{OC} as a function of V_{app}, and it first increases fairly rapidly with V_{app} and then reaches a plateau at about 0.5V.

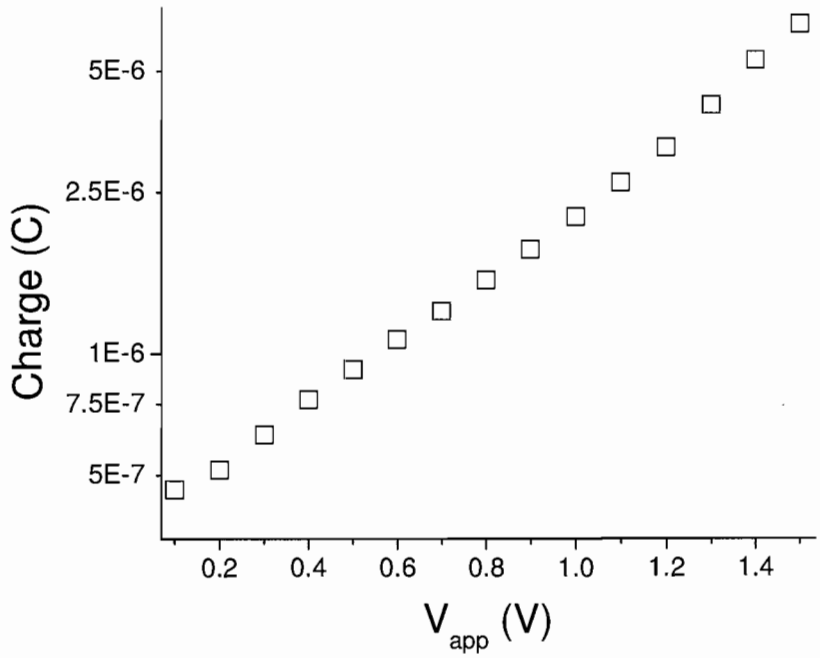

Figure 6.9 Relationship of the total charge extracted from integration of the short-circuit relaxations as a function of V_{app}. The plot is on a log -linear scale, therefore the amount of charge collected from the transient I_{SC} exhibits an exponential dependence on V_{app}.

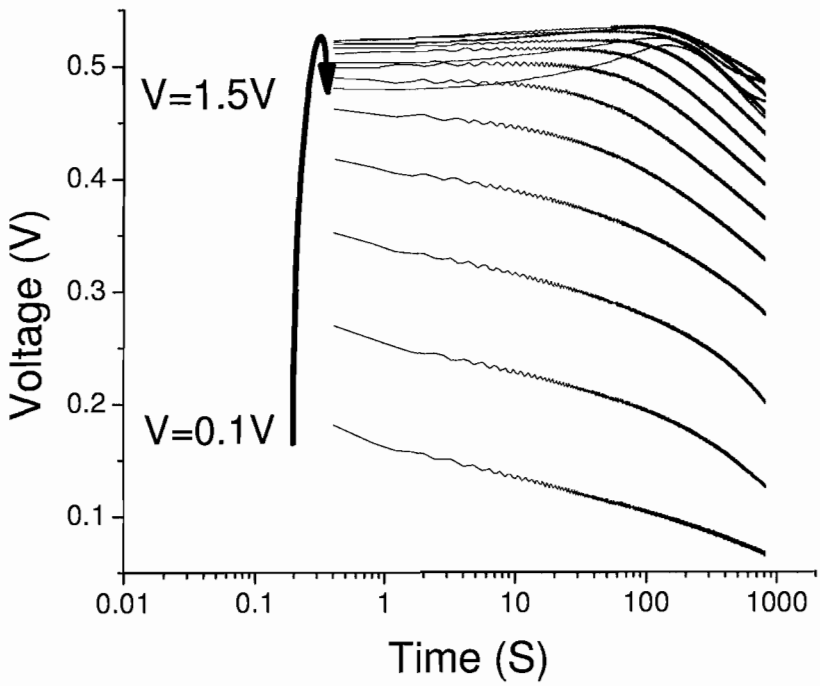

Figure 6.10 Open-circuit voltage (Y axis) after the sample has been prepared to steady state. The V_{app} is indicated in the graph.

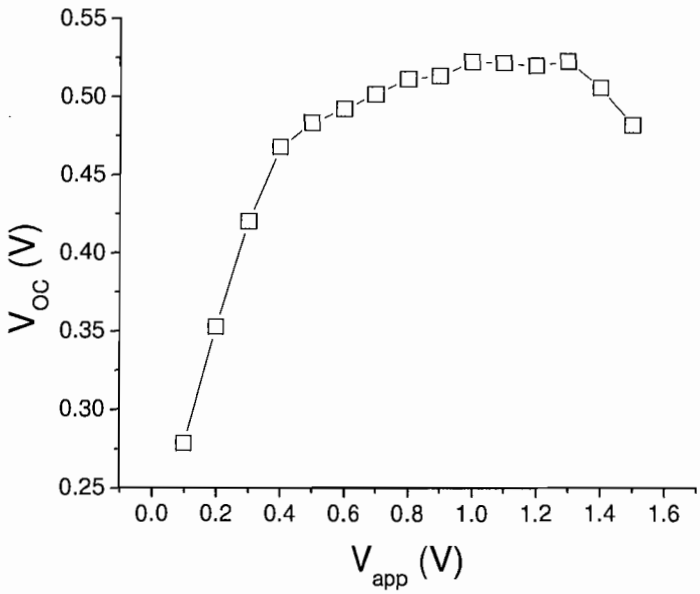

Figure 6.11 Initial open-circuit voltage V_{OC} vs V_{app}

The results of fast current-voltage measurements at 10V/s and immediately following a 4 hour potential step to V_{app} are shown in Figure 6.12 (top graph). Rectifying behavior is observed. In these rectifying curves, the current is negative at 0V and remains negative until a forward bias (positive in Figure 6.12) is increased up to certain value. The forward bias at which the current becomes zero is an open-circuit voltage, which is showed in figure 6.12 (bottom graph).

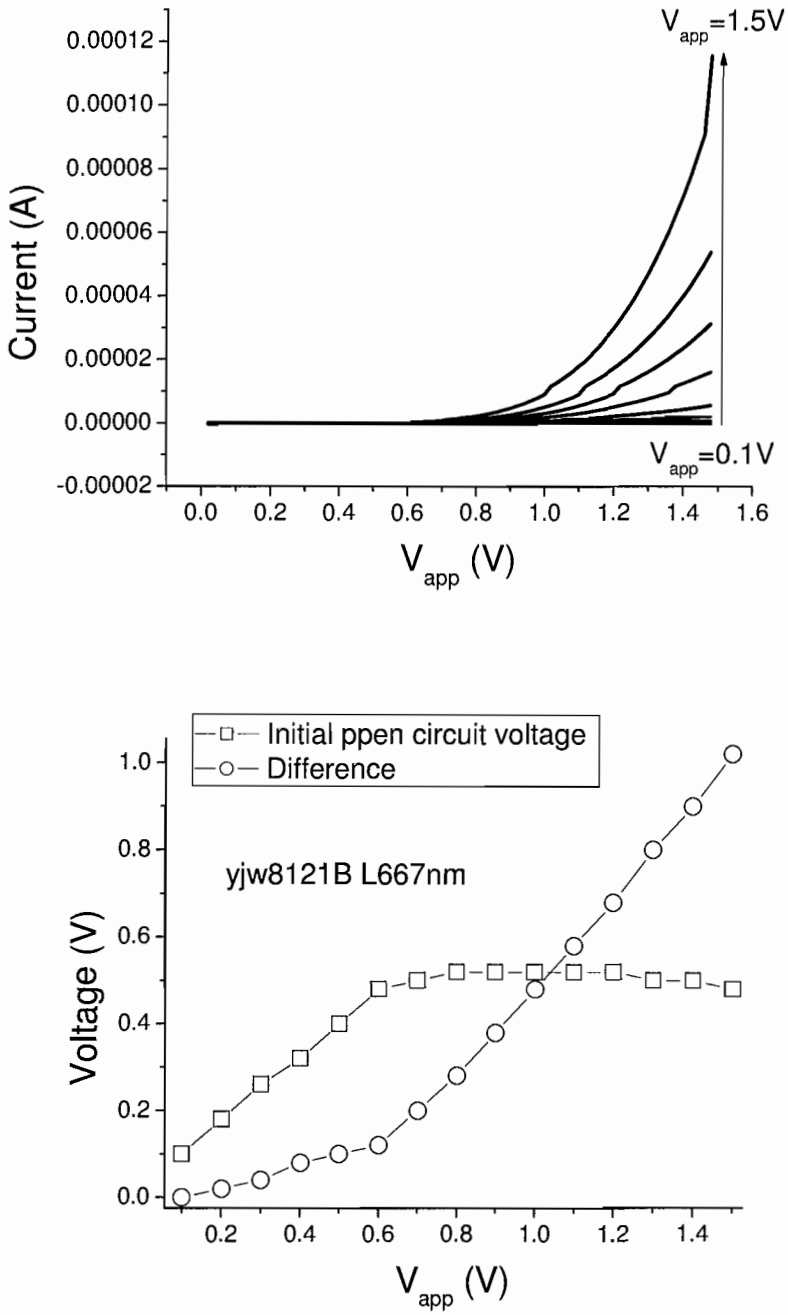

Figure 6.12 Linear current-voltage sweep measurements and open-circuit voltage. In the top graph, current-voltage measurements with a scan rate of 1 V/s are shown from 0V to 1.5V and immediately following a 4 hour potential step at V_{app}. In the bottom graph, the initial open circuit voltage, V_{oc}, from the fast linear voltage sweep shown in top graph and its difference (V_a) from the value of V_{app} are compared.

The open-circuit relaxation (figure 6.10 and 6.11) measurements and the fast linear current-voltage sweep (figure 6.12), which also yields an open-circuit voltage, are different techniques in that they are probing the state of the sample with very different electrical configuration. Despite some differences in the values, the open-circuit voltages from the two methods are consistent in that they both show an increase of the built-in potential with V_{app} up to about 0.5V, and then a plateau as the V_{app} is increased beyond this point. The consistency between the results from the two different techniques effectively validates these measurements.

Due to the interaction between the ionic and electronic carriers, the field and carrier distribution within the bulk and across the interface evolves towards a steady state when the sample is under V_{app}. The status of the sample at any particular moment can be probed by short-circuit measurements by varying the duration (t_d) of the potential step before short circuiting. I_{SC} with potential-step experiments ranging from t_d=5 sec to t_d =4 hours were performed with V_{app} of 1.5V. As shown in figure 6.13 for t_d = 5 sec, the shape of the I_{SC} is reminiscent of those with low DC voltage (<0.8V). The behavior of the I_{SC} decays as a function of t_d follow the same trends as the short-circuit decays from steady state as a function of V_{app} from 0.1V to 1.5V. The initial discharge current is plotted versus the driving duration in figure 6.14. The results from potential-step experiments are also included in this graph for comparison. The initial short circuit current over t_d follows the potential step current transience very well, with a sharp rise-up first, followed by a plateau.

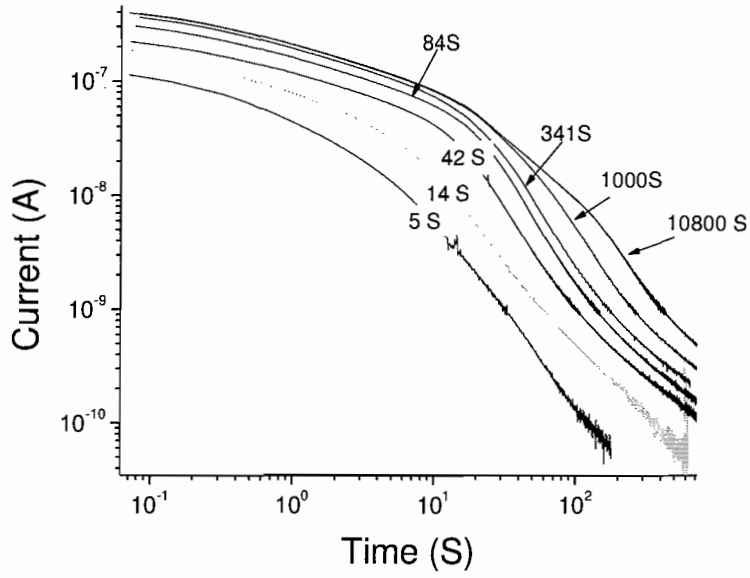

Figure 6.13 Short-circuit relaxation current following a potential step of V_{app} =1.5V as a function of the duration of the potential step (as labeled).

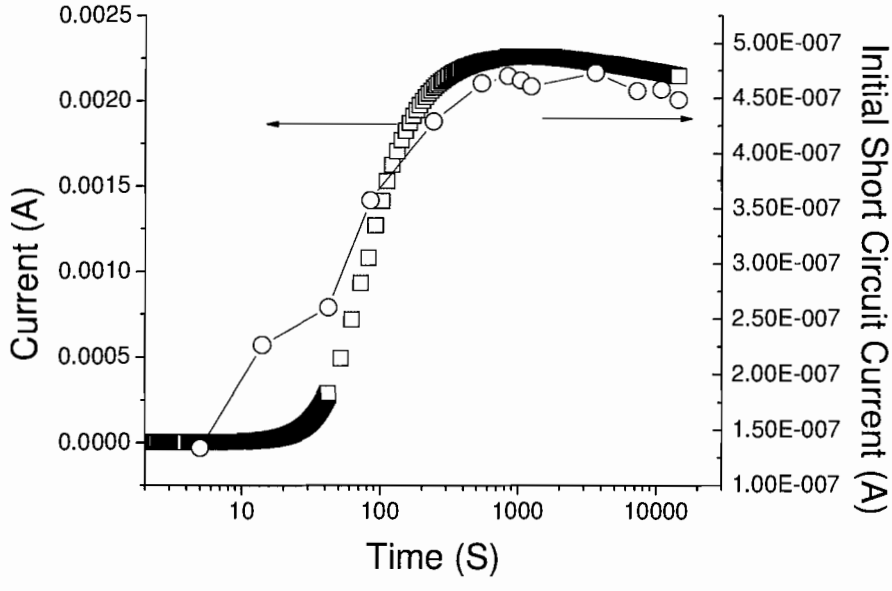

Figure 6.14 Current on the left axis and initial I_{SC} on the right axis as a function of time.

At the same time, the charge versus t_d exhibits a different behavior from the steady-state charge versus V_{app} in that the former increases linearly with t_d , as showed in figure 6.15. Clearly the amount of charge injected and stored in the sample keeps on increasing even when the potential step current reaches a peak and begins to decay slightly.

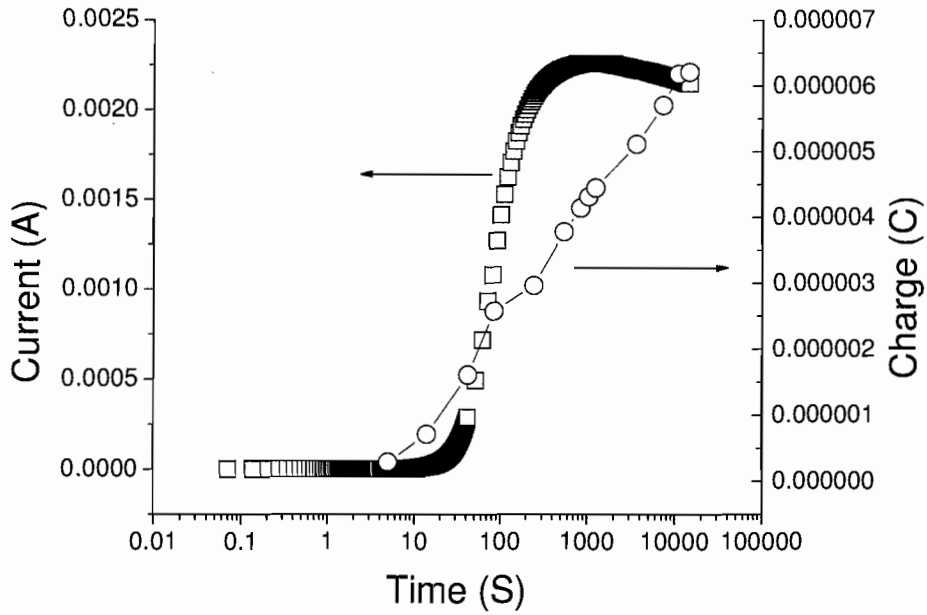

Figure 6.15 Current on the left axis and charge on the right axis as a function of time

Potential step measurements were also performed on samples with thicknesses ranging from 200nm to 1800nm. The steady-state currents I_{SS} in response to a potential step for these samples are plotted in figure 6.16. The I_{SS} at a given V_{app} decreases as the sample thickness increases. The inset in figure 6.16 shows I_{SS} normalized by the thickness of each sample. Four I_{SS}-V_{app} curves collapse into one curve after the normalization, except at the lowest V_{app}. The fact that values of I_{SS} converge after the

normalization reveals I_{SS} is inverse-linearly related to the thickness of the sample.

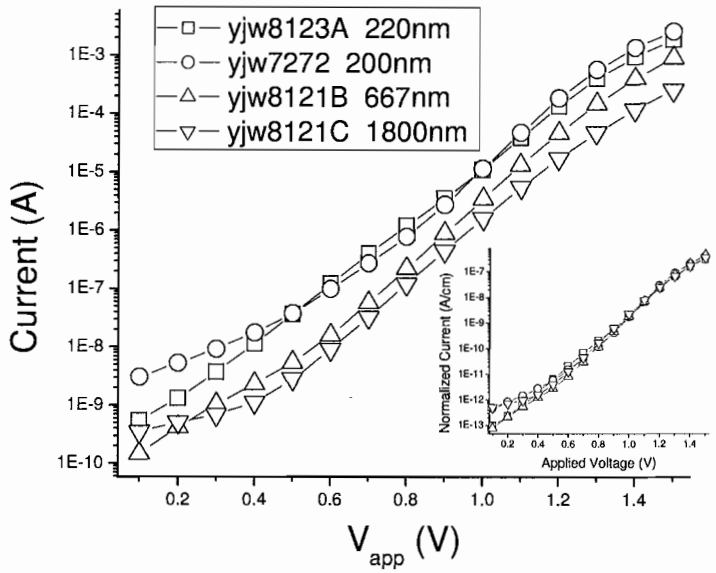

Figure 6.16 Thickness dependence of the steady-state current with samples of thickness 200nm, 220nm, 667nm and 1800nm. The inset showed the current normalized with sample thickness.

The short-circuit relaxation current following a 4 hour potential step at V_{app} = 1.5V as a function of thickness is shown in figure 6.17, and this data illustrates the thickness dependence of the discharging behavior. There is a clear trend that the thicker samples more closely follow a power law behavior over a wider range of time. The power indexes are about the same over a near 10-fold variation in the thickness (from 200nm to 1800nm). There is a negligible difference in the initial I_{SC} considering the large thickness range (200-1800 nm) involved. Much larger differences can be seen in

the longer-time regime of the short-circuit current. A shoulder is observed in samples with thicknesses of 667nm and 1800nm.

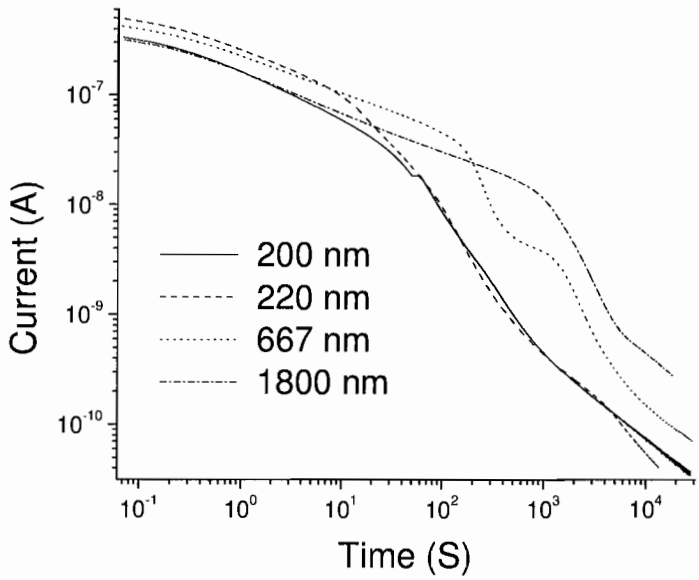

Figure 6.17 Comparisons of transient short-circuit current at 1.5V with thicknesses ranging from 200nm to 1800nm. Thickness of each sample is indicated in the legend.

A plot of the charge calculated from the short-circuit decay from steady state versus the value of V_{app} also shows a thickness dependence, as shown below in figure 6.18. Clearly, the two thicker samples store 10 to 15 times more electronic carriers than the samples of 200nm do at high voltage (>1V).

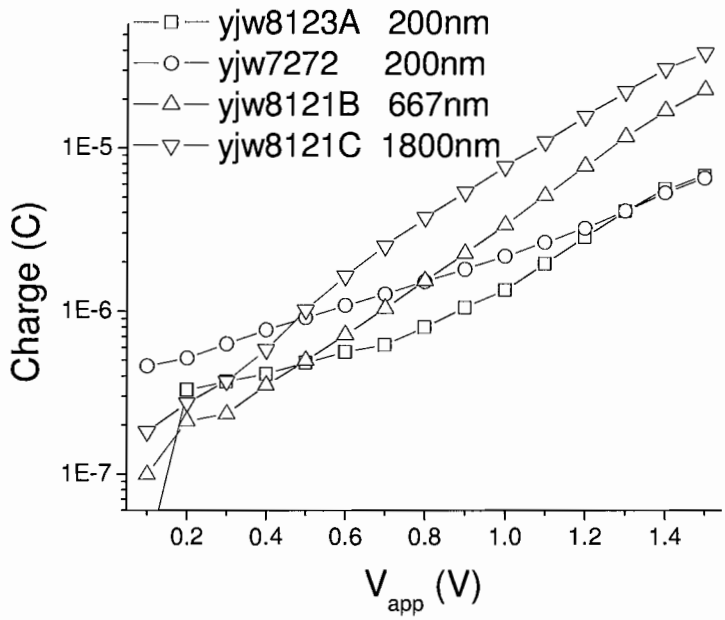

Figure 6.18 Charge versus V_{app} with samples of various thicknesses. At higher voltages, it is clear that thicker samples store more charge. The trend is not so apparent at voltages lower than 0.6V.

6.4 Discussion

The goal of the work presented in this Chapter is to develop a better understanding of the distribution of ions and electrons in P_A as a function of bias and time. The data support the following qualitative picture regarding the response of P_A to a potential step[4].

1. Ions move toward the interface to form a double layer. The initially uniform field is redistributed with large fields forming at the interfaces and a reduction of the field in the bulk.

2.The formation of large electric fields at the interfaces substantially increases the rate of carrier tunneling and hence the injection of electronic charges is enhanced.[5]

3a. At low bias, the average density of injected electronic charge carriers remains below the effective density of ionic charges. The large of excess of ions near completely screens the bulk from the charges on the electrodes and the electric field in the bulk is near zero[6]. The steady-state transport of carriers across material is driven by diffusion.

3b. At high bias, the average density of injected charge carriers at steady-state exceeds the effective density of ionic charges. The electric field distribution is determined both by the ionic and electronic carriers and the electric field in the bulk is significant. The steady-state transport of carriers across the material is driven by both drift and diffusion [7].

The above sequence of events is mapped onto an energy level diagram in Figure 6.19 and 6.20. Figure 6.19 shows the relative energy line-ups of the metal Fermi surface and the LUMO and HOMO of the organic compound P_A with no applied bias. The energy levels are estimated from previous cyclic voltammetry studies[8]. Figure 6.20 compares the equilibrium energy-level diagram with the steady-state diagram under the low and high bias conditions described above.

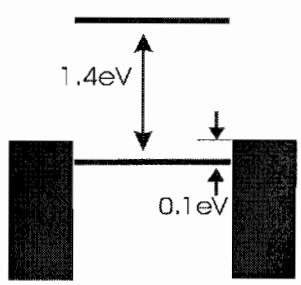

Figure 6.19 Energy level diagram of the Au|P_A|Au device. The Fermi level of the gold electrode is closer to the valance band of the polymer than to the conduction band edge.

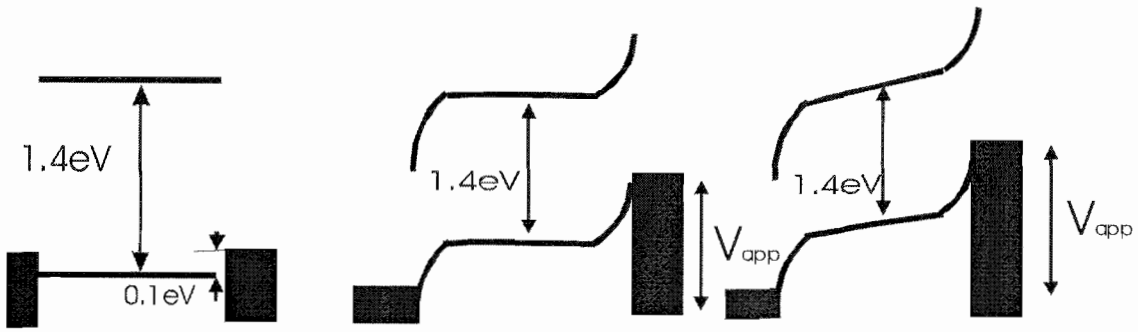

(a) (b) (c)

Figure 6.20 Energy level diagram of the Au|P_A|Au device under (a) zero V_{app} , (b) low V_{app} , and (c) high V_{app}. Solid lines represent the energy levels of polymer, while the rectangle box represents the energy band of gold.

The initial polarization of ion (Step 1 above) and the subsequent injection of electronic charge carriers (Step 2 above) are supported by the following observations.

1) As is most noticeable at low bias, the current in response to a potential step initially decreases with time consistent with the polarization of ions against blocking electrodes to form a double layer. Except at the very lowest voltages, this current decrease then gives way to an increase supporting the idea that double layer formation enhances the injection of electronic charge carriers. At the lowest values of V_{app}, the interfacial electric field is not yet sufficient to drive substantial carrier injection, and a pronounced increase in the current is not observed.

As showed in figure 6.7, the activation energy from potential-step experiments is about the same as that calculated from the impedance measurements in Chapter 3 (see section 3.2.2). The absolute time scale for t_{onset} is also comparable to that assigned to the electrode polarization process in the impedance studies. The values of t_{onset} at 315K and 328K are 6.3 seconds and 22.3 seconds respectively. The corresponding values of t_{onset}^{-1}

are 0.142 Hz and 0.045 Hz, respectively. The electrode polarization frequencies from impedance measurements at these two temperatures are 0.15 Hz and 0.05Hz respectively, which are very close to the frequencies calculated from the onset time. The fact that the two sets of data match very well confirms the connection between the electronic carrier injection and the formation of a double layer. This is a strong support for the argument that the charge injection is enhanced by the ion redistribution.

2) The substantial redistribution of ions that occurs upon application of bias is also evident from the decay measurements from steady state. Any non-equilibrium density of electronic charge carriers that are not coupled to ion motion will relax faster than the time scale of either the open-circuit or short-circuit decay measurements. The earliest time point for these measurements is 0.1s. As discussed in Chapter 4, the timescale for electronic carrier motion is much greater than kHz at room temperature, and hence, any redistribution of electronic carriers will be complete prior to the first time point in the relaxation measurements. The substantial current and open-circuit voltage measured further illustrate the substantial redistribution of ionic charge carriers that occurs upon application of a potential step. Such long-time transients would not be observed in more conventional electronic devices.

Due to the limited speed of the measurement, the open circuit measurement can only detect the potential related to the ionic space charge. At the temperatures used for these experiments (298K to 328K), the electronic carrier relaxation is too fast to measure. Therefore, the contribution from the electronic carriers in the bulk to the potential becomes zero before the first voltage reading (V_{oc}) is collected. The difference between

V_{app} and the measured open circuit voltage (V_{oc}) is then related to the internal electric field resulting from the electronic space charge.

3) As high as a mA/cm^2 steady-state current is achieved with V_{app} = 1V. In contrast, in organic LEDs, which are very similar to Au|P_A|Au except for the absence of ions in the active layer, the charge transport is often inhibited by the difficulty in overcoming the barrier at the interface[9,10,11]. Often voltages much higher than 1.5V need to be applied before substantial current (mA/cm^2) can be observed. This contrast between the Au|P_A|Au structure and organic LEDs confirms the role of ions in enhancing the electronic carrier injection. In addition, potential step measurement on samples with thicknesses ranging from 200nm to 1800nm demonstrate that the charge transport is a bulk-limited process, which is consist with the idea that charge injection is enhanced due to ionic space charge at the interface. A fundamental parameter for determining charge transport through the polymer device is the dominating transport mechanism: interfacial charge injection or hopping transport in the bulk [12,13,14]. Heterogeneous charge transfer kinetics at the Au|anionic-functionalized polyacetylene (P_A) interface strongly depends on the electrical field at the interface. In the Au|P_A|Au system, the redistribution of ions contributes to both a double layer and a high electric field at the interface. The double layer is dependent on V_{app}, temperature, the types of ions and ion concentration, but not on the thickness of the sample. Figure 6.16 shows that the steady state current is inversely related to the thickness of the sample. This indicates that the conduction mechanism in MIECs is dominated by charge transport in bulk rather than interfacial charge injection.

6.4.1 Low voltage regime (V_{app} up to 0.7V)

The ultimate steady-state field distribution depends on V_{app}. The assertion that the field is near zero in the bulk for V_{app} <0.7 (3a) is supported by a number of observations.

1) The initial V_{oc} follows V_{app}. As mentioned above, the timescale at which the potential in the bulk is dissipated by the electronic carriers is much smaller than the measurement time. Therefore, any contribution to V_{oc} from uncompensated electronic carriers will relax before the initial V_{oc} is collected. The fact that the initial V_{oc} follows V_{app} so closely indicates that the field distribution within the material is mostly determined by the ion distribution. Since the electrodes are blocking to ionic carriers, the steady-state ionic current is zero, and there is no ionic space charge in the bulk. According to Gauss's law, the electric field is zero.

2) The dominance of the ionic carriers in shaping the potential distribution, and hence to a near zero electric field in the bulk, for $V_{app} < 0.7$ is also supported by the observation that the injected electronic charge density remains below the effective mobile ion density. The density of injected electronic carriers (n_e) can be estimated from the short-circuit measurements, in which the portion of the electronic carriers that recombine through external routes are collected. A crude calculation shows that when V_{app} is about 0.6V, n_e is about $10^{19}/cm^3$, which is comparable to the effective ion concentration (n_{ion}) calculated from the electrode polarization modeling in chapter III. The fact that the n_e remains below the effective mobile ion density also explains the decay in the potential step experiments following the peak, which is most strongly observed in the lower voltage regime. The ion redistribution is a very slow process, and the continued formation of

electric double layers and reduction of the internal field to near zero continues well after the majority of the electronic charge carriers have been injected leading to a decrease in the drift and overall current. The net result of the charge injection enhancement and the drift current reduction, both due to ionic double layer formation, results in a maximum followed by a decay. The above description is best illustrated in figure 6.21.

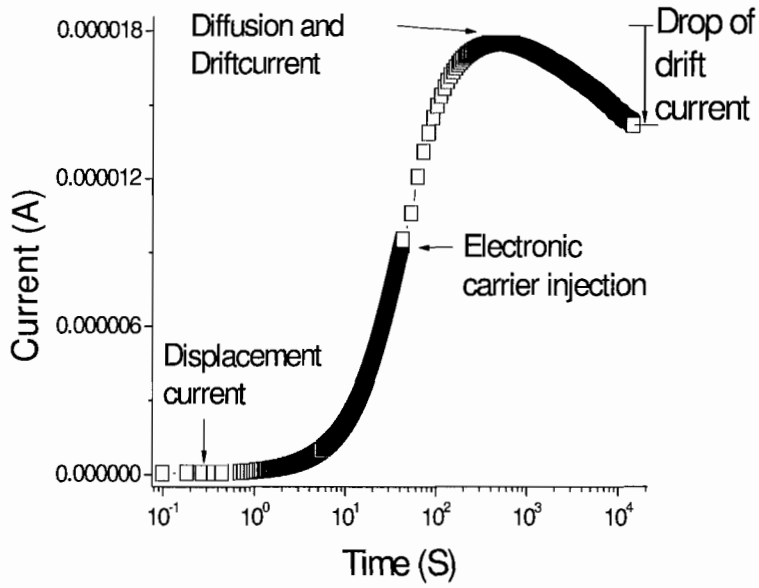

Figure 6.21 Plot of the transient current separated into four regions to indicate the evolution of both the electric field and transport properties.

6.4.2 High voltage regime (V_{app} > 0.7V)

At higher V_{app} , the assertion that there is substantial field in the bulk is supported by the following observations.

1) The initial V_{oc} starts to saturate at 0.5V when the V_{app} is 0.7V. Consequently the discrepancy between V_{app} and V_{oc} increases linearly as showed in figures 6.11 and 12.

As discussed before, the contribution to V_{oc} from electronic carriers decoupled from the ionic carriers relax much quicker than the timescale of the measurement. The ever-increasing discrepancy between V_{app} and V_{oc} at high V_{app} suggests that the electronic carriers in the bulk are assuming significant portion of V_{oc}. The electric field in the bulk is then non-zero since the electronic space charges induce a potential gradient within the polymer.

2) The result that the density of injected electronic carriers is higher than that of effective ionic carriers at high V_{app} (>0.7) also supports the argument that the electronic carriers contribute to the electric field. In this case, the dominance of ionic carriers is broken, and the electric field is jointly determined by both the ionic and electronic carriers.

3) The assertion that the electric field is non-zero in the bulk is consistent with the potential step experiments at high V_{app} (>0.7V). As we can see in figures 6.3 and 6.4, the current decay after its maximum at high V_{app} is much less than that in low V_{app}. The screening of the electrical field in the bulk reduces the drift current. The smaller drop in current following its maximum at high V_{app} implies incomplete screening, and therefore a persistent drift current.

The above analysis indicates that the n_e in comparison to n_{ion} is crucial in understanding the electrical characteristics of the Au|P_A|Au structure. The electric field distribution can change from mostly determined by ionic carriers to jointly determined by ionic and electronic carriers when n_e is comparable or higher than n_{ion}. A direct way to probe the n_e is the potential step experiments followed by the relaxation through a short

circuit configuration. As we will see, analysis of I_{SC} provides information about the charge distribution, and further strengthens the assertions.

6.4.3 Discharging behavior in the short-circuit configuration

There are four possible sources of electronic carriers in the system: electrons (Q_1) on the cathode, holes (Q_2) on the anode, and electron (Q_3) and holes (Q_4) inside the devices. Charge neutrality requires the following relationship:

$$Q_1+Q_3=Q_2+Q_4 \qquad \text{(eq 6.2)}$$

The above description, in combination with the assertions above (step 1,2,3) can be best illustrated with figure 6.22, which shows the steady charge and electric field distribution under $V_{app,}$ and the corresponding short circuit current decays.

Also in the figure 6.22, the concept of unipolar charge injection proposed by several groups [15,16,17] was adapted and applied the of the ionically functionalized polyacetylene sandwich structure studied herein.

The I_{SC} can roughly be divided into two sections based on its slope in a log-log scale: section 1 at early time with low slope, and section 2 at later time with high slope. The connection between the I_{SC} behavior and the steady-state charge distribution resulting from a potential step is illustrated in the bottom graphs of figure 6.22. This connection is described as follows and is based on the results and analysis in the earlier part of the discussion section:

Behavior 1: in the potential step experiments with low V_{app} (V<0.7), the n_e is much less than the effective density of mobile ions. The discharge is dominated by the electronic

carriers on the surface of electrode which are coupled with the ionic space charge in the interface region. The I_{SC} in figure 6.22 (a) shows behavior typical for the discharge of a double layer capacitance[15,16]. These observations are consistent with the argument that the electric field is formed mostly due to ionic carriers, and that in the bulk, the field is near zero.

Behavior 2: in the potential step experiments at high V_{app} (>1V), the electronic carrier injection increases greatly and n_e is much larger than n_{ion}. Therefore, a large amount of electronic space charge is present in the bulk, and there is an electric field within the polymer supported by electronic carriers. The discharge of electronic carriers on the electrodes is now under the influence of both ionic carriers at the interface and the electronic carriers in the bulk. The early part of the short-circuit relaxation current (<100 seconds) shows power law behavior with an index of 0.33. Another noticeable feature is a shoulder appearing in the latter parts of the short circuit relaxation current, as shown in figure 6.22 (c) and which will be discussed later.

Behavior 3: the short circuit current decay behavior at intermediate V_{app} (0.7V<1.0V) is a smooth transition between the behaviors described above for low and high voltages, with only a modest sign of power law behavior in the early time portion and the absence of shoulder at later times.

The connection between the injected electronic carriers and the I_{SC} behavior is further supported by the observation that the short circuit current with V_{app}=1.5V for short t_d is very similar in shape to that with low V_{app} (<0.7V) with t_d = 4 hours. Apparently, V_{app} exerts influence on the I_{SC} by way of tuning the amount of injected carriers through either

magnitude or duration. The factor that really matters is the n_e. At both the low V_{app} (<0.7V) and short t_d (<100 seconds at V_{app} = 1.5V) , the n_e is considerably less than that of n_{ion}. Therefore behavior 1, which is characteristic of a double layer capacitor, is observed in both cases.

Additional connections between injected charge carriers and two characteristic time sections in the I_{SC} can be established with the following analysis. As argued previously, by the time the potential step current reaches the maximum, the double layer has mostly formed, hence the charge distribution (ionic and electronic) in the interface region is largely in a steady state. The discharging behaviors of the charge carriers in the interface region then do not increase any more with longer potential step duration (t_d) than required for double layer formation. The fact that short-time regime of the short circuit current saturates at about the same time with the potential step current (figure 6.14) suggest a connection between the I_{SC} in short-time regime and the electronic charge in the interface region. The I_{SC} in long-time regime is then related to the discharge of carriers in the bulk.

This assignment is supported by results from the thickness dependence of the I_{SC}, as shown in figure 6.17. Notice that the I_{SC} in short-time regime is almost thickness independent, while that in long-time regime is affected considerably by the thickness. The thickness is inherently related to bulk properties. The fact that it only affects the short circuit current in long-time regime strongly supports the argument that the I_{SC} in short-time regime is due to the discharging of carriers on the electrodes, while the later section of the I_{SC} results from the discharge of electronic carriers in the bulk.

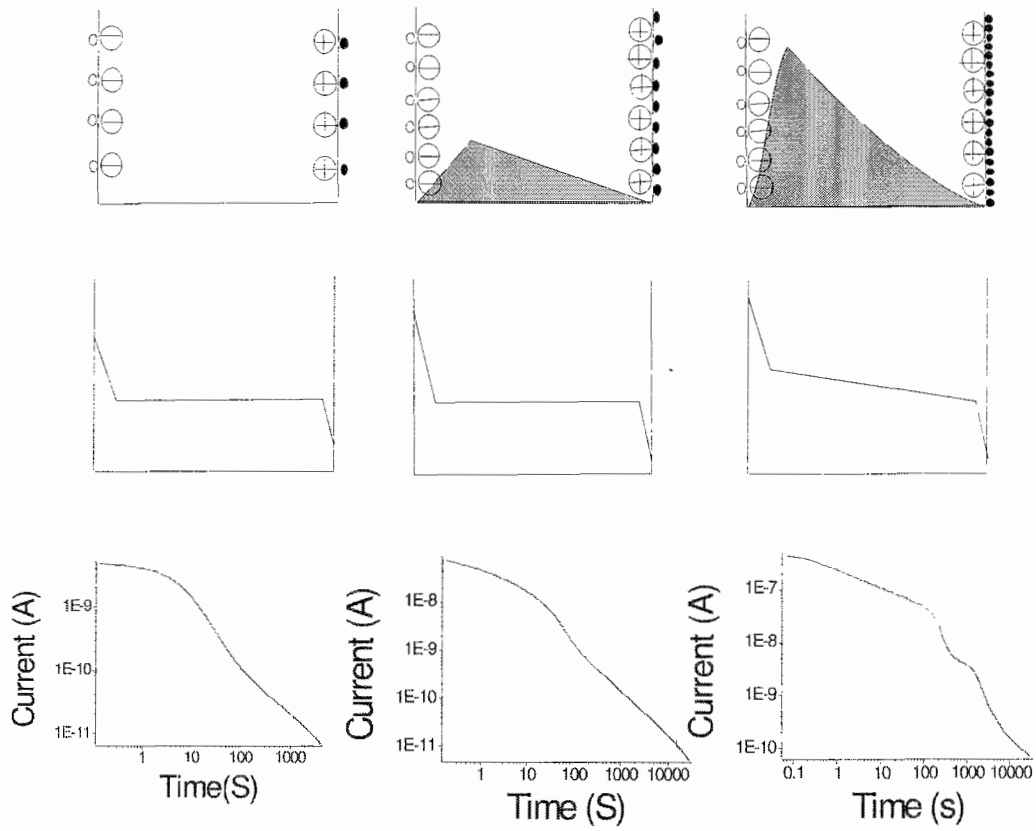

(a) (b) (c)

Figure 6.22 The charge (top), field distribution (middle), and short-circuit current with (a) low V_{app} 0<V<0.7V, (b) intermediate V_{app} between 0.7V to 1V, and (c) high V_{app} between 1V to 1.5V. In the graphs on the top, anion and cation are represented by negative and positive signs in the circles respectively. Electron is the black dots, and hole is light dots. Electronic carriers in the bulk are represented by the gray areas with triangle shape. The graphs depict the single carrier injection scenario because the energy line-up at the interface prefer the hole injection.

The total charge extracted from the integration of short-circuit decays increases even after the potential step current starts to decay situation. More charge does not necessarily lead to higher current. Recall that the decay after the maximum is attributed to the screening of the electric field. There is still some degree of screening at high V_{app}, only that it is much less than that at low V_{app}. The continuous reduction of electric field, although slight, cancels the expected current increase due to the greater number of injected electronic carriers.

It is also worth mentioning that there is clearly a shoulder at about 2000 seconds in the transient current under high V_{app}, as showed in figure 6.22 (c). It was concluded previously that the long-time regime in the I_{SC} is related to the discharge of electronic carriers in the bulk. The sudden change in the I_{SC} at this point is then related to the discharging of electronic carriers in the bulk. The shoulder is apparent at high V_{app} (1.5V) and long t_d (>300 seconds), as evidenced in figure 6.13 or the thicker samples (>667nm) as showed in figure 6.17. As observed in figure 6.18, thicker samples store more injected electronic carriers. Therefore, a common feature between these two situations is that a large amount of electronic carriers were stored in the bulk.

Analysis of the combined I_{SC} results convincingly establish the connection between the injected electronic carriers and the I_{SC} behaviors. In addition, it is found that there are strong correlations between the relaxation of electronic carriers on the electrode and short-time regime in the I_{SC}, and between the relaxation of electronic carriers in the bulk and long-time regime in I_{SC}. The amount of electronic carriers in the bulk determines the shapes of the I_{SC} in the following qualitative picture: When $n_e<n_{ion}$, the I_{SC} is typical of

double layer discharging. When n_e is comparable to n_{ion}, the I_{SC} exhibits a modest sign of the power law in short-time regime. When $n_e > n_{ion}$, short-time regime in the I_{SC} clearly follows a power law with index of 0.33. In addition, there is a shoulder present in long-time regime.

These results are in strong support of the electric field and carrier distributions laid out in step 1,2 and 3.

6.5 Conclusion

As discussed above, the direction connection between the timescales of the potential step transient current and electrode polarization of ionic carriers in the Au|P_A|Au sample architecture strongly argues that electronic charge injection is enhanced from the formation of a double layer at the interface. This double layer, which consists of ionic space charges in the polymer and electronic carries on the electrode, facilitates the electronic carrier injection by contributing a high electric field at the interface.

Results from potential step experiments and relaxation measurements under short circuit and open circuit configurations argue for a strong dependence of the carrier and electric field distributions on V_{app}. At low V_{app}(up to 0.7V), the electric field in the bulk is mostly determined by ionic carriers and therefore nearly zero due to the screening from ionic carriers. At V_{app}>0.7V, the electric field is jointly determined by both ionic and electronic carriers, and it is finite.

The connection between the amount of injected carriers and the relaxation behavior in

the short-circuit configuration was established with I_{SC} measurement results. In addition, a direct correlation was found between the relaxation of electronic carriers on the electrode and section 1 in the I_{SC}. At the same time, section 2 in the I_{SC} is related to the relaxation of electronic carriers in the bulk.

CHAPTER VII

LATERAL BARRIER HEIGHT INHOMOGENEITIES AT INP-POLY(PYRROLE) INTERFACES

7.1 Overview

The performance of metal-semiconductor (M-SC) or so-called Schottky contacts is of vital importance in several electronic applications. Specifically, M-SC contacts have been used as the gate electrodes in field-effect transistors, as drain and source contacts in MOSFETs and as photodetectors and solar cells. Although our ability to process complicated structures on semiconductors has advanced drastically over the years, in contrast, fundamental questions regarding barrier formation and charge transport at semiconductor interfaces still remain unanswered. The most discussed formation mechanisms of Schottky barriers (SBs) are those involving the presence of interface states such as metal-induced gap states[1,2] and defect-related states [3,4]. While these mechanisms assume lateral uniformity of the M-SC interface, unintended lateral heterogeneity on the length scale of the semiconductor depletion width W, has been gaining strength in explaining a range of common anomalies that have plagued the study of one-sided semiconductor interfaces [5,6,7]. Theoretical work on the unique physics of small-scale barrier inhomogeneities [8] and ballistic electron emission microscopy (BEEM) studies [9] are the primary supporting evidence for lateral heterogeneity. There has been comparatively little work, however, to directly investigate nanostructured interfaces to achieve a better understanding of barrier formation. The focus of this work is to introduce intentional lateral non-uniformities into M-SC interfaces in the hopes of

clarifying the ambiguities arising from anomalous behavior. It is hoped that this work could therefore solidify the link between anomalous behavior and small-scale barrier inhomogeneities.

In order to explore the role that barrier inhomogenity plays in semiconductor interfaces, a clear connection between inhomgenous physical structural and interfacial charge transport is needed. Thus, a good starting point is a relatively ideal semiconductor contact, as characterized in part by a quality factor close to unity (as discussed in more detail in section 8.2). Next, in order to relate the effects of barrier inhomogeneity to charge transport behaviors, it is important to be able to introduce nanoscale patterns in a controlled way, so that the size and shape of the patterns can be fully characterized. Finally, it is useful to introduce various barrier heights so that the extent to which barrier inhomogeneities affect charge transport can be studied systematically and thoroughly. With all these requirements in mind, an inorganic semiconductor-conjugated polymer interface (specifically the indium phosphide | poly(pyrrole) phosphomolybdate hybrid or InP-PMH interface) has been chosen as the platform for this project. As will be discussed below, the conjugated polymer-semiconductor interface is analogous to an ideal M-SC contact, with the added benefit of being able to readily tune the barrier height of the contact [10].

7.2 Theoretical Treatment of Barrier Formation and Charge Transport at M - SC Contacts

M-SC contacts (also referred to as Schottky contacts) exhibit rectifying behavior where current is exponentially dependent for one sign of the applied bias as shown in figure 7.1.

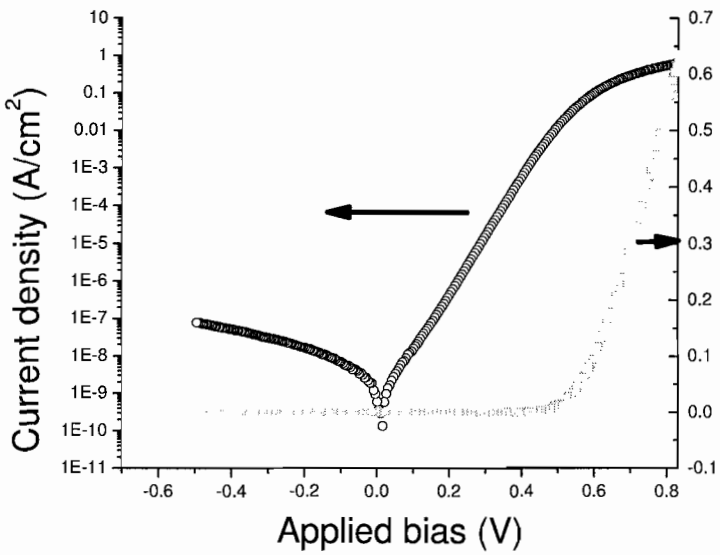

Figure 7.1 Characteristic dependence of current density (J) on applied bias (V_{app}) for a rectifying contact in logarithmic-linear scale (symbol) and linear-linear scale

This rectifying behavior occurs because of a space charge layer formed on the semiconductor side of the interface. The space charge layer is formed as the result of charge transport across the interface to bring two bulk materials with different Fermi levels to equilibrium, as shown in detail below in figure 7.2.

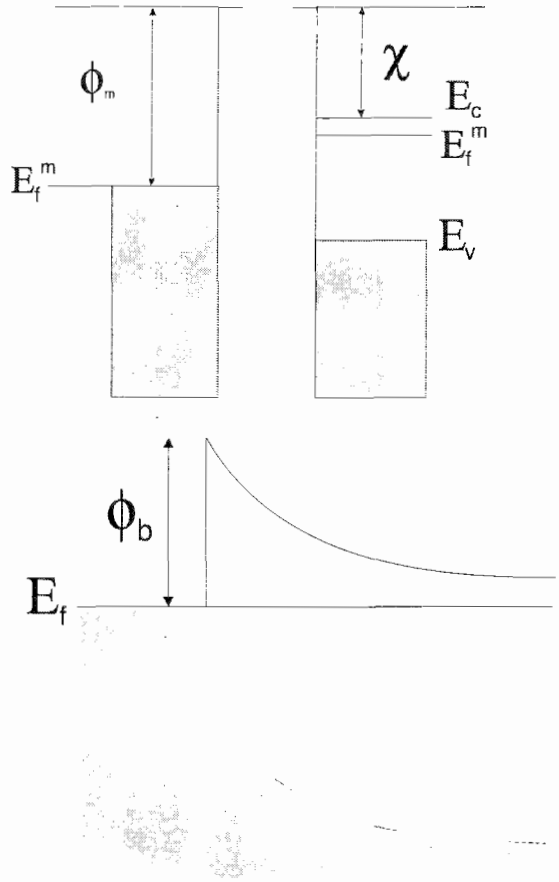

Figure 7.2 Formation of a barrier between an *n*-type inorganic semiconductor and a conductor, where E_v is the valence band energy, E_c is the conduction band energy, χ is the electron affinity, E_f^m is the Fermi level of each material before contact (top) and in perfect contact (bottom), where E_f is the equilibrium Fermi level of the contact, and ϕ_b is the barrier height at the interface.

The charge transfer between the two materials stops when the Fermi levels of contacting phases come into equilibrium, as shown in bottom graph in figure 7.2. By using the depletion approximation, it can be assumed that carrier density in the depletion region of the semiconductor is negligible, which leads to a uniform charge distribution. The electric field then increases linearly with distance from the edge of the depletion

region in accordance with Gauss's theorem (figure 7.3(b)) while the electrostatic potential increases quadratically (see figure 7.3(c)).

Figure 7.3 Variation of (a) charge density, ρ, (b) electric field $|\mathcal{E}|$ and (c) barrier height ϕ_b with distance x into an n-type semiconductor from the interface. X-axis is position.

By inspecting the band diagram in figure 7.2(b), the barrier height ϕ_b can be given by:

$$\Phi_b = \Phi_m - \chi \qquad \text{(eq. 7.1)}$$

where ϕ_m is the work function, and χ is the electron affinity of the metal (or more generally, the conductor). The barrier height is simply a measure of the energy needed for an electron to cross from the n-type semiconductor to the conductor. However, it must be noted that there are various ways electrons can be transported across the M-SC interface. Figure 7.4 shows different mechanisms of charge transport under forward bias. Usually thermionic emission (TE), where a sufficiently energetic charge carrier surmounts the interfacial potential barrier ϕ_b, is considered to be the dominate mechanism. However, for degenerately doped semiconductor interfaces, other mechanisms such as tunneling (field and thermionic field emission, FE or TFE in short)

also contribute to charge transport. These tunneling processes allow electrons with energies below the top of ϕ_b to penetrate the interface.

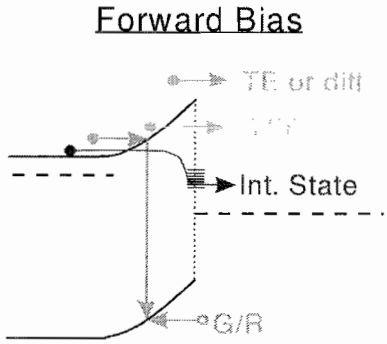

Figure 7.4 Competing charge transport mechanisms at an inorganic semiconductor | conductor interface, where TE: thermonic emission, TFE: thermonic field emission, G/R : generation and recombination and Int. State is interfacial states. The open circles represent holes, and the filled ones represent electrons.

From TE theory, the current-limiting process is the actual transfer of electrons across the interface between the semiconductor and the metal, where the current density J is expressed as:

$$J = J_0 \exp(\frac{qV_{app}}{kT})(1 - \exp(-\frac{qV_{app}}{kT})) \qquad \text{(eq. 7.2)}$$

where V_{app} is the applied voltage, T is the temperature in Kelvin, and J_0 is the equilibrium exchange current density, given by:

$$J_0 = \kappa A^* T^2 \exp(-\frac{q\Phi_b}{kT}) \qquad \text{(eq. 7.3)}$$

where A^* is the Richardson constant, and κ is the transmission coefficient for majority carriers at the interface. Experimentally observed M - SC forward-bias J-V_{app} curves are almost always semi-logarithmic, in agreement with TE theory. This is shown in more detail in figure 7.1. However, the slope of the $ln\ J$ vs. V_{app} plot - as characterized by the empirical quality factor, $n_{emp} = \frac{kT}{q}\frac{dV_{app}}{d\ln J}$, often deviates from the ideal prediction of n =1 as expected in TE. A value of n_{emp} greater than one is generally attributed to mechanisms such as imaging force lowering, interface states, generation and recombination and TFE, but there is often poor quantitative agreement between these models and experiment.

In general, deviations of n_{emp} from unity can occur from a voltage dependence of the barrier. For current transport governed by TE as given in equation 7.2 above, it is apparent that n_{emp} is related to the voltage dependence of ϕ_b through the following:

$$n_{emp}^{-1} = 1 - \partial\phi_b/\partial V_{app} \qquad \text{(eq. 7.4)}$$

This voltage dependence can arise for several reasons, one of which is an inhomogeneous barrier potential. Tung, Werner and Gutler, and others have discussed the effect of a inhomogenous barrier at the M - SC interface [2,7,7,9]. Details about the applied voltage dependence of barrier height will be discussed later (Section 7.6).

7.3 Previous Work on InP - PMH Interfaces

The rectifying InP - PMH interface provides an ideal platform for probing the fundamental questions that still remain about barrier formation and charge transport. Like M-SC interfaces, the InP - PMH interface is considered to be a one-sided inorganic semiconductor interface in that PMH does not support a space charge region. The interior of a doped conjugated polymer has no electric field because of perfect screening by mobile counter ions, which perform the same function as electrons in a metal. The mobility of these dopant counter ions is an important feature that makes the InP - PMH interface more analogous to a Schottky diode than for instance a pn junction. Another unique aspect of the InP - PMH interface is the ability to tune the barrier height of this interface by *in situ* electrochemical manipulation of the conjugated polymer PMH. Figure 7.5 shows a series of J-V_{app} curves collected for a single InP - PMH interface. Each curve corresponds to a different electrochemical potential μ_{PMH} (or Fermi level) of the PMH, as controlled by the electrochemical doping of the polymer while it remains in contact with the inorganic semiconductor. The shift in the J-V_{app} curves is due to changes in the Schottky barrier height ϕ_b as confirmed by capacitance-voltage measurements [10]. Figure.7.5 shows how the barrier height between the InP-PMH interfaces can be tuned electrochemically with a wide range, as demonstrated by the shift of the turn-on voltage of the current density-applied voltage curve.

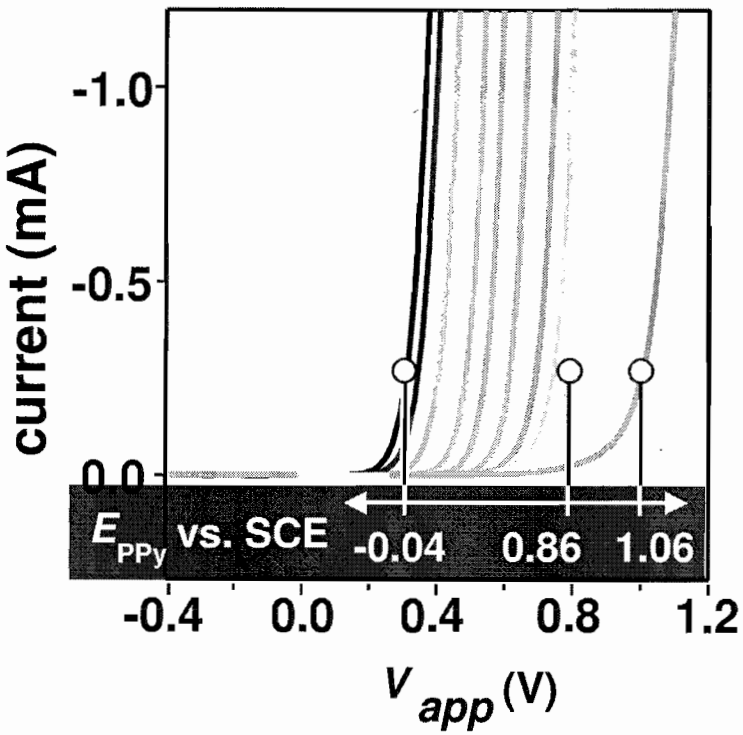

Figure 7.5 Current density – applied voltage (J-V_{app}) curves for an InP - PMH interface as a function of the electrochemical potential of the doped conjugated polymer PMH (μ_{PMH}). Ref. 10

Current transport at the InP - PMH interface has also been thoroughly investigated [12]. It was reported that the forward bias current density J was very close to that predicted by TE theory at room temperature, but deviated from it as temperature was reduced. To explain the excess current that is present at reduced temperatures, an inhomogenous barrier distribution was proposed as the potential mechanism. A Gaussian distribution of barrier heights was assumed as illustrated in figure 7.6.

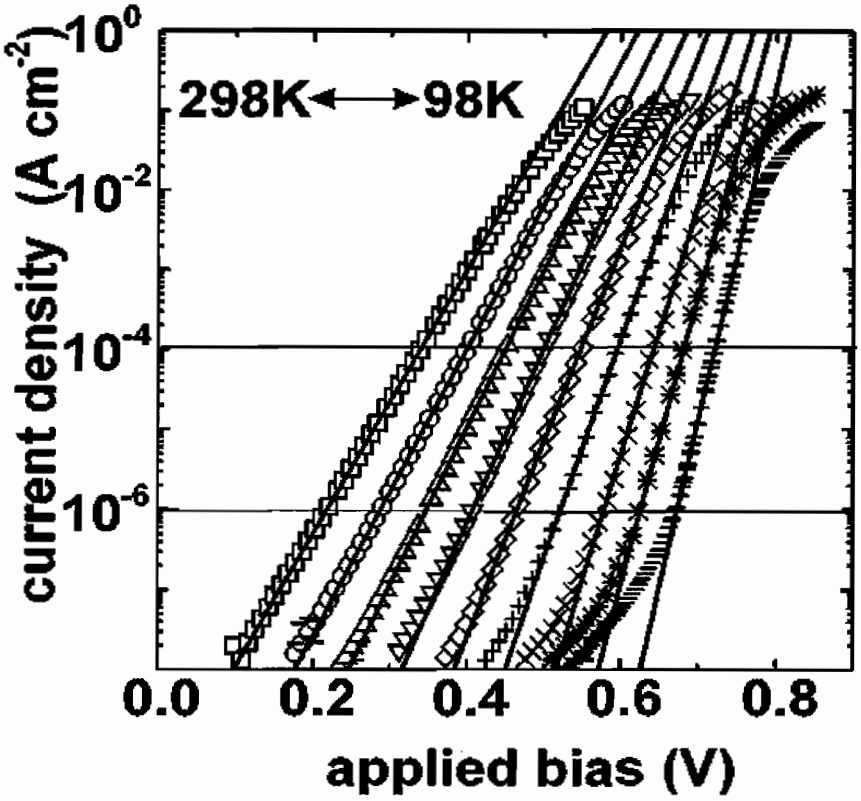

Figure 7.6 Temperature dependence of the current density (J) for an InP-PMH interface. Temperatures ranging from 98 to 298 K, stepped by 25K, are shown. The symbols represent experimental J-V_{app} data, while the temperature dependence of the J-V_{app} data is modeled using a Gaussian distribution of lower barrier regions (solid line). Ref. 12.

7.4 Parallel Conduction vs. "Pinched Off" Barrier Inhomogeneities

Ballistic electron microscopy (BEEM) studies show that most M-SC interfaces consist of a host of different structures due to multiple compound formation, polycrystalline defects, and other disorders. Traditionally, parallel conduction has been used to describe the charge transport of parallel contacts and the total current is assumed to be a linear combination of the TE current of each contact [13]. The barrier height characterizing the interface depends predominantly on the fraction of contact area covered by the lower barrier phase.

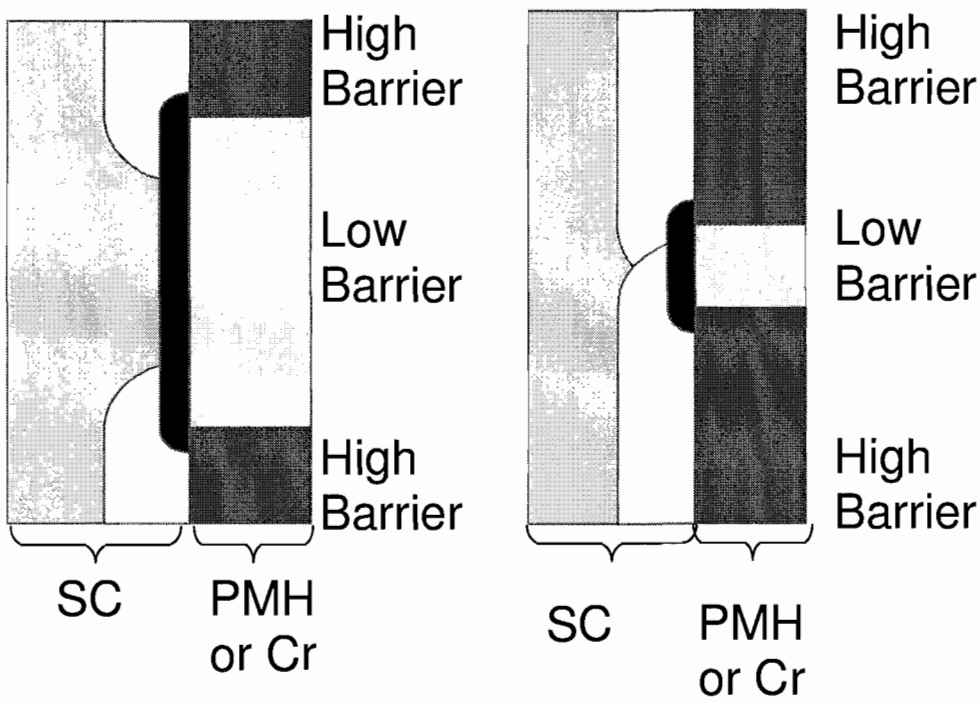

(a) (b)

Figure 7.7 (a) Parallel conduction (b) Pinch-off The light black area is the depletion region of low barrier contacts, and white area is depletion region of high barrier contacts.

The idea of parallel conduction can be illustrated in figure 7.7(a). The core assumption is that there is no interaction between neighboring contacts and the total current is the sum of the contribution of individual contacts of different barrier heights and contact resistances. It has been reported that the barrier height measured by forward bias J-V_{app} characteristics in the above situation depends not only on the fraction of the area of low-barrier contacts but also on the size of these contacts. Freeouf et al [14] demonstrated that for small interfacial "patches" characterized by a lower ϕ_b than the background and of size comparable to the depletion width (W) of the inorganic semiconductor, a so-called "potential pinch-off" would occur. This is illustrated in figure.7.7(b). Tung [8] further developed this idea to show that the anomalous behavior

of putatively uniform interfaces can be quantitatively explained using a nanometer-scale low-barrier contact distribution and an inhomogeneous barrier height pinch-off model. While these studies suggested that lateral inhomogenties of the interfacial barrier height may play a role in charge transport, more investigations are needed to show how to quantitatively relate them to experimental results, thus providing motivation for the work contained herein.

Therefore, the relatively ideal InP - PMH interface will be the starting platform used to introduce planned lower barrier regions in order to investigate the predictions of the barrier inhomogeneity model. Both the density and the size of these lower barrier regions will be varied, and the J-V_{app} and capacitance-voltage (C-V_{app}) characteristics of the interface will be studied. The InP-Cr contact is utilized as the low barrier contact, in contrast to the high barrier InP-PMH contact. In order to probe the pinch-off phenomena,

the feature size of the Cr pattern need to be comparable to nanoscale depletion width. Electron beam lithography is utilized to fabricate the nanoscale Cr pattern, which is the first step to producing the hybrid InP-Cr|PMH interfaces. The next section will provide detailed descriptions of experimental procedures. In the context of this chapter, the hybrid interfaces refer to the Schottky contacts with lateral structure inhomogenity formed by embedding the InP-Cr contacts between InP-PMH contacts.

7.5 Experimental procedures

Electron-beam lithography can be utilized to produce nano-scale patterns on semiconductor substrates. A scanning electron microscope (SEM) was outfitted with Nabity pattern generation system, so that the electron beam could be manipulated to write a computer generated pattern, as shown in figure 7.8.

In order to write a pattern on the InP substrate, a poly(methylmethacrylate) or PMMA film was first deposited onto the semiconductor surface by spin-coating. Substrates were then exposed to a well-controlled electron beam to write a pattern designed by CAD followed by a development step to remove the PMMA that was exposed. For some samples, plasma cleaning was also used to rid the sample of any residual PMMA in the exposed area. A Cr film of a controlled thickness was then deposited onto each substrate by thermal evaporation. Substrates were subsequently soaked in an acetone bath while undergoing sonication to lift off the unexposed PMMA. Patterns formed in this manner were then characterized by SEM. A more comprehensive description of this process can be found in the Appendix in reference 12.

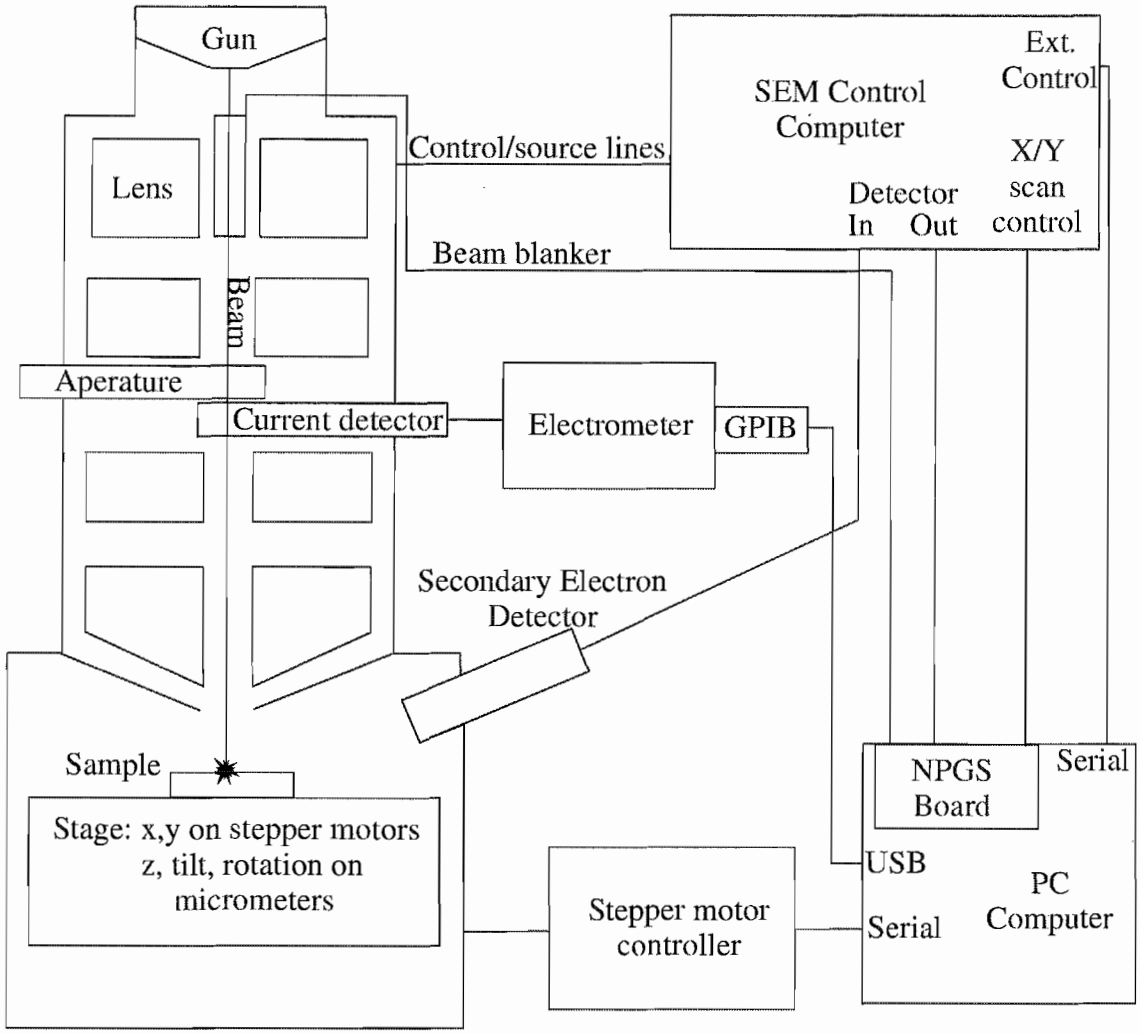

Figure 7.8 The schematic of the modified SEM system for the application of electron beam lithography. (in courtesy of F.E.Jones)

The hybrid InP-CrI PMH architecture is showed in figure 7.9. The experimental design of the InP - PMH interface involved a physical mask consisting of a glass cover slip between two layers of Tefzel™ film to control the contact area of the semiconductor. The mask was adhered to the semiconductor substrate by heating the assembly to a temperature above the melting point of the Tefzel™ film, approximately 250°C. Back ohmic contact to the inorganic semiconductor was made by scratching the InP with a

Ga/In eutectic contacted with a Sn-Cu wire coil. The wire coil contact was then mechanically stabilized with epoxy. PMH was synthesized by chemical oxidation of pyrrole by phosphomodlybdic adic hydrate and drop cast from solution into the area defined by the Tefzel™ mask. The reaction solution contained 0.165g phosphomolybdic acid hydrate,12.5uL of pyrrole and 0.55mL of tetrahydrofuran, following the procedure of Freund and coworkers[15].

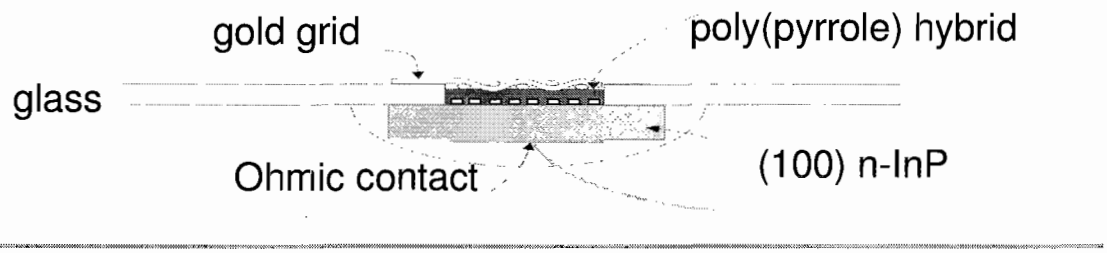

Figure 7.9 The schematic of the hybrid InP-Cr| PMH architecture, low barrier contacts formed by InP and metal interface are in parallel with high barrier contacts formed by the InP and PMH interface. Tiny rectangles represent cross sections of metal lines

A gold grid was positioned on top of the cast polymer film formed after the evaporation of the tetrahydrofuran, as shown in figure 7.9. More reaction solution was then deposited to embed the gold grid in the polymer. It should be noted that after casting, the PMH is insoluble to later casting drops, which prevents the gold grid from directly contacting the semiconductor substrate. After polymer casting, the interface was then rinsed gently in methanol to dissolve away any non-reacted pyrrole and phosphomolybdic acid hydrate. The gold grid was electrically contacted through a tail that extended off the surface of the InP. The interface was then loaded into a steel airtight

canister and evacuated (~0.30 mTorr) for subsequent current-voltage and capacitance-voltage characterization.

Temperature control over all of the interfaces studied realized with an EC10 environmental chamber by Sun electronics. J-V_{app} data was measured using a Keithley 236 Source Measure unit and collected with a custom Labview program. Capacitance-voltage (C-V_{app}) measurements were carried out with a Solatron 1260 impedance analyzer over a frequency range of 10 Hz to 1 MHz with a 10 mV waveform amplitude.

7.6 Experimental Results & Discussion

The InP-PMH and InP-Cr interfaces were each studied independently before they were utilized to make hybrid InP-Cr|PMH interfaces. It had previously been shown that the ideality factor, n_{emp}, of the InP-PMH interface is very close to unity at room temperature and that the barrier height of the interface can be "tuned" electrochemically [11]. In addition, as shown in figure 7.10, the difference in barrier height of the InP-PMH versus the InP-Cr interface is about 0.4eV, which is sufficient to provide the "pinch-off" effect as discussed above, rather than parallel conduction.

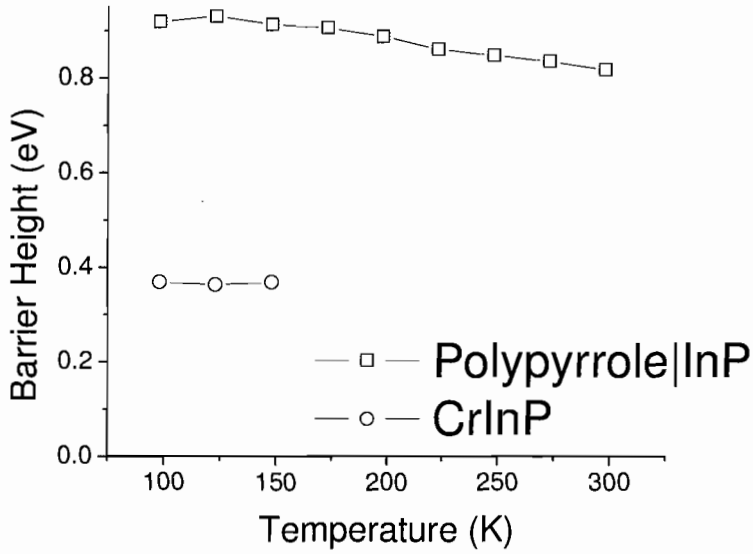

Figure 7.10 Comparison of the barrier height of InP - PMH and InP - Cr interfaces as the temperature is reduced.

To date, a substantial amount of work has been done to fabricate "ideal" InP-PMH interfaces and to tune the modified SEM to function as an electron beam lithography system. The latter involved much trial and error to find a good electron beam dosage, as well as problems with stage correction, and focal plane function fitting. Furthermore, several control experiments concerning the effects of SEM probe current and dosage on line width were designed and tested. The effects of each processing step on both the *J-Vapp* and $C\text{-}V_{app}$ characteristics of the interfaces were also thoroughly investigated. These control experiments were very important because many steps in the pattern-making process can potentially modify the surface of semiconductor and introduce complex consequences into both the measurement process and data analysis. It was found that the most dramatic surface modification in the experimentation process was caused by plasma cleaning. Samples made from InP chips that were exposed to oxygen plasma for 30s to

clean the surface were found to pass substantially more current and possessed substantially lower barrier heights than control samples that were not processed with the plasma cleaning, as shown in figure 7.11:

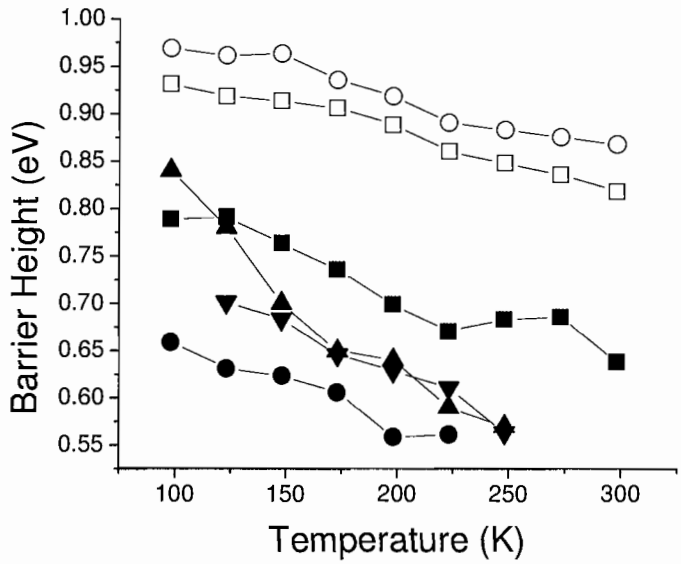

Figure 7.11 The effect of plasma cleaning on the barrier height of InP-PMH interfaces. The open symbols represent interfaces where the surface of the SC was not plasma cleaned, while filled symbols represent interfaces that were plasma cleaned prior to polymer deposition. All barrier height measurements were done using capacitance-voltage measurements.

After the InP-PMH and InP-Cr interfaces were characterized independently, metal patterns of different sizes and shapes were fabricated onto the InP surface with electron beam lithography to explore the size effects of low-barrier contacts. Although the metal patterns varied in size and shape, the total coverage of metal onto the semiconductor substrate was kept near constant. Patterns were imaged by SEM before the polymer

solution was deposited on top of the Cr patterned InP. A few representative images are shown below in figure 7.12.

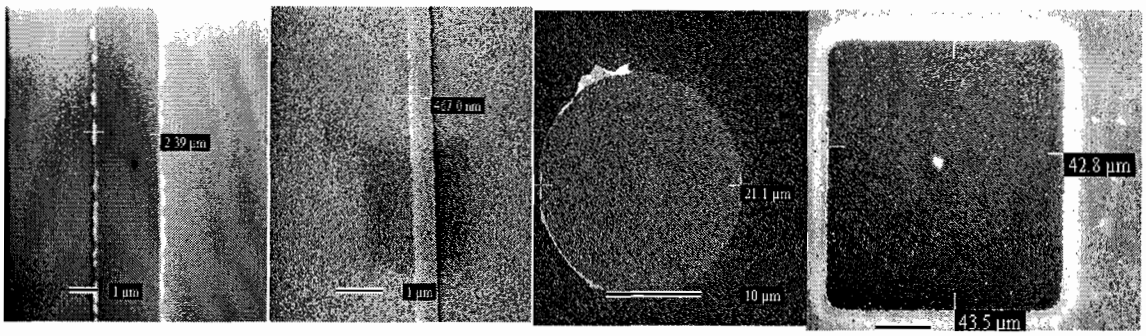

(a) (b) (c) (d)

Figure 7.12 Patterns of various shapes and sizes fabricated onto InP substrates using electron beam lithography. In (a) the linewidth 2.39um, in (b) the line width 467nm, in (c) circles with diameter 21.1um while in (d) squares with 43um in side length, the total areas of the semiconductor surface covered by arrays of these patterns were kept the same.

Although the total area of Cr coverage was kept constant, several anomalies were noted as the size of the pattern was reduced. As shown below in figure 7.13 and 7.14, a hybrid interfaces with square 40um Cr patches, and hybrid interfaces with 500nm Cr lines passed more current than the hybrid interfaces with 50nm Cr lines, in spite of the constant area. Furthermore, when compared with a control interface (InP-PMH), the hybrid interfaces with 50nm Cr line passed more current. The control sample was processed in the same way as the patterned samples other than electron beam exposure. These results indicate that InP-Cr contacts of a smaller scale than the depletion width of the InP-PMH showed observable signs of pinch-off and that the overall barrier height of the entire interface is increased due to the interaction with neighboring InP-PMH regions.

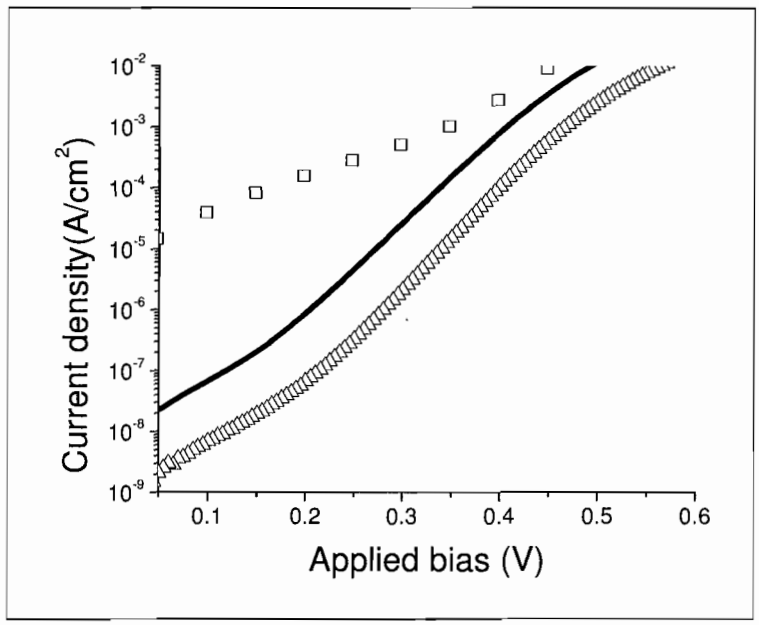

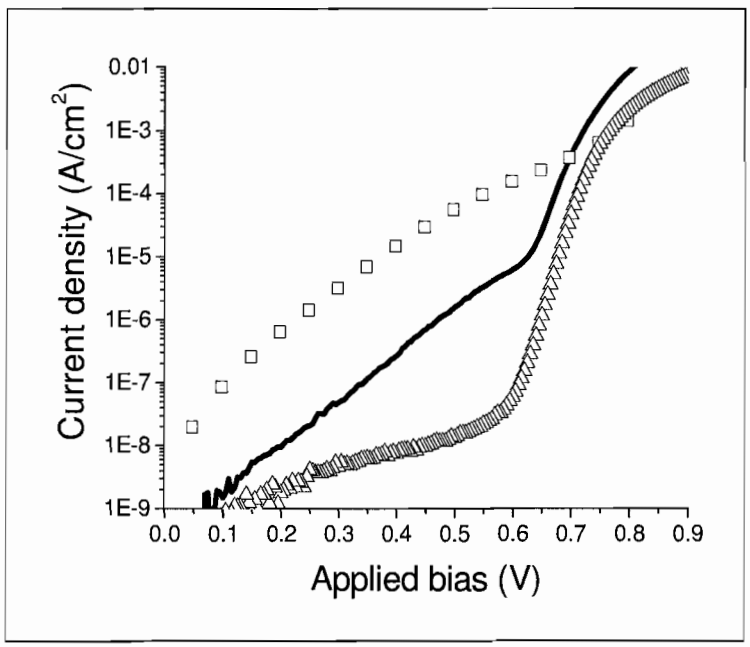

Figure 7.13 Size effects of patterned samples of various line width at room temperature (top) and at reduced temperature of 198K (bottom). Results are from a sample with 500nm Cr line (□), a sample with 50 nm lines (solid line), and a uniform InP-PMH contact (△).

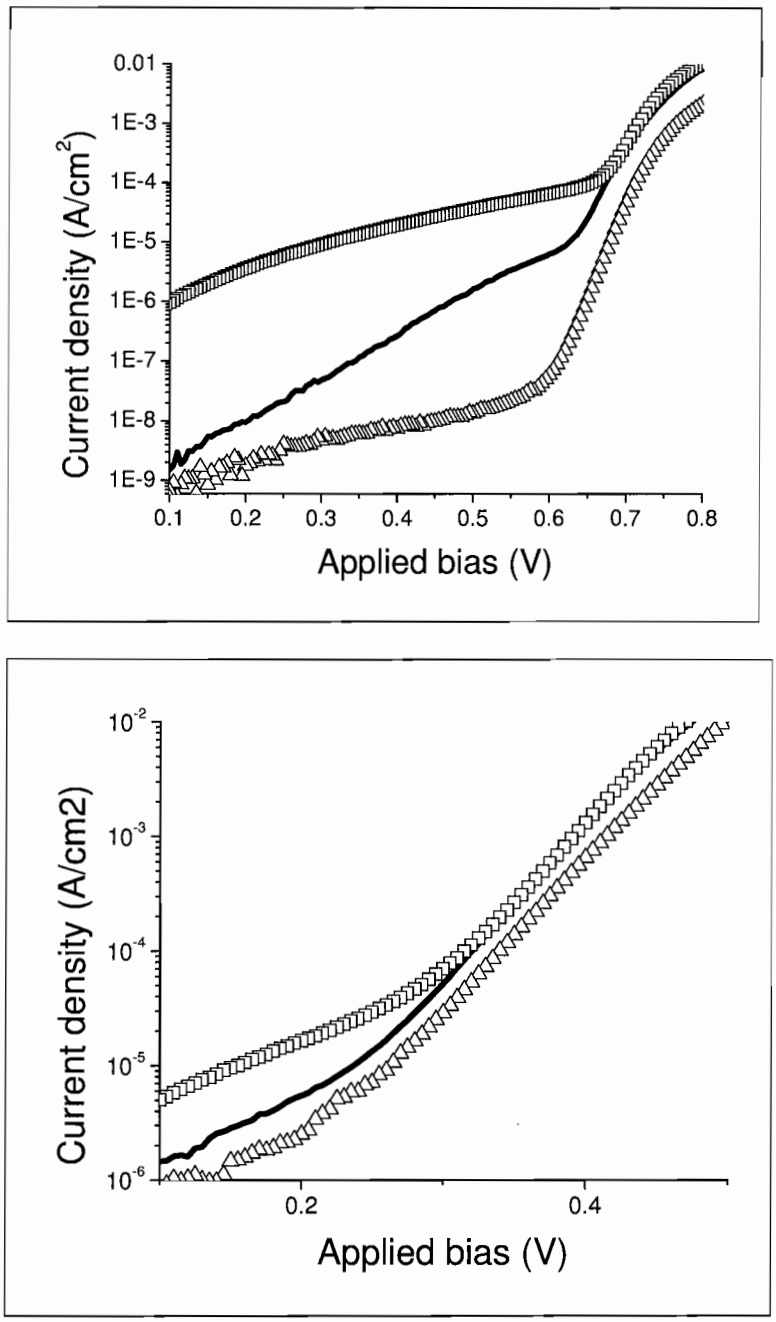

Figure 7.14 Interfaces exhibiting "pinch-off" effects at room temperature (top), and a reduced temperature of 198 K (bottom). Results from an interface patterned with 40um square metal patches (□), an interface patterned with 50 nm lines (solid line), and uniform InP-PMH interface.

The J-V_{app} measurements on samples with metal patterns of various sizes showed that the neighboring high barrier contacts exert some influence on the low barrier contacts of when the width is about 50nm. Considering that the depletion width of specific InP-PMH interfaces under studies is about 200nm, the clear message from these experiments is that low barrier contacts shows signs of pinch-off when their sizes are much smaller than the depletion width of their neighboring high barrier contacts. This agrees with the diagram in figure. 7.7. These convincing results point to a connection between the pinch-off phenomena and size of the metal lines, more experiments and analysis are needed in order to understand the physics behind this relationship.

For this purpose, several interfaces were fabricated with InP substrates covered by Cr lines of approximately 30 to 70nm in width followed by a layer of PMH. All of them show the following features:

1. The forward-bias current can be separated into three sections: a low bias region with a low slope (corresponding to $n_{emp} \sim 1.00$), followed by an intermediate bias region characterized by a high slope ($n_{emp} > 2.00$) and finally a high bias region exhibiting the influence of series resistance, as illustrated in figure 7.15.

2. The low bias region is barely present at 298K and gradually becomes more and more prominent as the temperature is lowered.

3. The transition from the low slope region to the high slope region appears at approximately the same current at all temperatures.

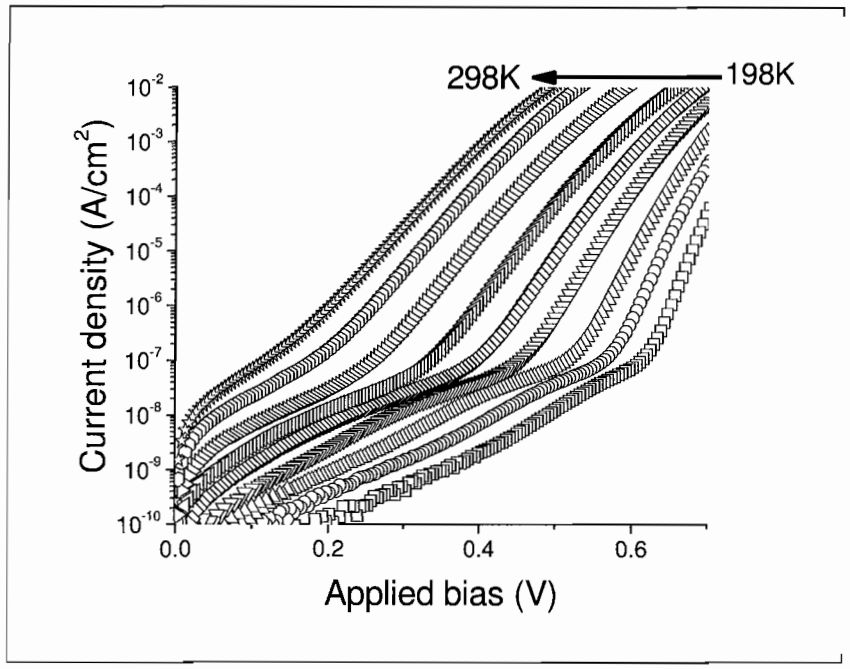

Figure 7.15 Current density-applied voltage (J-V_{app}) characteristics of a representative hybrid InP-Cr|PMH interface exhibiting a low slope, a high slope, and a series-resistance dominated region as a function of decreasing temperature (K)

It is also noticeable that the low bias region is completely absent in the control samples (without the metal patterning), and is therefore connected to the introduction of the patterned metal lines. The quality factors extracted from both the low bias and high bias sections are shown below in Figure 7.16 top and bottom graphs, respectively.

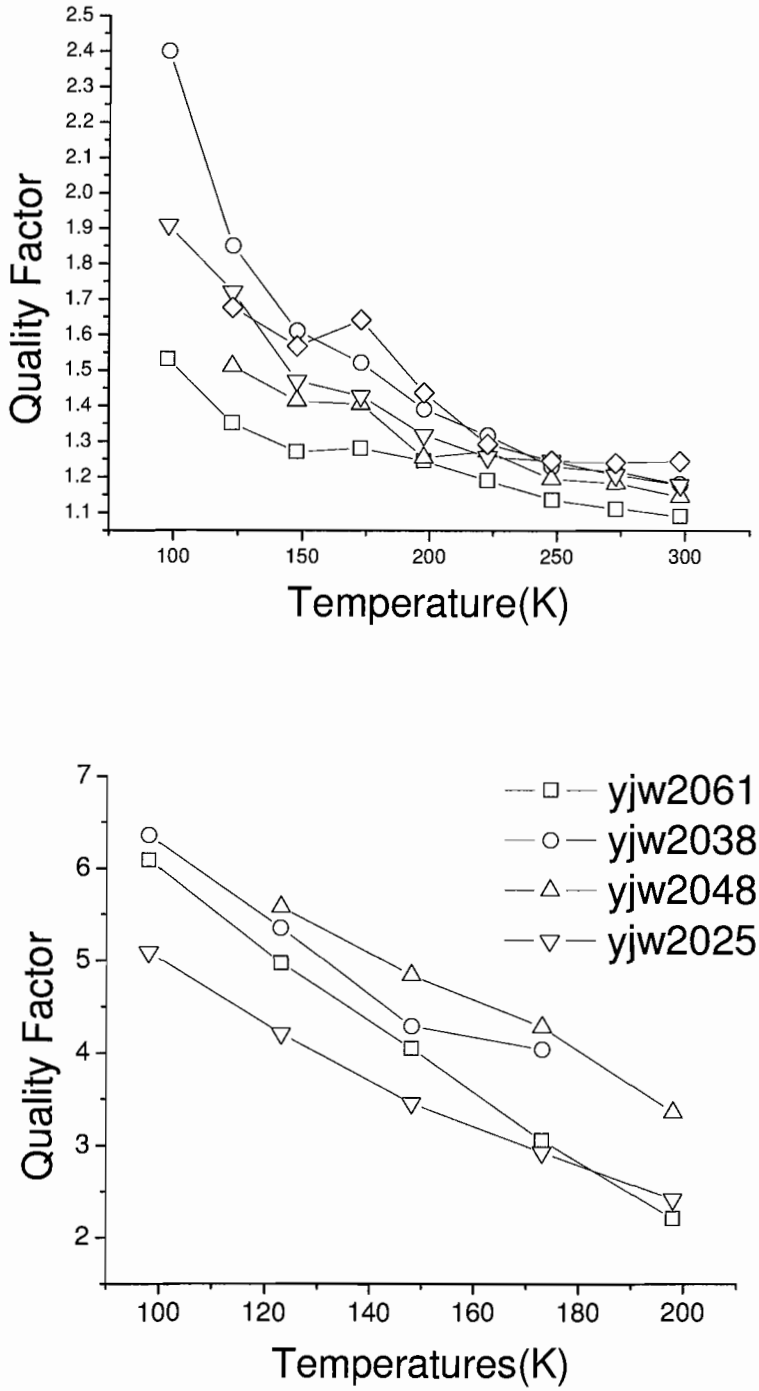

Figure 7.16 Quality factors extracted from both low bias and (top) and high bias (bottom) regions of the J-V_{app} data

As discussed above, pinch-off is observed in the hybrid Schottky contacts with lateral barrier inhomogenties created intentionally by fabricating low barrier contacts in parallel with high barrier contacts. The effects of these lateral barrier inhomogeneties can be elucidated using Tung's model[7,8]. The model implies that the barrier height of the lower barrier patch increases when the size is close to, or even less than, the depletion width of the M-SC interface. This phenomenon is referred to as pinch-off, and is used to explain many experimental anomalies in the experimental results of M-SC interfaces. Using the experimental data detailed above, simulations were done to examine the contribution of patch size and applied voltage to the pinch-off effect. The parameters used in these simulations were specific to the particular system studied.

Figure 7.17 describes the potential profile at the center of low barrier contact where the origin represents the M-SC interface, and increasing x is penetrating deeper into the SC. The effective barrier height of low barrier patch exhibits a strong size dependence. With line width as large as 300nm, the effective barrier height is equivalent to the interfacial barrier potential, and the influence from neighboring areas can be ignored. As the line width of the pattern is reduced, the effective barrier starts to shift into the semiconductor, even as the interfacial barrier potential remains the same. Pinch-off refers to the situation where the effective barrier height surpasses that of the interfacial barrier potential. In summary, the interaction between the low barrier contacts and their surroundings produces an increase in the barrier height when the feature size of the contact is comparable to the depletion width of the semiconductor.

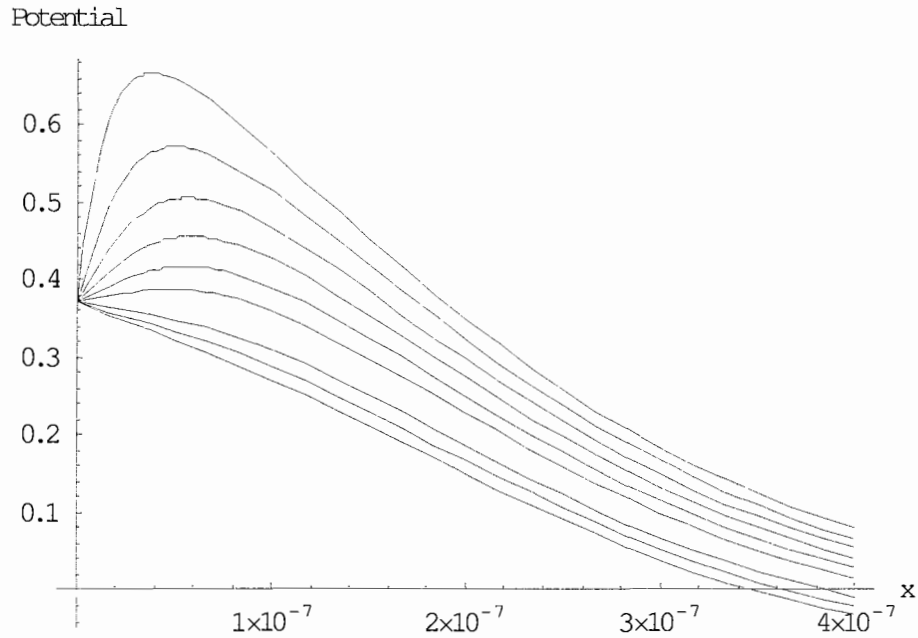

Figure 7.17 Barrier height as a function of distance into the inorganic semiconductor given for various pattern sizes. Feature sizes range from 30 to 270 nm (from bottom to top, respectively, with step 30nm).

The applied voltage can also affect the potential profile, as shown in figure 7.18. The feature size of the lower barrier contact is selected to be 30nm, which is much less than the depletion width of the InP semiconductor substrate. The applied voltages shown are -0.5V, 0V and 0.5V respectively. By inspecting the graph, it is apparent that the effective barrier height at 0.5V increases when compared with that at zero voltage. As discussed in section 7.2, the dependence of barrier height on applied voltage is the most common reason for $n_{emp} > 1.00$, as n_{emp} can also be written as $1 + \frac{d\Phi_b}{dV}$. Therefore based on Tung's model, the deviation from ideal TE theory is directly related to the lateral inhomogenties.

At the applied voltage of -0.5V, the effective barrier height is depressed compared with that at 0V, which contributes to the current increase with the reverse bias. This

leakage current degrades the interface properties in such a way that the ON-OFF contrast of the Schottky diode is deteriorated.

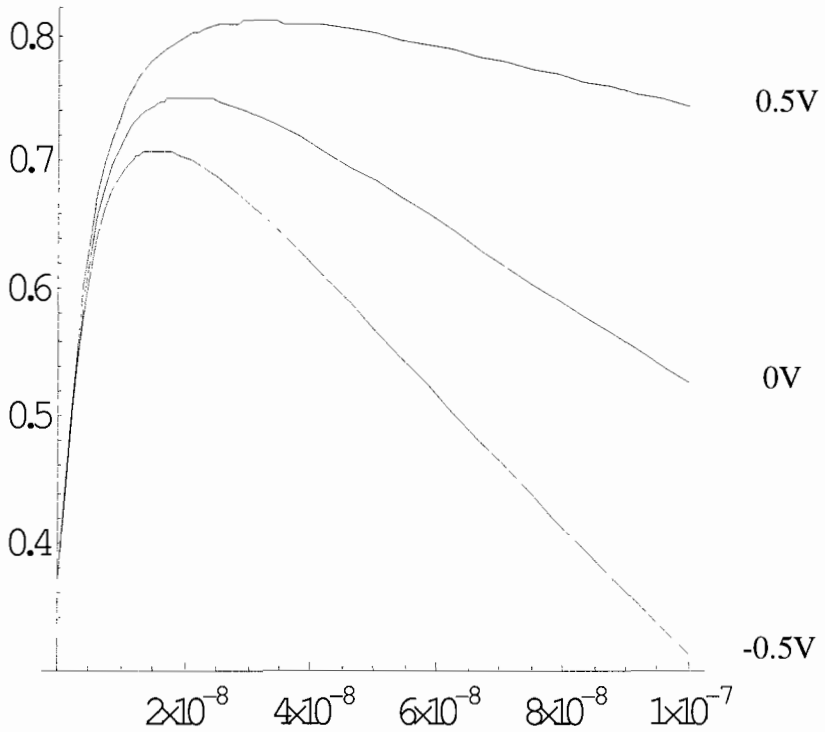

Figure 7.18 The effect of applied voltage on the barrier height of the interface, for V_{app} at -0.5, 0, and +0.5 V.

The barrier profile calculated from the simulations was then applied to the TE charge transport equation to calculate the current density. The J-V_{app} relationships of other interfaces, such as InP-Cr and InP-PMH are also calculated. The results are summarized in figure 7.19.

Figure 7.19 shows that the experimental results are clearly different from both the predictions of the parallel conduction model and the barrier inhomogeneity model. In the

high bias region, the experimental results were very close to the calculated current passing through the InP-PMH interface. Interestingly, the point at which the two respective currents cross each other is also the point where the transition from the low bias region to the high bias region occurs. To explain this phenomenon, a scenario combining both parallel conduction and an inhomogeneous barrier potential is proposed. As was stated earlier, Hybrid InP-Cr|PMH contacts show obvious signs of pinch-off when compared to uniform InP-Cr contacts. For these hybrid interfaces, the current in the low bias region is attributed to the pinched-off InP-Cr lower barrier contacts, while the current in the high bias region is dominated by the charge transport through the InP-PMH part of the contact. Charge transport across the InP-Cr contact deviates considerably from the ideal TE prediction due to the pinch-off effect. It should be noted that the barrier height of these contacts is still much lower than that of the InP-PMH regions even after the increases due to the influence from neighboring high barrier areas is accounted for. Therefore, most of the current is flowing through the lower barrier InP-Cr regions. The fraction of current flowing from the InP-PMH regions becomes more and more as the bias is increased. Finally, a point is reached where there is more current flowing through the InP-PMH regions than through the InP-Cr regions, and the transition between the two regions becomes apparent.

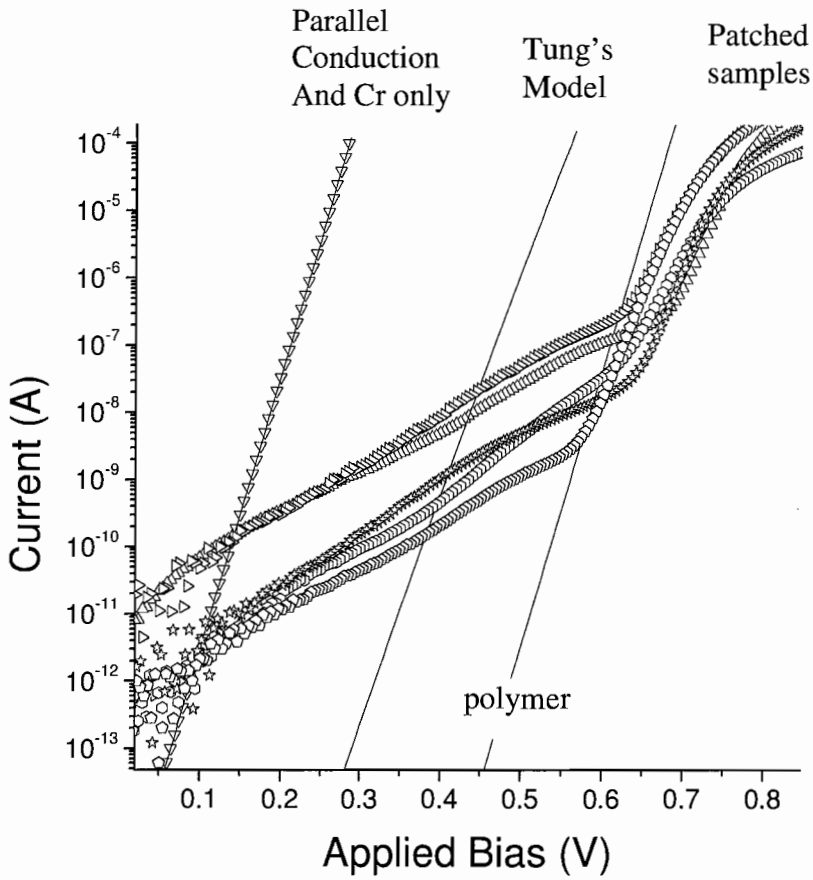

Figure 7.19 Comparisons of current-voltage relationship in hybrid interfaces with that of simulated results based on parallel conduction, Tung's model, and ideal thermonic emission of uniform interfaces respectively. Experimental results from patterned samples are represented by empty symbols. Simulated results by modeling pinch-off with Tung's model and uniform InP-PMH interfaces are represented with lines. Simulated results from parallel conduction (non-interaction hybrid interfaces) and uniform InP-Cr are identical and showed in empty triangles and lines respectively.

7.7 Conclusions

Experiments with hybrid interfaces of various feature size show that samples with about 50nm wide metal lines conduct more current than those without metal pattern, but less current than samples with larger size metal patterns of the same area, such as 500nm lines or 40um square. This indicates that the charge transport at low barrier contacts is affected when their sizes are less than the depletion width of the parallel high barrier contact (200 nm for the InP-PMH interface). In addition, the quality factor of the hybrid contact increases significantly and the degree of increase is related to the applied voltage. At the room temperature, the quality factor is about 3 at low voltages (<0.8V) and 1.2 at high voltages (>0.8V), and goes up dramatically in both cases when the temperature is lowered. Simulations were performed based on three models: 1) ideal thermonic emission at uniform interfaces, 2) parallel conduction and 3) Tung's model with consideration of the influence of lateral barrier inhomogenity. Comparisons between experimental results and simulations suggest that the charge transport at the hybrid InP-Cr|PMH contact were understood by separating the current-voltage relationship into two regions. In the low applied voltage region (V<0.8V), the charge transport across nanoscale InP-Cr interfaces contributes to the majority of the current. However, the fact that the current is much lower than what we expect for the standalone InP-Cr interfaces implies that charge transport across the InP-Cr contacts in the hybrid interfaces is affected by the InP-PMH interfaces. In the high voltage region, charge transport across the hybrid interfaces is largely dominated by the InP-PMH interface.

7.8 Future Work

More work is needed to explain some puzzling results in the current-voltage characteristics of the patterned samples, such as the apparent two-slope current-voltage relationship and high quality factors. In order to validate the proposed mechanism concluded from the comparisons between the experiments and simulations, systematic investigations of hybrid interfaces with a range of area ratio between the metal–InP contact and the InP-PMH are necessary. Through this, a solid correlation between coverage of metal pattern and the electrical properties can be established. More work is needed to correlate the size and geometry of the written patterns to the electrical properties of the hybrid interfaces. Further work will also include the electrochemical doping of the PMH to study the effect of electrochemical potential and on the barrier height of the hybrid interface. Indeed, the manipulation of μ_{PMH} should be a systematic and direct way to study the effects of neighboring high-barrier contacts to low-barrier contacts. It should be noted that values of n_{emp} of about 5 or 6 seen at reduced temperatures and low bias are not predicted by Tung's model, or any other charge transport mechanism, and this phenomenon needs to be more thoroughly explored.

CHAPTER VIII

CONCLUSIONS AND FUTURE DIRECTIONS

Conclusions

The mixed ionic-electronic conductors (MIECs) support both types of current (ionic and electronic) and present an interesting group of materials in term of fundamental physics, as well as applications. The heart of the fundamental understanding of MIECs involves the interactions between the ionic and electronic carriers. The MIECs field has benefited from many works formulating and investigating their transport properties. While the existing works have provided important insight into the understanding of some MIECs, basic questions such as the role of ionic carriers in electronic carrier transport, remain unanswered. This lack of understanding stems from the complexity of MIECs on one hand and the shortage of systemic electrical characterizations on the other. In order to examine the interaction of ionic and electronic carriers, especially effects of ion dynamics on the electrical properties of MIECs, electrical characteristics of ionically functionalized polyacetylene are investigated with broad measurement techniques in frequency domain and time domain respectively.

Impedance measurements in temperatures from 308 to 398K in Chapter III revealed three major dielectric relaxation processes, which were assigned to the geometric capacitance charging, ion hopping and electrode polarization respectively through equivalent circuit analysis. A wealth information concerning ionic carriers such as characteristic frequency of electrode polarization, ionic DC conductivity, activation energy, effective ion concentration, and hopping frequency, were obtained through

analyzing those dielectric relaxation processes in framework of ion hopping and electrode polarization.

Assignments of dielectric relaxation processes in the temperatures from 308K to 398K were validated by impedance measurements of electronic carriers introduced by applying a DC voltage (V_{app}) at room temperature in Chapter IV. The impedance measurements were executed at temperatures sufficiently low (from 173K to 233K) so that the ionic carriers are immobile. Using the same methods described in Chapter III, characteristic frequency of electrode polarization and activation energy of electronic carriers were obtained. These experiments supported the assignments of active carriers to be ions at temperatures from 308K to 398K when V_{app}=0. Forward and reverse DC voltage (V_{DC}) were also applied along with small amplitude AC signal to probe their effects on dielectric responses. It was found that the double layer capacitance increased with forward V_{DC} up to 0.7V, then decreased significantly with higher V_{DC}, while that with reverse bias only showed modest dependence on V_{DC}.

The influence of ion dynamic on electrical properties was probed by impedance analysis under the influence of DC voltage (V_{DC}) in temperatures from 308K to 348K in Chapter V. At 308K and V_{DC} higher than 0.3V, an upturn in AC conductivity was observed once the frequency was lower than the characteristic frequencies of electrode polarization (ω_{EL}). Clearly the AC conductivity enhancement happened only when the ion motion was fast enough to accommodate the change rate of the probing electric field. This supported for the argument that the charge injection was controlled by the

redistribution of ions. The low frequency capacitance appeared to increase with V_{DC} until it is 0.3V, then decrease dramatically to the point that it was negative with V_{DC} of 0.5V. These results, especially the negative capacitance, were related to delay of current rise-up relative to the applied voltage (V_{app}) in the time domain, which is confirmed by the simulations with Fourier transform.

Electrical measurements of anionically functionalized polyacetylene executed in Chapter VI included potential step experiments, relaxation through short- or open-circuit configuration, fast current-voltage scans. Two major accomplishments were achieved in this chapter. Firstly the direct connection between the electronic carrier injection and ion redistribution was established by the potential step measurement at temperatures 298K, 313K and 328K. It was showed that the onset time of current rise matches the timescale of the electrode polarization reported in Chapter III very well. Secondly the information about charge and electric field distribution was derived from the comprehensive electric measurements.

Results from potential step current experiments implied that incomplete electric field screening under higher DC voltage was contributing to decay of the current after the maximum. The incomplete screening suggested an electric field in the bulk supported by electronic carriers. This argument was confirmed by a number of observations in relaxations through short- or open circuit. Confirmation of a nonzero electric field in the bulk came from the initial open circuit voltage (V_{OC}), which is about the same with the potential step (V_{app}) up to 0.5V and then saturated. In addition, the density of electronic carriers obtained from short circuit measurement exceeded that of effective ionic carriers,

implying incomplete screening and electric field within the polymer due to the significant presence of electronic carriers in the bulk. Connection between the amount of injected carriers and the relaxation behaviors in short circuit configuration was also established with short circuit current measurement results.

Future directions

The conclusions from experimental results in Chapter VI can be greatly strengthened by the theoretical simulations, which involve solving the group of equations consisting continuity equation, Passion equation and current density in the presence of both electronic and ionic carriers. Theoretical simulations, nonetheless complex, could provide quantitative information about the carrier and electric field distribution, and greatly deepen our understandings of electrical properties of Au|P_A|Au.

Electrical measurements on anionically functionalized polyacetylene sandwiched between two metal electrodes (Au|P_A|Au) offered many insights to the role of ionic carriers on electronic carriers in this system. Experiments on sandwiched structures with cationically functionalized polyacetylene (P_C) or blend of poly(ethylene oxide) (PEO) and P_A (P_{APEO}) as active layers were also performed in order to further explore effects of ions on the electronic carrier injection and generalize the observations in this work. Preliminary measurements showed that behaviors of Au|P_C|Au and Au|P_{APEO}|Au structures were similar to these of Au|P_A|Au structures, which indicated that major conclusions from this work can be generalized. At the same time, more experiments

Au|P_C|Au and Au|P_{APEO}|Au are needed to solidify this generalization.

BIBLOGRAPHY

Chapter I

1. R. Benz, Z. Phys. Chem. **95**, 25 (1975).

2. A. Roos, A. F. Aalders, J. Schoonman, A. Arts, H. W. Wijn, Solid State Ionics, **9/10**, 571 (1983).

3. J. A. Archer, A. V. Chadwick, I. R. Jack, and B. Zeqiri, Solid State Ionics, **9/10**, 505 (1983).

4. M. Goldman and L. Shen, Phys. Rev. **144**, 321 (1966).

5. T. Kudo and H. Obayashi, J. Electrochem. Soc. **123**, 415 (1976).

6. P. Duwez, F. H. Brown, and F. Odell, J. Electrochem. Soc. **98**, 356 (1951).

7. F. H. Etsell and S. N. Flengas, Chem.Rev. **70**, 739 (1970).

8. E. C. Subbarao, P. H. Sutter, and J. Hrizo, J. Am. Ceram. Soc. **48**, 443 (1965).

9. J. Kincs and S. W. Martin, Phys. Rev. Lett. **76**, 70 (1996).

10. P. Maass, A. Bunde, and M. D. Ingram, Phys. Rev. Lett. **68**, 3064 (1992).

11. D. J. Vischjager, P. J. van der Put, J. Schram, and J. Schoonman, Solid State Ionics, **27**, 199 (1988).

12. I. D. Brown, Solid State Ionics, **31**, 203, (1988)

13. T. Ishihara, H. Matsuda, and Y. Takita, J. Am. Chem. Soc. **116**, 3801, (1994).

14. S. Seki, J. Phys. Chem. B **109**, 3886 (2005).

15. J. M. Tarascon and M. Armand, Nature **414**, 359 (2001).

16. C. O. Park, S. A. Akbar, W. Weppner. Journal of Materials Science **38**, 4639 (2003).

17. C. Wagner, Z. Phys. Chem. B **21**, 25 (1933).

18. C. Wagner, Naturwissenschaften **31**, 265 (1943).

19. J. W. Patterson, J. Electrochem. Soc. **118**, 1033 (1971).

20. N. S. Choudhury and J. W. Patterson, J. Electrochem. Soc. **117**, 1384 (1970).

21. N. S. Choudhury, J. W. Patterson, J. Electrochem. Soc. **118**, 1398 (1971).

22. G. C. Farrington and J. L. Briant, Science **204**, 1371 (1979).

23. Q. Pei, G. Yu, C. Zhang, Y. Yang, and A. J. Heeger, Science, **269**, 1086 (1995).

24. D. L. Smith, J. Appl. Phys. **81**, 2869 (1997).

25. I. Riess and D. Cahen, J. Appl. Phys. **82**, 3147 (1997).

26. J. C. deMello, N. Tessler, S. C. Graham, and R. H. Friend, Phys. Rev. B **57**, 12951 (1998).

27. J. Gao, A. J. Heeger, I. H. Campbell, and D. L. Smith, Phys. Rev. B **59**, R2482 (1999).

28. D. J. Dick, A. J. Heeger, Y. Yang, and Q. Pei, Adv. Mater. **8**, 985 (1996).

29. M. C. Lonergan, Annu. Rev. Phys. Chem. **55** 257 (2004).

30. H. W. Cheng, F. D. Lin, and M. C. Lonergan, J. Phys. Chem. B **109**, 10168 (2005).

31. H. W. Cheng and M. C. Lonergan, J. Am. Chem. Soc. **126**, 10536 (2004).

32. W. Schottky, Z. Physik **113** 367 (1939).

33. N. F. Mott, Proc. Roy. Soc. **171**, 27 (1939).

34. E. H. Rhoderick, Metal-semiconductor contacts, Clarenodon Press-Oxford 1980.

35. S. M. Sze, Physics of semiconductor devices John Wiley & Sons, New York.

36. S. M. Sze, C. R. Crowell, and D. Kahng, J. Appl. Phys. **35**, 2534 (1969).

37. R. H. Fowler, Phys. Rev. **38**, 45 (1931).

38. I. Reiss, J. Phys. Chem. Solids **47**,129 (1986).

39. I. Reiss, Phys. Rev. B **35** 5740 (1987).

40. H. Nafe, J. Electrochem. Soc. **144** 3922 (1997).

41. C. C. Liang, J. Electrochem. Soc. **120**, 1289 (1973).

42. M. S. Whittingham, R. A. Huggins, J. Chem. Phys. **54**, 414 (1971).

43. C. E. Rice and J. L. Jackel, J. Solid State Chem. **41**, 308 (1982).

44. J. L. Fourquet and M. F Renou, Solid State Ionics, **9/10**, 1011 (1983).

45. Z. P. Shao and S. M. Haile Nature **431**, 170 (2004).

46. T. Hibino, A. Hashimoto, T. Inoue, J. Tokuno, S. Yoshida, and M. Sano, Science **288**, 2031 (2000).

47. B. A. Boukamp, G. C. Lesh, R. A. Huggins, J. Electrochem. Soc. **128**, 725 (1981).

48. D. R. MacFarlane, J. H. Huang and M. Forsyth, Nature **402**, 792 (1999).

49. K. D. Kreuer, S. J. Paddison, E. Spohr, and M. Schuster, Chem. Rev. **104**, 46374678 (2004)

50. T. Schober and H. G. Bohn, Solid State Ionics **127**, 351 (2000).

51. J. Frenkel, Z. Phys. **35**, 652 (1926).

52. W. Schottky, Z. Phys. Chem. ABT.B **29**, 335 (1935).

53. G. Farrington, J.Briant, Science, **204**, 29 (1979).

54. A. J. Heeger, Angew. Chem., Int. Ed. **40**, 2591 (2001).

55. C. K. Chiang, S. S. Gau, A. G. MacDiarmid, Appl. Phys. Lett. **33**, 18 (1978).

56. R. N. Marksa, D. D. C. Bradleya, R. W. Jacksonb, P. L. Burnb, and A. B. Holmesb, Synth.Met. **57**, 4128 (1993).

57. I. D. Parker, J. Appl. Phys. **75**, 1656 (1994).

58. A. Rose, Phys. Rev. **97**, 1538 (1955).

59. M. B. Armand and J. M. Chabagno, Extended abstracts, second international confercnece on solid electrolytes, St Andrews,Scotland 1978.

60. A. Killis and J. F. LeNest. J. Polym. Sci. Polym. Phys. ED. **19**, 1073 (1981).

61. A. Killis, J. F. LeNest, Solid State Ionics, **14**, 231 (1984).

62. M. A. Ratner and D. F. Shriver, Chem. Rev. **88**, 109 (1988).

63. J. M. Leger and S. A. Carter, J. Appl. Phys. **98**, 124907 (2005).

64. M. Buda, G. Kalyuzhny, and A. J. Bard, J. Am. Chem. Soc. **124**, 6090 (2002).

65. Y. F. Hu and J. Gao, Appl. Phys. Lett. **89**, 253514 (2006).

66. L. Edman, B. Liu, M. Vehse, J. Swensen, G. C. Bazan, and A. J. Heeger, J. Appl. Phys. **98**, 044502 (2005).

67. W. Zhao and J. M. White, Appl. Phys. Lett. **90**, 181906 (2007).

68. M. A. Abkiwitz, J. S. Facci and M. Stolka, Appl. Phys. Lett. **63**, 1892 (1993).

69. M. A. Arkowitz and J. S. Facci, J. Appl. Phys. **83**, 2670 (1998).

70. A. A. Gorodetsky, S. Parker, G. G. Malliaras, Appl. Phys. Lett. **84**, 807 (2004).

71. L. Edman and A. J. Heeger, Phys. Rev. B **70**, 115212 (2004).

72. J. H. Shin and L. Edman, Appl. Phys. Lett. **89**, 013509 (2006).

73. J. Gao and J. Dane, Appl. Phys. Lett. **84**, 2778 (2004).

74. Y. Hu, C. Tracy and G. Jun, Appl. Phys. Lett. **88**, 123507 (2006).

75. C. Tracy and G. Jun, Appl. Phys. Lett. **83**, 143502 (2005).

76. C. Tracy and G. Jun, J. Appl. Phys. **100**, 104503 (2006).

77. I. H. Campbell and D. L. Smith, Appl. Phys. Lett. **72**, 2565 (1998).

78. H. Rudmann, S. Shinada, and M. F. Rubner, J. Appl. Phys. **94**, 115 (2003).

79. I. H. Cambell, Phys. Rev. Lett. **76**, 1900 (1996).

80. J. C. deMello, R. H. Friend, Phys. Rev. Lett. **85**, 421 (2000).

81. J. D. Slinker, G. G. Malliaras, Nature Materials **6**, 891 (2007).

Chapter II

1. K. C. Kao, Dielectric phenomena in solids, (Elsevier Academic Press, London, 2004).

2. C. Gabrielli and M. Keddam, Electrochim. Acta. **19**, 355 (1974).

3. D. E. Smith, Anal. Chem. **48**, 221A (1976).

4. J. E. Barle, J. Phys. Chem. Solids, **30**, 2657 (1969).

5. J. Bernasconi, H. U. Bereler, S. Strassler and S. Alexander, Phys. Rev. Lett. **42**, 819 (1979).

6. I. Betova, M. Bojinov, P. Kinnunen, T. Laitinen, P. Pohijanne, and T. Saario, Electrochim. Acta. **47**, 2093 (2002).

7. C. Bohnke and O. Bohnke, Solid State Ionics **39**, 195 (1990).

8. M. Ciureanu and H. Wang, J. New. Mat. Electrochem. Systems **3**, 107 (2000).

9. C. Y. Chao, L. F. Lin, and D. D. Macdonald, J. Electrochem. Soc. **129**, 1874 (1982).

10. H. Chang, G. Jeffe, J. Chem. Physics. **20**, 1071 (1952).

11. R. J. Friauf, J. Chem. Phys. **22**, 1329 (1954).

12. J. R. Macdonald, Phys. Rev. **92**, 4 (1953).

13. T. M. Proctor and P. M. Sutton, J. Chem. Phys. **30**, 212 (1959).

14. J. H. Beaumont and P. W. M. Jacobs, J. Phys. Chem. Solids, **28**, 657 (1967).

15. H. Frohlich, theory of dielectrics , Oxford University Press, London. (1958).

16. A. J. Bard and L. R. Faulkner, Electrochemical Methods: Fundamentals and Applications (Wiley, New York, 1980).

17. J. Newman, Electrochemical Systems (Prentice-Hall, Englewood Cliffs, NJ, 1991).

18. R. Olshansky, P. Hill, V. Lanzisera, W. Powazinik, Quantum Electronics, IEEE Journal of **23**, 1410 (1987)

19. S. R. Taylor and E. Gileadi, Corrosion Science, **51**, 664, (1995).

20. A. K. Joncher, Journal of Materials Science, **30**, 2491 (1995).

21. R. Vogel and P. J. Walsh, Appl. Phys. Lett. **14**, 216 (1969).

22. A. K. Joncher, C. Pickup, and S. Zaidi, Semicond. Sci. Technol. **1**, 71 (1986).

23. J. Wener, Phys. Rev. Lett. **60**, 53 (1988).

Chapter III

1. H. Gommans and M. Kemerink, Phys. Rev. B 69, 155216 (2004)

2. F. Huet, J. Power Sources, 70, 59 (1998).

3. K. Funke, S. Br€uckner, C. Cramer, and D. Wilmer, J. Non-Cryst Solids **307**, 921 (2002).

4. Y. F. Li, J. Gao, G. Yu, Y. Cao, and A. J. Heeger, Chem. Phys. Lett. **287**, 83 (1998).

5. S. Andjelic, J. Mijovic and F. Belluccif, J. Polymer Science, Part B **36**, 641 (1998).

6. T. E. Springer, T. A. Zawodzinski, M. S. Wilson, and S. Gottesfeld, J. Electrochemical Soc. **143**, 587 (1996).

7. Y. F. Li ; J. Gao; D. Wang ; G. Yu ; Y. Cao ; A. J. Heeger, Synthetic Metals, **97**, 191 (1998).

8. S. C. Chang, Y. Yang, F. Wudl, G. He and Y. Li , J. Phys. Chem. B **105**, 11419 2002).

9. R. J. Klein, S. Zhang, S. Dou, B. H. Jones, R. H. Colby, and J. Runt, J. Chem. Phys. **124**, 144903 (2006).

10. K. Funke, Prog. Solid St. Chem. **22**, 111 (1993).

11. B. Roling, A. Happe, K. Funke, and M. D. Ingram, Phys, Rev. Lett. **78**, 2160 (1997).

12. D. L. Sidebottom and J. Zhang, Phys. Rev. B **62**, 5503 (2000).

13. K. C. Kao, Dielectric Phenomena in solids (Elsevier Academic Press. London, 2004).

14. D. P. Almond, C. C. Hunter, and A. R. West, Journal of Material Science **19**, 3236 (1994).

15. H. C. Chang and G. Jaff, J. Chem. Phys. **20**, 1071 (1952).

16. J. R. Macdonald, J. Chem. Phys. **58**, 4982 (1973).

17. D. L. Sidebottom, B. Roling and K. Funke, Phys. Rev. B **63**, 024301 (2000).

18. J. C. Dyre and T. B. Schroder, Rev. Mod. Phys. **72**, 843 (2000).

19. J. C. Dyre, J. Appl. Phys. **64**, 2456 (1988).

20. B. Roling, J. Chem. Phys. **117**,1320 (2002).

Chapter IV

1. J. Gao, G. Yu, and A.J. Heeger, Appl. Phys. Lett. **71**, 1293 (1997).

2. Y. F. Li, J. Gao, G. Yu, Y. Cao and A. J. Heeger, Chem Phys Lett. **287**, 83 (1998).

3. Y. F. Li , J. Gao , D. Wang , G. Yu, Y. Cao, A. J. Heeger., Synthetic Metals **97**, 191 (1998).

4. V. Shrotriya and Y. Yang., J. Appl. Phys. **97**, 054504 (2005).

5. M. Meier, S. Karg and W. Riess, J. Appl. Phys. **82**, 1961 (1997).

6. I. H. Campbell and D. L. Smith, Appl. Phys. Lett. **66**, 3030 (1995).

7. J. R. Macdonald, J. Chem. Phys. **54**, 2026 (1971).

8. J. R. Macdonald, J. Appl. Phys. **44**, 3455 (1973).

9. J. R. Macdonald, J. Appl. Phys. **45**, 2343 (1974).

10. J. C. deMello, N. Tessler, S. C. Graham, and R. H. Friend, Phys. Rev. B **57**, 12951 (1998).

11. H. W. Cheng, F. D. Lin, and M. C. Lonergan, J. Phys. Chem. B **109**, 10168 (2005).

12. J. D. Slinker, G. G. Malliaras, Nature Materials **6**, 891 (2007).

Chapter V

1. J. R. Macdonald, Theory and applications of impedance spectroscopy, Weiley Interscience, (2005).

2. F. Huet, J. Power Sources, **70**, 59 (1998).

3. X. Wu, E. S. Yang, H. L. Evans, J. Appl. Phys. **68**, 2846 (1990).

4. H. C. F. Martens and H. B. Brom, Phys. Rev. B **60**, R8489 (1999).

5. J. Werner, A. F. J. Levi, R. T. Tung, Phys. Rev. Lett. **50** 53 (1988).

6. C. Melzer, E. J. Koop, D. Mihailetchi, P. W. M. Blom , Adv. Func. Mater. **14**, 865 (2004).

7. J. C. deMello, Phys. Rev. B, **66**, 235210 (2002).

8. F. E. Jones, B. P.Wood, J.A. Myers, C. Daniels-Hafer, and M. C. Lonergan, J. Appl. Phys. **86**, 6431 (1999).

9. F. Lemmi and N. M. Johnson, App. Phys. Lett. **74**, 251 (1999).

10. H. H. P. Gommans and M. Kemerink, Phys. Rev. B, **69**, 155216 (2004).

11. Y. F. Li, J. Gao, D. Wang, G. Yu, Y. Cao, and A. J. Heeger, Synthetic Metals **97**, 191 (1998).

12. A. K. Jonscher, Journal Material Science. **30**, 2491 (1995).

13. M. Ershov, H. C. Liu, M. Buchanan, Z. R. Wasilewski, and A. K. Jonscher, IEEE Trans. On electron devices, **45**, 2196 (1998).

Chapter VI

1. Q. B. Pei, G. Yu, C. Zhang, and A. J. Heeger, Science **269**, 1086 (1995)

2. D. L. Smith, J. Appl. Phys. **81**, 2869 (1997).

3. J. deMello Phys. Rev. B **66**, 235210 (2002).

4. J. C. deMello and R. H. Friend, Phys. Rev. Lett. **85**, 421 (2000).

5. R. H. Fowler, Phys. Rev. **38**, 45 (1931).

6. J. C. deMello, J. J. M. Halls, S. C. Graham, N. Tessler, and R. H. Friend, Phys. Rev. Lett. **85**, 421 (2000).

7. C. H. W. Cheng, F. D. Lin and M. C. Lonergan. J. Phys. Chem. B **109**, 10168 (2005).

8. M. C. Lonergan, C. H. Cheng, B. L. Langsdorf, X. Zhou, J. Am. Chem. Soc. **124**, 690 (2002).

9. I. D. Parker, J. Appl. Phys. **75**, 1656 (1994).

10. J. C. Scott, P. J. Brock, J. R. Salem , S. Ramos, G. G. Malliaras, S. A. Carter, and L. Bozano, Synthetic Metals, **111**, 289 (2000).

11. I. H. Campbell, T. W. Hagler, and D. L. Smith, Phys. Rev. Lett. **76**, 1900 (2000).

12. D. Braun, J. Polymer Science A: Polymer Chemistry **41**, 2622 (2003).

13. J. C. Scott, P. J. Brock , J. R. Salem , and S. Ramos. Synthetic Metals **111**, 289 (2000).

14. M. Buda, G. Kalyuzhny and A. J. Bard, J. Am. Chem. Soc. **124**, 6090 (2002).

15. J. C. deMello, N.Tessler, and R. H. Friend, Phys. Rev. B **57**, 12951 (1998).

16. X. L. Chen, Z. Bao, J. H. Shon, A. J. Lovinger, Y. Y. Li, B. Crone, A. Dodabalapur, and B. Batlogg, Appl. Phys. Lett. **78**, 228 (2001).

17. L. Edman, M. A. Summers, S. K. Buratto, A. J.Heeger, Phys. Rev. B **70**, 115212 (2004).

Chapter VII

1. V. Heine, Phys. Rev. **771**, 717 (1947).
2. J. Tersoff, Phys. Rev. Lett. **52**, 461 (1984).
3. W. E. Spicer, I. Lindau, P. Skeath, C. Y. Su, and P. W. Chye, Phys. Rev. Lett. **44**, 420 (1980).
4. M. S. Dow, and D. L. Smith, Solid State Commun. **37**, 205 (1981).
5. J. H. Werner and H. H. Guttler, J. Appl. Phys. **69**, 1522 (1991).
6. I. Ohdomari and H. Aochi, Phys. Rev. B **35**, 682 (1987).
7. R. T. Tung, J. Vac. Sci. Technol. B **11**,1546 (1993).
8. R. T. Tung, Phys. Rev. B **45**, 13509 (1992).
9. A. Olbrich, J. Vancea, F. Kreupl and H. Hoffmann, Appl. Phys. Lett. **70**, 2559 (1997).
10. M. C. Lonergan, Science, **278,** 2103 (1997).
11. C. D. Hafer, M. Jang, S. W. Boettcher, R. G. Danner, and M. C. Lonergan, J. Phys. Chem B **106**, 1622 (2002).
12. F. E. Jones PhD Dissertation, University of Oregon (2004).
13. I . Ohdomari and K. N. Tu, J. Appl. Phys. **51**, 3735 (1980).
14. J . L. Freeouf. and J. M. Woodall, Appl. Phys. Lett. **39**, 727 (1981).
15. M. S. Freund, C. Karp, and N. S. Lewis, Inorg. Chim. Acta. **240**, 6 (1995).